A STUDY OF THE BALLISTIC PERFORMANCE OF LIGHTWEIGHT ARMOURS AGAINST SMALL ARMS AMMUNITION.

by
M. S. Stephenson.

A Thesis Submitted for the
Degree of Doctor of Philosophy
in The School of Engineering,
City University, London.

August 1991.

Contents

List of Tables

15. Alumina Faced Armour with Aromatic Polyamide Laminate Backing - Measured, Adjusted, and Fitted data for the Spreading of the Projectile Tip.
16. Glass Faced Armour with Aromatic Polyamide Laminate Backing - Measured, Adjusted, and Fitted data for the Spreading of the Projectile Tip.
17. Fracture Cone Angles for Alumina Faced Armour with Aromatic Polyamide Backing.
18. Measured Vcs for Laminates.
19. Values for the Constant "a" and the measured Weight of the Fragment Simulating Projectiles.
20. Results for Alumina Faced Armours with Aromatic Polyamide Backing Impacted at Oblique Angles of Incidence.
21. Maximum Diameter of the Rings Measured on 2.9mm Thick Polycarbonate.
22. Measured and Fitted Values for Radius of 5.56mm Bullets
23. The Values Calculated from both sides of the Bernoulli Equation for all the Armour Combinations Studied.
24. Bullet Tip Radius, Tip Area, and Calculated Energy for Alumina Faced GRP Backed Armours.
25. Bullet Tip Radius, Tip Area, and Calculated Energy for Alumina Faced Aramid Laminate Backed Armours.
26. Bullet Tip Radius, Tip Area, and Calculated Energy for Glass Faced Aramid Laminate Backed Armours.
27. Calculated Energy of the Fragments.
28. Calculated Energy per Layer of the Laminates.
29. Calculated and Measured Critical Velocities for Laminates against FSPs.
30. Critical Velocities of 1.1g FSPs against Polycarbonate Sheet.
31. Comparison of the Measured and Predicted Critical Velocity for some Ceramic Facing Materials.

List of Figures

Acknowledgements.

This work has been carried out with the support of the Ministry of Defence.

Thanks are due to the MOD and all individuals who gave advice and assistance during this study

Declaration.

Abstract

It has become possible over the last half century to provide lightweight armour capable of defeating high velocity bullets. The aim of this thesis is to study the behaviour of such armours and enhance the understanding of the mechanism by which high velocity projectiles are defeated.

In order to achieve this various aspects of the behaviour of lightweight armours and their constituent parts were studied. This study began by making flash radiograms of the penetration of three different armour constructions by high velocity projectiles. From the analysis of these radiograms the rate of penetration through the ceramic, the destruction and distortion of the projectile were studied. An empirical model of the performance of unfaced aramid laminates was produced .

Data on the performance of lightweight armours attacked at oblique angles was collected. The behaviour of the materials under these conditions was interpreted with the aid of the model of laminate performance.

The role of plate bending in the failure of the ceramic was considered. It was found that there was a critical thickness of ceramic below which bending waves did play a significant role in the failure of the ceramic facing. Above this critical thickness little evidence of plate bending was found. This postulation also rationalized the anomalies found in the analysis of the armour behaviour at oblique incidence.

The fractures induced in ceramic facings attacked by a high velocity projectile were examined. It was found that the formation of the observed fracture cone could be explained by the action of a shear wave. The observed axial cracking on the rear face of the ceramic was associated with the reflection of the dilatational wave.

Finally a model was developed which can predict the ballistic performance of a variety of ceramic facings attached to an aramid laminate backing. The level of understanding of the system was demonstrated by the close agreement between the model and the measured values for the performance of lightweight armours with several different ceramic facings.

Chapter 1

Introduction

Armour designers are in perpetual competition with munitions designers, each trying to overcome the latest development of the other. This type of leap frog development is best demonstrated by tank armour, but is evident in other fields of armour development. Tank armours, which have to defeat the most severe threats, namely shaped charges and long rod penetrators, have become heavy and complex.

The weight of the armour reduces as the threat level reduces in severity. Vehicle armours called upon to defeat small arms projectiles can be made from panels of glass reinforced plastic (GRP). The weight of a typical panel to defeat a high velocity bullet is still far greater than can be conveniently carried by a person.

Armours are usually classified by the type of threat they are called upon to defeat. Armours which protect against small arms projectiles are often referred to as lightweight. The term lightweight is in comparative, these armours are lighter than the steel armour required to defeat the same threat. These armours are a composite of a ceramic face on a fibre reinforced plastic backing.

For the lower threat level of low velocity projectiles, such as hand gun bullets and fragments, the usual method of protection is many layers of a high strength textile.

Ceramic composite lightweight armours intended to defeat high velocity bullets are the main subject of this thesis. The aim is to extend the understanding of how this type of armour behaves when it is impacted by such a projectile. The level of understanding achieved is measured by constructing a model to predict the ballistic performance of a combination of materials, and assess how closely the results agree with the measured values.

The research which leads to better lightweight armours covers many subjects. A brief history of the development of lightweight armours and the recent research in the fields relating to armour research are given in chapter 2. The review into relevant research begins by considering the failure of ceramics generally, and then looks at the special case of failure at elevated strain rates. This leads on to the transmission of stress pulses through materials, and then discusses how the materials are modified by these transmissions. Research work on actual lightweight armour systems is reviewed and compared to the theories in existence for the more established field of metallic armours. Finally the phenomenon of impact itself is reviewed.

There were four main parts to the experimental work. The largest part was producing the flash radiograms of the bullets penetrating the armours. Three facing / backing combinations were used, alumina faced aramid[1] laminates, glass faced aramid laminates, and alumina faced GRP laminates. Another part of the work involved measuring the ballistic performance of alumina faced aramid laminate backed armours at several different angles of attack to study the effect of varying facing thickness. In the final phase of the experimental work a coated polycarbonate material was used to investigate plate bending and its relevance to armour failure. The experimental work is detailed in chapter 3, and the associated results are presented in chapter 4.

The features observed on the radiograms taken as the bullet penetrated through the ceramic are discussed in chapter 5. It was found that the equation derived for the erosion of the projectile penetrating metallic armours, described the projectile erosion during the penetration of the ceramic quite accurately. This was the first time it had been applied to this type of armour construction. It was not immediately obvious that this would be the case because of the marked difference between the brittle behaviour of the ceramic and the ductile behaviour of the metallic armours.

In order to produce a working model of complete composite armour systems it

[1] aromatic polyamide

was necessary to model of the energy absorption of the backing. Thus an original semi-empirical model was developed in chapter 6, which could predict the energy that would be absorbed by a backing, provided that the contact area between the projectile and laminate, and the amount and type of reinforcement in the backing was known. The details and the limits of this model are also presented in chapter 6.

The simple models which were developed in the two previous chapters were applied to the behaviour of alumina faced aramid laminate backed armours which were impacted at several angles of obliquity, in chapter 7. A model for the performance of armours under these circumstances is proposed. Most of the behaviour of the armours could be accounted for with the simple models proposed in chapter 7, but there were a few anomalous results.

Chapter 8 presents a study of bending waves propagating in plates and advances a theory, which was based upon the exact wave equations, for the existence of bending waves in the ceramic facing after an impact. The theory predicted that there existed a critical velocity associated with each plate thickness, above which no bending waves would propagate through the panel. The anomalous behaviour of the armours at oblique angles of attack was then easily rationalized.

In order to extend the understanding of the mechanisms by which high velocity projectiles are defeated by this type of armour construction, a detailed study has been undertaken into the features observed during the penetration of the ceramic by a such projectiles. Alternatives to the currently accepted mechanisms are proposed in chapter 9.

All the theories and models presented in the previous chapters were drawn together in chapter 10 for the development of an original model which can predict the performance of a composite armour consisting of a ceramic facing with an aramid laminate backing. The agreement between measured and predicted critical velocities for several facing materials is quite good, within the limits determined. Models with a similar purpose have been advanced in the past, but very often have been confined to unreal idealised situations, or required data for mechanical properties at high strain rates, which is difficult to obtain. The model presented here needs only low strain rate properties which are easily obtained.

Chapter 2

Review

2.1 A Brief History of Body Armour.

The modern era of body armour had its tentative beginnings in the American Civil War. A breast plate from this era was able to defeat a .45 calibre Colt bullet, even when it was tested 100 years after it was manufactured (1). The Australian outlaw, Ned Kelly, was famed for his body armour which defeated several bullets from the Martini Henri rifle, the standard British rifle of the time. This body armour weighed 97lb, and did not protect his arms and legs, where he suffered 28 wounds before his final capture. Textile body armour, possibly made from silk, was used to defeat low velocity bullets in the early part of this century, although its efficacy has not been recorded. The Archduke Franz Ferdinand, heir to the Austro-Hungarian empire, was claimed to have possessed such a garment, but the heat was so oppressive on Sunday 28th June 1914 in Sarajevo that he did not wear it. Some accounts (2) have it that he was shot in the neck, and so it would have afforded him little protection, however this event did herald a period of history which quickened interest in body armour to a marked degree.

The first item of body armour to be on general issue was the steel helmet. The idea was originally French, and was first used on a large scale in the Champagne offensive in September 1915. A British version was issued in November 1915, and had the

advantage that its shape was more suited to mass production than the French model. Both helmets were originally made from mild steel, but at the instigation of Sir Robert Hadfield the British adopted a 12% manganese steel, known to this day as Hadfield steel. The Germans chose a harder, silicon nickel steel for their helmet, which was the last to be issued by the major powers. This was also the heaviest helmet in service, but provided the greatest area of cover.

Whilst the helmet was the most common item of body armour, some development of other items was also pursued at this time. The main area protected was the torso, and the usual dilemma was encountered. To be effective the armour was heavy, and more weight was the last thing a foot soldier wanted in battle. One flexible body armour which was a product of these times and merits a particular mention is the "Chemco Body Shield". This consisted of multiple layers of linen scraps, silk and cotton, bonded by a resin; and most resembles some of the body armours of today.

The Second World War saw another British attempt at producing a viable body armour, made from Hadfield steel plates which were worn in various configurations depending on the protection required. Again the conclusion was drawn, in 1942, that it was too heavy, too hot, and would compete for the limited supply of Hadfield steel also required for helmet production. The U.S. Air Force followed the British trials of body armour with interest, and soon realised that it had great potential for protecting the relatively immobile aircrew of heavy bombers. Hadfield steel was again chosen as the ballistic material, but now the weight was increased to 17lb, and a much greater area of cover provided. In all over 1 million sets of body armour of this and similar types were produced for U.S. aircrew during the war. The success of the flyers armour, and the use of body armour by the Japanese, generated interest in body armour in the other two American services, both of which were under going active trials when the war ended in 1945.

The armour that was on trial represented a break with what had become a tradition in armour materials, it consisted of an aluminium plate backed with 8 plies of nylon. In the years between the Second world war and the Korean war there was an intense research effort in the USA on ballistic materials. The most significant product of this was "Doron", a laminate of glass fibre and a resin developed especially for this purpose called methacrylate. This became the accepted armour material for the Marines, whilst the Army remained with the Aluminium and nylon system. The advent of a high tenacity nylon, subsequently called ballistic nylon, enabled the production of what in military slang be came known as the "Flak Jacket". This was a

combination of "Doron" plates and ballistic nylon filler. It was widely used by the US Marine Corps during the Korean War and is credited with enabling many soldiers to "fight again another day". Body armour became a fully accepted piece of American military equipment subsequent to this conflict.

The Vietnam war saw the use of the previously developed body armour, and the introduction of an all nylon flexible jacket. Unfortunately the limitations of the body armour were graphically highlighted by the nature of the fighting in S E Asia. The first problem encountered was the increased physiological load imposed by wearing, what amounted to, an impervious plastic cover in a very humid jungle environment. Troops became reluctant to wear their body armour under these conditions. The second problem was much more serious. In a general war, such as WW I, WW II, and Korea a relatively small number of casualties are caused by high velocity bullets; the vast majority are actually caused by fragments from exploding munitions. However, the larger element of terrorist attacks involved in the Vietnam campaign resulted in more casualties from high velocity bullets. The construction of the body armour used was based on the experience of the previous conflicts, and so was not optimised for a high velocity bullet threat. Additionally, the weight of armour needed to defeat this type of threat is substantially greater than that required to defeat a fragmentation threat.

The increased threat from high velocity rounds and the vulnerability of the helicopters, which were used for the first time on such a large scale, caused serious consideration to be given to methods of defeating high velocity projectiles. The solution to the problem lay in work done in 1918 by a Major Neville Monroe-Hopkins, a physicist, who found that the ballistic performance of steel could be enhanced by the addition of a 1/16th inch thick layer of enamel on its front face. This lead to the development of ceramic armours consisting of a very hard ceramic front bonded on to a more flexible, aluminium or glass fibre backing. Three types of ceramics were used as front face materials, alumina, silicon carbide, and boron carbide. Boron carbide was the best, but also the most expensive, whilst alumina had the lowest performance, but was the least expensive. Thus the modern high velocity ballistic armour plate was born.

Whilst Vietnam was occupying American thoughts on the protection of their servicemen, the British Army was called on to become a peace keeping force on the streets of Ulster. In a similar way to the US troops, the British servicemen were facing a terrorist type of campaign where they were exposed to a greater high velocity

threat than they would have been subjected to in a conventional conflict. The troops were issued with US style Flak Jackets as an emergency measure, but it was not possible for these to defeat a high velocity round. The existing American technology was adopted and improved upon to provide a protective plate which covered the heart and major blood vessels. The improvement was the replacement of the glass fibre backing of the ceramic with a laminate made from an aromatic polyamide, which had much superior ballistic performance. This meant that the plate could be made as light as possible, and interfere least with ease of movement.

As the range of potential armour materials increases with advances in ceramic technology, then a deeper understanding of the mechanisms by which such composite armour systems defeat high velocity bullets is needed. The aim of this study is to investigate the factors which affect the penetration of the armour system by lead ball rounds, such as the formation of the fracture cone in the ceramic, and how the backing influences the behaviour of the ceramic.

2.2 Review of Relevant Research.

This section reviews the previous work done in the fields of ceramic failure and then goes on to study how the failure of ceramics is influenced by higher strain rates, and how stress pulses are transmitted through the material. That work is used as the basis of the studies conducted into the effect stress pulses have on the behaviour of ceramic materials, and in particular the behaviour of ceramic faced composite armours. Finally the large body of information relating to the penetration of armours and impact phenomenon in general is reviewed.

2.2.1 Introduction to the Failure Modes of Ceramic Materials

Ceramic materials are commonly regarded as hard brittle substances with very high melting points. The class of ceramics used in this work are some times called engineering ceramics because they have high strengths; although they retain the brittle failure characteristic of all ceramics. The brittle nature of these materials originates from the low mobility of dislocations within the crystal structure. It is very difficult for plastic flow to relieve strains within the material. Fracture occurs at a stress which is substantially below the theoretical fracture stress of the material, by the propagation of cracks nucleated at defects within the material. This accounts for both the low tensile strength and the marked difference between the tensile and compression strengths. The latter can be an order of magnitude greater than the former. Increases in the strength of ceramics have been made by exercising greater control over the inherent defect population. It is the high modulus and high compressive strength which make ceramics attractive materials for the facing on composite armour systems.

Griffith was the first to investigate the low strengths measured for glass and ceramic materials. He proposed that the material failed when an existing defect was able to extend rapidly by the conversion of elastic strain energy in the material into surface energy of the advancing crack. Usually only the largest defect initiates a crack and this is called the critical defect. The stress required to initiate and propagate a crack from a defect is related to the defect size, and so large defects initiate cracks at low applied stresses and so degrade the mechanical performance most. A material

parameter, the fracture toughness, is used to quantify a materials inherent resistance to fracturing. The most commonly quoted version of this is the plane strain fracture toughness (K_{Ic}), which is related to the opening mode of crack loading, see figure 1. Two other fracture toughness parameter can be measured, which are governed by the different modes of loading a crack, which are also detailed in figure 1.

A recent addition to the field of fracture mechanics is the study of dynamic fracture, fractures occurring at elevated strain rates, with the attendant specification of dynamic fracture toughness parameters.

An interesting feature of fracture is that the velocity of propagation of a crack is dependant on the applied stress only up to a critical value. Above this critical stress cracks propagate at a single velocity, the critical crack velocity. Values of about half the Rayleigh surface wave speed have been quoted. This becomes more important when the time of application of the stress is short and the pulse is past before the cracks have had a chance to travel very far. This is thought to be the basis of the increased dynamic strength of some materials. Cracks other than the single largest crack in a material are able to develop. The idea of a lot of cracks all growing at once has in turn given birth to damage mechanics, based on a statistical approach to material strength, and its variation due to the passage of stress pulses.

Material which has been subjected to a stress wave, but has not experienced catastrophic failure, has been found by Case (3) to have a reduced value for both Poisson's ratio and Young's modulus. Four models relating the Young's modulus of ceramics to their Poisson's ratio after the introduction of microcracking into the material were examined. The changes were recorded as the ratio of the new Poisson's ratio to the original one. All four theories were in quite close agreement for ratios of Poisson's ratios between 0.5 and 1.0. The equations relating to the separate models were then rewritten in such a way as to eliminate the dependence on microscopic parameters such as microcrack size and number, expressing them solely in terms of Young's modulus and the Poisson's ratio. The results of experimental work showed that the Young's modulus and Poisson's ratio reduced as the amount of microcracking increased. It was found that rocks with a low value of Young's modulus also tended to have a low Poisson's ratio. When these rocks were subjected to uniaxial compression both values rose. This suggested that the materials studied were porous, and the compressive stress caused the voids to close up.

2.2.2 Failure of Ceramic Materials at Elevated Strain Rates.

Langford (4) experimented with several ceramic materials subjected to a range of strain rates, from quasi-static to 100 per second. Figure 2 shows the change in compressive strength with strain rate for the materials tested. There was little or no increase in the compressive strength of most materials until a substantial strain rate was reached and then a quite rapid increase was noted. The apparent drop in the strength of the line labelled NC 350 was apparently due to a change in fracture behaviour from transgranular to intergranular. All other ceramics tested in that programme, and other work referred to found the failure of ceramic materials in general to be transgranular over the entire range of strain rates.

Based on the results presented above it was proposed that the low strain rate compressive strength of ceramics is governed by thermally activated tensile microcrack growth. Figure 3 shows a conceptual diagram, derived by Langford, which outlines how a tensile crack can be produced within a compressive stress field. The basis of this is that the cleavage planes of the grains lie in different directions, and so there is effectively a modulus mismatch across the boundaries. This mismatch will give rise to tensile stresses as shown in the diagram, with a magnitude proportional to

$$\sigma \quad \propto \quad \mu(1/E_1' - 1/E_2') \tag{2.1}$$

where σ = the induced tensile stress.
μ = Poisson's ratio
E_i' = Effective modulus of grain i

The high strain rate compressive strength of the materials were all found to be related to the strain rate in the following way

$$\sigma_c \quad \propto \quad (\dot{\epsilon})^{0.3} \tag{2.2}$$

where σ_c = the compressive strength of the material
$\dot{\epsilon}$ = the strain rate

The usual expression governing the fracture toughness of materials subjected to quasi-static loading is

$$K_I \quad = \quad \frac{2\sigma\sqrt{r_0}}{\sqrt{\pi}} \tag{2.3}$$

where σ = the tensile stress
r_0 = the penny shaped crack radius.

This relationship holds until the time of application of the stress is $t < r_0/c$, where c is the speed of sound in the material. Then K_I is given approximately by

$$K_I \approx \sigma\sqrt{ct} \tag{2.4}$$

At failure $K_I = K_{Ic}$. Thus the dynamic fracture stress is given by

$$\sigma_f = \frac{K_{Ic}}{\sqrt{ct_f}} \tag{2.5}$$

where σ_f = stress to fracture
t_f = time to fracture initiation

The strain rate can be represented by

$$\dot{\epsilon} = \frac{\dot{\sigma}}{E} = \frac{\sigma_f}{\rho_0 c^2 t_f} \tag{2.6}$$

where ρ_0 = the material density

Eliminating t between equations (2.5) and (2.6) gives

$$\sigma_f \approx \sqrt[3]{\rho_0 c K_{Ic}^2}\,(\dot{\epsilon})^{1/3} \tag{2.7}$$

Thus $\sigma_f \propto (\dot{\epsilon})^{1/3}$, which is very close to the expression derived from the experimental results. From these equations the lower bound for the transition from the thermally activated process to the dynamic regime should correspond to

$$\dot{\epsilon_c} = \frac{K_{Ic}}{\rho_0 c r_o^{3/2}} \tag{2.8}$$

where r_o = maximum initial flaw size. $= c\,t_f$
$\dot{\epsilon_c}$ = Critical strain rate

Liaw et al (5) compared the damage produced in metals by an impact, to the damage produced in monolithic ceramics by a similar impact. The major difference

between them is that metals usually involve plastic deformation, but ceramics tend to exhibit more cracking. Elastic plastic indentation fracture models have been proposed in the literature to explain the permanent depression produced. The experimental evidence presented in that paper shows that microcracking can be evoked as an explanation of that feature. Unfortunately the density of the microcracks is so high the use of linear elastic fracture mechanics is precluded on the grounds of complexity.

To over come this a damage mechanics approach was used, where the process is modelled on a computer, taking account of the deteriorating mechanical properties of the material as the damage increases. Four assumptions were made for that work. a) A crack will form at a point in the material perpendicular to the direction of the maximum principal stress and when the tensile stress at the point exceeds the tensile strength of the material. b) Orthogonal cracks will form at a point where the maximum shear stress exceeds the shear strength of the material. c) A closed crack will carry a compressive load and resist shear according to Coulombs law of dry friction. d) An opening crack cannot support a tensile load.

Good agreement between the observed formation of the pit and lateral cracking was found. However the model failed to predict the development of the observed cone cracks at all. This would suggest that the assumptions are sound, but are incomplete, and there is another process controlling the formation of the cone crack.

Kumar (6) found that whilst the quasi-static properties of Basalt and Granite are similar, their dynamic properties differ considerably. That led to a study of the performance of these materials when the temperature and stress rate were varied. Strain rates up to $2 * 10^3$ were applied with a split Hopkinson bar. It was found that the relationship between strain rate and fracture stress was linear up to a critical value and then began to increase more rapidly. Griffith observed that a blunt crack could be made to grow under a compressive stress, if that stress were eight times the stress required to made it grow under tension, and was applied at thirty degrees to the crack direction. That was combined with the suggestion that the velocity of propagation of a large number of microcracks would remain proportional to the applied stress, and so as the rate of stressing increased, then so would the average crack velocity, explaining the observed behaviour.

2.2.3 Transmission of Stress Pulses Through Materials.

A full chronological list, of all the workers in the field of waves and wave propagation in solids, up to 1955, is given in Graff (7, pp 5–7). Only the most salient ones are surveyed.

Following the discovery of surface waves by Lord Rayleigh in 1885, Lamb (8) published his paper on the propagation of tremors over the surface of an elastic solid subjected to a periodic forcing function. That work explored resulting displacement of the surface of the solid, and the effect on the propagating waves. However it has applications well beyond the sphere of seismology, where the original application was intended.

It was found that the disturbance spreads over the surface as an annular wave. The initial form of the wave obviously depends upon the shape of the pulse applied to the surface. However if the pulse duration is short the waves acquire a characteristic form as they move further from the site of the impulse. This characteristic form consists of three distinct parts which correspond to the compression, shear and surface waves respectively. The history of the first two parts depends on the time integral of the original pulse, but the surface wave follows the time scale of the original impulse. The important feature of the surface wave is that the material involved in it describes an elliptical path, as opposed to the other two wave types where the motion is in one direction only.

The transmission of stress waves through semi-infinite bodies was also considered by Miller and Pursey (9). The application of a force on the surface was developed to investigate the structure of the waves generated within the body. They found that three wave types were generated, which are shown in figure 4 after Woods (10). The spacing of the waves in this diagram is in proportion to the ratios of the velocities of the wave types. The dilatational wave travels fastest followed by the shear wave, and the surface wave is the slowest. The significant development of this work is that the shear wave is shown to change its direction of shear at an angle from the axis. Woods defined a shear window around this point where the strains induced in the material are highest.

2.2.4 Material Behaviour Due to Stress Pulses.

Hopkinson was the first to investigate the behaviour of a material subjected to a stress pulse in the famous wire and bar experiments. These showed the importance of the reflection of a pulse from a boundary. If that boundary was fixed, an incident compression pulse was reflected as a compression pulse. For a free boundary a compression pulse was reflected as a tensile pulse and vice versa.

Kolsky and Shearman (11) performed experiments to observe the effect of transient stress waves on transparent plastics. The stress pulses were generated using small quantities of lead azide on the surface of sheets of polymethylmethacrylate of varying thicknesses. This explosive was assumed to give a sharply rising compressive stress pulse which decayed linearly, and since the polymethylmethacrylate had a greater compressive strength than tensile strength, this allowed a distinction to be made between compressive and tensile damage.

That work showed that with high intensity short stress pulses it was the reflected tensile wave which did most damage. In the thinner sheets it produced a scab on the back face. This was contrasted with the longer pulse generated by nitro-glycerin, which did not produce a scab because the there was time for the reflection to interfere. Cylindrical specimens tested with lead azide not only had scab formation at the bottom, the face opposite the explosion, but also cracks were found where the waves reflected from the sides interacted with the waves reflected from the bottom.

Christie and Kolsky (12) continued the work on short stress pulses in materials by using lead azide and .22 rifle bullets on glass and plastics. It was established that the cracks produced within a material by a stress pulse may not have time to grow before the stress pulse has passed on. The types of failure caused by lead azide and a .22 bullet were compared, and it was found that while the pulse generated by the bullet lasted only 100 microseconds, it was long enough to allow several large radial cracks to form and grow. The pulse from the lead azide caused a larger number of much smaller fractures, concomitant with a shorter pulse duration.

The radial cracks were formed by the hoop tensions caused by the spherical nature of the compressive pulse emanating from the contact point. In that case the number was limited because the formation of the crack was able to relieve quite a large volume

of material, because there was sufficient time for the relief wave to travel the required distance. In the case of a shorter pulse this type of stress redistribution is confined to a smaller volume of material because the rate of stress relief is low compared to the pulse duration.

Figure 5 reproduces the graphic representation used by Christie and Kolsky (12) to describe the stress state of the material near a free boundary which reflects a stress wave. The thick line represents the resultant stress experienced by the material. It can be seen clearly that, if the incident wave is compressional, and depending on the exact pulse shape, there is a region at a fixed distance behind the boundary where the pulse first reaches the maximum tensile strength of the material. It is here that the material fails, and here is the origin of the scab described previously.

Christie (13) then investigated some of the phenomena described above using photographic methods. In particular the position of a corner crack was studied. This crack was generated in a sheet of glass 5.5" x 5.5" x 0.25" when a lead azide charge was detonated on the edge. Both dilatational and shear waves are generated by the detonation and both have spherical wave fronts. When either dilatational or shear waves are incident obliquely on a free boundary the reflection contains both types of wave. Thus both shear and dilatational reflected waves are generated continually as the original spherical waves progress through the depth of the material, because each wave front is incident at an oblique angle on the side. The crack in question was shown to follow the locus of the intersection of the two shear waves produced by reflection at the plate side.

This situation is not particularly relevant when a projectile hits a ceramic plate in the centre not on an edge.

A further experiment conducted in that work was the application of very short pulses to the edge of polymethylmethacrylate plates from a steel bar. It was found that with very short pulses the dilatational wave and the shear wave separated as they propagated within the material, however with longer pulses this did not happen, and the damage produced was the sum of the effects of both waves.

The magnitude of the maximum stress pulse which glass, and some glass-like plastics could transmit was investigated by Kolsky and Shi (14). In that work a Hopkinson bar, made from the material under study, was employed. In that work the momentum

was measured by using one of the rods as a ballistic pendulum. Attenuation of the pulse was found in all cases, and the cause depended upon the material. In glass it was caused by the inertia effects of the bar itself, however in the polymethylmethacrylate bars the viscoelastic behaviour was the major contributing factor. That restricted the choice of bar to either thin or short ones, the latter were chosen for that work. The rods failed by a small cylinder detaching itself from the end opposite the explosion, in a manner very similar to that of the original Hopkinson bar experiments. The length of the cylinder was found to be quarter of the length of the pulse travelling in the bar. If the charge of explosive was increased the multiple failures could be achieved, because of the reflection of the tail of the pulse from the new surface generated. It was found that glass could tolerate a dynamic tensile load roughly twice that of the static value.

Ten years later the study of fractures produced in glass blocks was continued by Tsai and Kolsky (15). That work studied the impact of steel balls on glass blocks, and investigated the coefficient of restitution, the fractures produced on impact, and the stress waves generated by the impact.

A quasi-static approach was used to describe the stress state in the material after impact, but before fracture. The wave analyses performed by both Lamb and Miller and Pursey (9) were used to describe the structure of waves on the surface of the block. They observed the generation of the cone crack which penetrated further and further into the material as the impact velocity increased, although no attempt was made to interpret the results with reference to the Miller and Pursey analysis. Beyond a certain velocity additional radial cracks were also found to form. The formation of the ring crack, which is the precursor to the cone crack, was thought to form when the critical tensile stress of the glass was exceeded at the edge of the contact area. The formation of the ring cracks and subsequent development into the fracture cone seemed to have very little effect upon the coefficient of restitution. The conclusion drawn from this was that very little energy was absorbed in the production of these cracks. When the impact velocity exceeded that at which the glass shattered, then the coefficient of restitution dropped sharply.

A stress wave was also produced when a surface ring crack formed. This was superimposed on the existing stress wave that was travelling away from the impact, and was attributed to the sudden stress change produced by crack formation. The analysis of Miller and Pursey (9) was extended to describe the shape of waves produced on the surface of an elastic material subjected to a force which varied with

time, and had a varying contact area. The measured surface waves agreed quite well with the predicted shape.

Fracture patterns very similar to those found by Kolsky and Shearman (11) were also found by Evans and Taylor (16) to occur in steel samples subjected to intense stress pulses. The hardness of the metal at various locations within the sample was also measured. It was found that around the detonation site the hardness increased substantially, indicating that the material had been stressed beyond its elastic limit. Nearer to the scab fracture, at the other end of the cylindrical sample, the hardness was reduced, which was attributed to the formation of a network of fine microcracks. It is reasonable to assume this could also occur with a ceramic sample subjected to similar conditions.

2.2.5 Previous Ceramic Composite Armour Research

The most serious attempt at understanding the mechanisms involved in the penetration of ceramic armour systems was done by Wilkins (17). The main aim of the work was to provide enough data to generate a computer simulation of the penetration process. The measure of ballistic resistance of an armour is its Critical Velocity, this is defined as the impact velocity below which penetration is very unlikely. The model developed was then used to vary material properties, and study the effect upon the calculated V_c. The experiments performed during that study were all done with hard steel projectiles having either a conical or blunt nose. That was done largely to simplify the interpretation of the experimental data.

Armours consisting of an alumina face 8.6mm thick, and aluminium backing 6.35mm thick, were tested with conical steel projectiles. The impact velocity was 853m/s, which was just below the V_c for that armour combination. The following chronology was established.

- **0–9 microseconds**
  Destruction of the projectile tip, and yielding of the backing at the interface with the ceramic. That allowed bending in the ceramic which caused tension on the rear face of the ceramic front. So initiated an axial crack which propagated towards the impact face and contributed to the ultimate failure of the ceramic.

- **9–15 microseconds**
  A fracture conoid was initiated at the front face of the ceramic directly beneath the projectile, which eroded its tip further by a grinding motion caused by the ceramic rubble. It was calculated that 40% of the initial projectile energy is removed by ejection of the eroded projectile material. The projectile is eroded because the stress induced in the tip is greater than its strength. It was proposed that the maximum decelerating force on the projectile was related to its yield strength.

- **After 15 microseconds**
  The erosion stops, and the projectile energy loss equals that gained by the target. Only 60% of the original impact energy remains, and that is all absorbed by the backing.

Wilkins proposed that a substantial increase in the V_c would be gained if the erosion of the projectile tip could be extended for another 2microseconds, and suggested maintaining ceramic integrity was a way to do this. It could be achieved by having a more rigid backing material which yielded at a higher stress, delaying bending of the ceramic, and postponing development of the axial crack. Alternatively a ceramic with greater tensile strength could be employed in order to hold up the development of the axial crack.

Lead projectiles are used in this work rather than the steel ones used by Wilkins. Lead is much softer and may melt due to the temperatures induced by the pressures encountered during the penetration process. There is no concrete evidence for this yet, but it remains a distinct possibility.

Figure 6 is taken from Wilkins (17), and shows the rear face of a ceramic plate with a glass backing at four intervals after the impact of a .30 calibre steel projectile. The circular base of the cone can be clearly seen after 9 microseconds. Further figure 7, also from Wilkins, shows several partially formed fracture cones, the inner most has an angle of 53°. The time taken for the cone to appear on the back face is 9 microseconds, corresponding to a crack velocity of 1590m/s, which is about that usually quoted for alumina in the literature.

A computer simulation was constructed which reproduced the events described above. The tensile strength of the facing material was increased in the calculations,

and the results showed that the integrity of the tile was maintained longer and the calculated V_c was 76m/s greater. It was also proposed that introducing ductility would improve the V_c, by allowing the ceramic to remain intact longer by undergoing plastic deformation rather than fracturing. Beryllia was used as an example of a ceramic which demonstrated plastic deformation, and it did have a suitably high ballistic limit. Unfortunately, handling the material was difficult due to its toxicity, which would prove to be a disadvantage in field use of the armour, and so was not pursued beyond these few tests.

The pressures generated by the impact of a steel projectile on an alumina facing were estimated from the intersection of the Hugoniot curves for the ceramic, and a reflected Hugoniot curve for steel. That method has its limitations, because Hugoniot curves are produced using plain strain from one dimensional impacts, and that is not the case in the armour situation. Figure 8, also from Wilkins, illustrates the Hugoniot curves in question. The slope of the line up to the Hugoniot elastic limit is the elastic impedance, if that can be increased, then a higher impact pressure would result. It is the elastic impedance at the impact stress level which is important not the zero stress level, which is much easier to calculate.

A further parameter which was identified as important was the compressive yield strength of the ceramic. That governs the stress at which the impedance of the material changes, or the amount of elastic distortion that can be tolerated before elastic behaviour ceases, and is a measure of the resistance to distortion during the impact. A high compressive yield strength alone is not a good indicator of good ballistic potential, as the example of silicon shows. That had a high yield but a low elastic impedance, and so low pressure on impact, and was shown to have poor ballistic performance.

It was found that if a ceramic was tested with no confining pressure, then the load it can support falls to zero when it ruptures. However if it is subjected to a hydrostatic pressure see figure 9, then it can continue to support a load of about half to two thirds its rupture strength, provided the confining pressure is above a critical value. Table 1 shows the values for several ceramics tested in this way. That behaviour was attributed to the friction between the fragments.

The effect of the backing was also investigated. The conclusion was drawn that for a constant backing thickness the V_c increased linearly with increasing ceramic

thickness. That was explained by assuming the stress in the front face is directly proportional to the impact velocity, and that falls linearly with increasing thickness of the ceramic. Thus the stress on the backing is inversely proportional to the ceramic thickness, and is proportional to the impact velocity. That provided a rule of thumb for estimating the thickness of a ceramic required to defeat a given threat which needed only one V_c calculation.

Finally the difference between the two types of backing material, glass fibre and aluminium, were investigated. Two separate failure mechanisms were identified. The aluminium was less flexible, but provided greater support to the ceramic during penetration, and failed by shear below the impact site. The glass fibre provided less support, but was better able to absorb the energy of the projectile and rubble.

Rosenberg and Yeshurun (18), developed a ballistic efficiency indicator. This was based on the work of Wilkins, and provided a method of ranking various ceramic materials in their order of performance against 12.7mm and 14.5mm Armour Piercing (AP) ammunition. They discussed Wilkins work and concluded that some of observations had been complicated by bending of the ceramic armours because they were supported by thin backings. Thus in there work a solid block of aluminium was employed as the backing which prevented any possibility of the ceramic bending under the impact. A close correlation between the ballistic performance and the compressive strength of the ceramic was found.

A finite element computer model which predicts the ballistic performance of ceramic composite armours has been developed by Prior (19). It is based upon the work of Wilkins, and similarly requires that two material constants are optimised by comparison with experimental data before the results can be used. Its intended use was as a method of studying variations in the material properties, once these had been established.

The performance of textile reinforced laminates was studied by Prosser (20). It was found that the energy absorbed by a laminate during the penetration was independent of the impact velocity. There were two regimes identified by the slope of the curve relating total energy absorbed to number of textile layers. The transition from one regime to the other was attributed to the impact velocity exceeding the velocity at which the fibres in the textile failed immediately upon impact. The energy v no. of layer lines did not pass through the zero point. This was attributed to a further

energy absorption mechanism occurring such a delamination which was not accounted for in the calculations.

2.2.6 Fractography of Ballistically Tested Materials

Frechette and Cline (21) investigated the appearance of several materials after they had been ballistically tested. These materials included magnesia, alumina, and plate glass. It was established that the sequence of events during failure of the material during an impact was the same for flat nosed, round nosed, and conical projectiles. They also found that the fracture cone begins on the front face as a cylindrical crack which flares out rapidly in the usual conoid. Radial cracks were also found to emanate from the conoid surface and spread both into the conoid itself, and the surrounding material. These observations were made using a glass target, and in that these radial cracks travelled faster than the conoidal fracture.

When the velocity of impact was approaching penetration then more than one conoid was formed. These also originate at the front, or impact face. There was also evidence of an axial crack which started at the rear face of the ceramic and travelled forward. The final stages of failure began when the conoid moved forward because the backing yielded due to the pressure transmitted through the conoid.

2.2.7 Studies of the Penetration Process in Metallic Armours.

There is a large body of information and observation available on the penetration of monolithic steel armours. Most of the research into penetrations into metallic armours are concerned with steel plates usually used for tank armour, and consequently the projectiles are very different to the soft lead used in this study.

The penetration process has been divided up by Hohler and Stilp (22) into four phases, figure 10. The first is described as a transient phase following immediately after the impact, and includes the initial projectile target interaction. It is charac-

terised by a high stress peak and the generation of shock waves which travel through the target. The next is called the "primary phase" and consists of a constant level of stress behind the shock front. The tip of the projectile undergoes a steady flow as it is eroded and swept away from the projectile target interface, having lost all its forward momentum. The duration of that phase is related to the aspect ratio of the projectile. The third phase is called the cavitation phase, it begins when the projectile has been totally deformed and the stress level falls during that part of the penetration process. The final phase is the recovery phase where the crater formed contracts. These stages were identified for the penetration of a long rod penetrator into thick steel tank armour, however the first phase may apply to a ceramic armour model also. The second phase appears similar to that observed in ceramic armours, but there is little evidence that the lead bullet looses all its forward momentum and curls back on its self.

An ideal rod penetrator was defined as behaving according to the hydrodynamic jet theory. That theory predicted that a graph of the penetration depth versus the impact velocity would be S-shaped. Data from impacts of real rods into steel armours showed a distinct tendency towards that shape of graph. From that two main conclusions were drawn, the first was that the material strengths had little influence, but the densities were very important, and the second was that the dynamic strength of the target was greater than that of the projectile in that case.

Dehn (23) also examined long rod penetrators interacting with semi-infinite targets. The aim was to produce a unified theory of penetration which would apply both to long rods and Munroe jets impacting such targets, and predict the depth of penetration into the target.

Goldar and Paldas (24) studied the dynamic response of transversely loaded beams. These beams were simply supported, and had a striker dropped from a constant height onto the midpoint. The beam to striker weight ratio was kept constant, and two parameters were measured. One was the "initial stress pulse" calculated from $\rho C_0 V_0$, and the other was the peak tensile stress, measured along the axis of the beam on the under-side below the impact point. From these the ratio $\sigma/\rho C_0 V_0$ was calculated. ρ was the beam material density, C_0 was the speed of sound in the material, and V_0 was the impactor velocity, σ was the measured peak stress. It was found that the ratio was in close agreement with the Poisson's ratio for the beam material. There was no attempt at explaining that.

The effect of penetration steel targets with tungsten penetrators has been studied by Tate (25), and expressions describing the temperatures found in the projectile have been presented. It was concluded from this work, which was conducted with velocities greater than 1km/s, that thermal conduction was significant only very close to the interface between the projectile and armour. Other than in this narrow area most of the flow was considered to be adiabatic. When the distances were scaled relative to the crater diameter the temperature distribution is independent of the impact velocity and approaches melting temperature in a small region which is of a similar size to the conduction zone. The melting point of lead, the projectile material used in this series of test is significantly lower than that of the tungsten penetrator used in Tate's tests.

2.2.8 Impact Phenomenon

In 1975 Janach (26) studied the impact of steel cylinders against rocks, with the intention of investigating percussive drilling. The initial situation studied was a purely elastic contact, where both cylinder and rock remained elastic. That occurred when the impact velocity was low, and the contact pressure rose to that required to bring the steel cylinder impacting the rock to a halt at a penetration corresponding to purely static loading.

As the impact velocity was increased the rock failed in a similar manner to that observed by Tsai and Kolsky (15) with glass. Since the steel projectiles were hardened, the the failure was confined to the rock, with the projectile remaining elastic. If the maximum pressure that could be supported by the broken rock was less than the pressure required to bring the projectile to rest, then the interface been rock and cylinder continue to advance through the material. In any real situation, however the projectile will not be infinitely long, and so the elastic waves reflected from its back face bring it to rest. The rock being impacted was for all practical purposes infinite, total penetration could not occur, and so the projectile rebounded with a residual velocity.

Figure 11a illustrates the distribution of stress in impacts where both the rock and projectile remain elastic, and Figure 11b where only the projectile remains elastic. These figures also show the crushed rock being pushed out away from the contact zone. Wilkins (17) found evidence of crushing of the ceramic below the impact site

in ceramic armours, so that may go some way to explaining to the mechanism of penetration occurring through the ceramic.

Crushing of the rock was found to increase the volume occupied by the debris due to bulking of the material. The increase in volume of the granite studied by Janach (22) was found to be 20%, which is accommodated by the crushed rock moving from under the projectile. Very high strain rates are induced during that process and the bulking can introduce inertial forces which result in a higher mean pressure in the impact zone. That is illustrated by figure 12 which shows the increase in the largest principal stress related to increases in the confining stress, as was discussed by Wilkins (17).

The bulking phenomenon was investigated further by stressing a small piece of the granite beyond its elastic limit in a split Hopkinson bar. The only failure mode available was crushing, but because that requires a volume increase then it could only start at the free surface and travel towards the centre. That motion, however induced a further confining stress on the material in the interior of the sample, which enabled that material to support a greater load (σ_a), in turn preventing total failure of the sample. The upper limit of σ_a is the Hugoniot Elastic Limit for the material, for granite that was found to be about 4000MPa, which is 20 times its unconfined compressive strength.

A further factor in the formation of the crater below the impact site is chip formation, also illustrated in figure 11. These chips are produced by the larger radial cracks which form by the action of the tensile stresses tangential to the main compression direction. That was proposed as the explanation for brittle rocks failing in a direction parallel to the largest compression direction. Radial cracks were observed by Wilkins (17) in the penetration of the ceramic armours by high velocity projectiles.

The penetration of a projectile in to glass blocks, which were long enough to be considered as infinite, was studied by Hornemann et al (27). Two types of steel projectile were used, flat faced cylinders and conical projectiles, at velocities from 400 m/s to 1600 m/s. The type of damage produced within the glass is demonstrated in Figs 13,14,and 15. It was found that the damage caused by a conical projectile was much more regular than that from a flat faced cylinder, as can be seen by comparing figs 13 and 14 to figure 15. . That was explained by suggesting the rate energy is transferred from the projectile to the target was greater for the flat faced cylinder

than the conical projectile.

There is also a suggestion of a cone of cracks ahead of the roughly hemispherical mass induced by the impact of the flat cylinder. That was unmentioned in the paper, but may be of significance, considering the large body of information discussing the formation of fracture cones in brittle materials. Results such as those shown in Figs 13, 14, and 15 were used to plot the rate of progress of the crack front versus time, fig 16. It was discovered that its velocity was in excess of the maximum crack velocity accepted for materials of that type. Thus it was proposed that damage caused in that way progressed through the material by the nucleation of secondary crack fronts by the action of the stress wave on microscopic flaws, ahead of the main front, travelling with a velocity which appeared greater than that of the fastest crack. That hypothesis was supported by impacting glass which had deliberately introduced flaws and did indeed generate new cracks ahead of the main crack front, figure 17.

2.2.9 Conclusion to the Survey Section

Literature on many subjects related to the penetration of ceramic materials by projectiles has been reviewed. It is clear that ceramics fail in ways which are fundamentally different to those of metals, predominantly brittle failure without any plastic flow. The properties are different at elevated strain rates to those more usually measured at quasi-static rates, and that is of immense importance when considering ballistic impact. The formation of fracture cones and radial cracking is well recorded, and will be investigated further in the present study. There appears to have been little work aimed at explaining the exact mode of failure of composite armour systems.

Chapter 3

Experimental

This section presents the programme of work. It describes the equipment and techniques used in the experimental work of this study, and describes the materials and construction of the armours and other samples.

3.1 Programme of Work and Aims

3.1.1 Overall Aim

The overall aim of this study is to explore the current understanding of ballistic penetration processes and where possible extend it. As a measure of the depth and precision of this understanding it was intended to produce a model which can predict the ballistic performance of an armour system provided its basic mechanical properties are known.

3.1.2 Flash Radiography.

The aim of this part of the work was to study the penetration process which occurred when high velocity bullets impacted onto ceramic faced laminate backed composite armours, using a flash radiography technique to freeze the event. It produced radiograms which formed a permanent record available for analysis. The results of this analysis were compared with the current understanding of ballistic penetration and where possible this understanding was extended.

3.1.3 Ballistic Testing of Unfaced Aramid Laminates

The aim of this series of tests was to investigate the ballistic behaviour of unfaced laminate backing material and develop a model which could predict its performance under a variety of conditions.

3.1.4 Ballistic Testing of Armours at Oblique Angles of Impact

This work was conducted with the aim of establishing the variation in the ballistic performance of armours at varying angles of incidence. Additionally it was intended to explore and extend the current level of knowledge of the behaviour of armours under these conditions, and contribute to the general understanding of ballistic penetration.

3.1.5 Study Plate Bending with Reference to Ballistic Impact.

In the review in section 2.5 it was reported that bending was thought to play a significant role in the penetration process. The aim of this part of the work was

to examine this basic premise, and establish it's significance in the penetration of ceramic composite armours by soft lead ball rounds.

3.1.6 Study of Waves Generated by an Impact.

Several features have been observed to occur in armours subjected to ballistic impact. It was the aim of this area of the study to examine these features and determine whether they were caused by the waves generated by the impact.

3.2 Ballistic Testing

3.2.1 Range Layout.

The range layout is shown in figure 18. The firing point was separated from the range by a brick wall with a small port through which the barrel protruded into the range. Communication was via doors operated by castellated key system which prevented both doors being open together. This was an important safety measure. The armours were mounted on a frame 4 metres away from the barrel, and positioned so that the bullet impacted the centre of the armour. Mounted coaxially with the barrel was a close circuit TV. camera. This was used in the final positioning of the target.

3.2.2 Projectiles Used.

Two projectiles were used in this work, a standard NATO 5.56mm ball round (L3A1) and a Fragment Simulating Projectile (FSP). A drawing of the bullet is shown in figure 19. These bullets were used in the flash radiography and Critical Velocity (V_c) measurements.

Figure 20 shows the FSPs used in this study. Whilst the weight and dimensions vary, the shape remains the same. They are all cylindrical with a chisel nose, and commonly used in the ballistic testing textiles and laminates, which are usually employed as fragment protective armours. In this work they were used in the experimental measuring of the V_c's of the unfaced laminates and the testing of the polycarbonate samples.

3.3 Testing and Measurement Methods.

3.3.1 Bullet Firing

Figure 21 shows the equipment used to fire the bullets. It consists of a solid steel pressure housing into which a barrel of the required calibre is fitted via a universal adapter. The calibre chosen for the bullets used this work was 5.56mm The system was constructed to allow single shot firing only.

3.3.2 Fragment Firing

The same pressure housing was used for firing Fragment Simulating Projectiles (FSPs) as was used to fire bullets. A 7.62mm calibre barrel was used, and the FSP was placed inside a polyethylene sabot figure 22, then slid down the barrel. This was followed by a cartridge case without a bullet, charged with an amount of propellant to give the FSP the required velocity. The maximum achievable velocity for FSPs using this method was about 600 m/s. When the sabot and FSP were fired from the barrel the sabot opened out, "butterflied", and separated from the FSP.

3.3.3 Velocity Measurement.

It is very important that the velocity of impact is known accurately. The velocity of the projectiles used was measured by interrupting two light beams. The first sent a pulse to begin a timer, and the second a pulse to stop it. The two beams were positioned 1 meter apart, and the velocity calculation was performed automatically. The target armour was positioned less than a meter beyond the final beam and it was known that no measurable change occurred in the projectile velocity.

3.3.4 Mounting Frames.

Three mounting frames were used during this study. The frame used for the radiograms is shown in figure 23. It supported the armour and gave an unobstructed view of the region behind the it. This was essential to record all the relevant information about the penetration. The armours were held in place using adhesive tape.

The frame used for the measurement of the Critical Velocities (V_c) of armours at oblique angles of impact is shown in figure 24. In order to vary the angle of incidence the armour support was pivoted, and the angles were set by rotating the frame to as required then the fixing arm as in figure 24. The direction of rotation shown in this figure was chosen so that as much as possible of the debris from the penetration of the armour could still be collected. The armours were held in place by adhesive tape.

A simple supporting frame was used in both the V_c measurement of the unfaced laminates and the penetration of the polycarbonate samples. This is shown in figure 25. It consisted of two upright square sections 25mm wide and 150mm apart. The samples were fixed in place using adhesive tape.

3.3.5 Flash Radiography System.

The X-ray system used in this work was a "Scandiflash 150kV", supplied by Scanitronix Hubsborg, S-755 90 Uppsala Sweden. It consisted of a 150KV X-ray tube with a tungsten target, a pulse generator, delay timer, triggering device, and control panel. The pulse of X-rays generated lasted 35ns, and each pulse had an intensity of 20mR at 100mm from the tube window on the maximum voltage setting, which was used throughout this work. The short duration of X-ray pulse was achieved by the rapid discharge of a large capacitor, initiated by the controlled breakdown of a compressed air dielectric. The source size was 3mm. Figure 26 is a schematic diagram of the individual components which made up the x-ray system.

The trigger unit was itself controlled by the delay generator. This allowed delays between the event trigger and X-ray flash to be varied from zero to one second in 1ms steps. The delay unit was checked using a transient recorder for both timing accuracy and additional delays introduced by the trigger unit itself. The pulse shape produced by the trigger unit was a sawtooth form, with a steep leading edge, and no additional delay was found to have been introduced.

Event triggering was done using a "foil" system. A "foil" was made from two pieces of aluminium baking foil attached to either side of a piece of paper using an "iron on" technique. A voltage was applied to one side of the "foil", and as soon as penetration occurred this caused a short circuit and triggered the delay unit. An initial trial was performed with the delay generator set to zero, and the "foil" itself the target for the X-rays. The radiograms showed that the equipment triggered when the bullet nose just appeared in contact.

Figure 27 shows the X-ray tube mounted on the stand and the position of the film cassette beyond the mounting frame. The frame in this picture was that used for holding armours when measuring the V_c at oblique incidence angles. The X-ray tube was mounted so that the beam of X-rays was normal to the impact direction, with the armour between the X-ray head and the cassette containing the film. This made the restriction that the ceramic facing had to be narrow enough to allow an image of the penetration to be recorded. This arrangement also introduced a degree of distortion which manifested itself as a magnification of the image. It was minimised by having the armour and film as close as practicable, and measurements taken from the radiograms were adjusted by a factor which was calculated from the measured

tile thickness and the true thickness.

3.3.6 Measurement of Critical Velocity

The Critical Velocity of a target of a specified areal density is defined as the velocity below which penetration by a specified projectile will not occur. The Critical Velocity of an armour type is measured by fixing a sample of that armour in front of a freely hanging pendulum, called a "ballistic pendulum". This pendulum is positioned so as to collect all the debris produced by a projectile penetrating that sample of armour. A long rod transducer attached to the rear of the pendulum measures its displacement following an impact. The maximum displacement recorded is displayed on a peak meter, and is related to the momentum of the impacting debris. The V_c measured is the result of shooting at several samples of the armour configuration at progressively lower velocities until an impact velocity is reached which does not achieve penetration. The velocities and resulting momenta are then fitted to the equation after Recht and Ipson (28).

$$M_r = a\sqrt{V_i^2 - V_c^2} \tag{3.1}$$

where M_r = Residual Momentum of projectile after target penetration
V_i = Impact Velocity of projectile
V_c = Critical Velocity
a = a constant related to the mass of the projectile and the mass of the debris collected.

This equation is based on an energy balance between the impact energy and the energy absorbed by the armour, and the energy remaining in the projectile after penetration. It is independent of the energy absorption mechanism of the armour.

Pendulum Calibration

The pendulum is calibrated by firing projectiles of known mass and velocity directly into the pendulum, and measuring the peak displacement produced. The resulting data are fitted by regression analysis to the equation:

$$M = Kd + C \tag{3.2}$$

where M = momentum
K = constant of proportionality
d = peak displacement of the pendulum
C = constant term related to pendulum sensitivity

This is used subsequently to calculate the momentum associated with each peak displacement measured. This calibration is dependant on the mass of the pendulum remaining approximately constant for the duration of the test. With the accumulation of debris within the pendulum as testing proceeded the weight gradually changed, so it was re-calibrated half way through each series of V_c measurements.

Maximising Pendulum Sensitivity

The sensitivity of the pendulum is important in determining the minimum residual momentum which can be measured by the system. Two arrangements of the ballistic pendulum and associated measuring devices were used. The sensitivity of the pendulum was not an issue in the measurement of the armour V_c's using bullets. However it was important when measuring the V_c's of the unfaced laminates, which required much greater sensitivity because very small residual momenta were anticipated. This arrangement is considered first.

The sensitivity is governed by the weight of the pendulum and the transducer, and the resistance to the motion of the transducer itself. The lightest pendulum available had a mass of 3.5 kg. The pivoting resistance of the transducer was quite significant when this pendulum was used, thus the transducer was rigidly supported, instead of

being allowed to pivot about a horizontal axis with a rocking motion, as it did when used with the heavier pendulum. It also remained uncoupled from the back of the pendulum, but was positioned hard against the pendulum back prior to each shot. The only remaining source of resistance was that to the motion of the transducer, which could not be reduced, but was low enough to be acceptable.

The arrangement adopted with the heavy pendulum, weighing 35kg, was similar with the following exceptions. The transducer was attached to the back of the pendulum and mounted in its pivot so that it could oscillate up and down allowing for the motion of the pendulum.

3.4 Materials and Armours

3.4.1 Ceramic Facing Materials

Several facing materials were used in this work. "Cooors AD-85" alumina, supplied by Coors Porcelain Company, Golden, Colorado USA. This was a composite material consisting of 85% alumina, with the balance made up of a continuous glassy phase surrounding the alumina grains. It was used only for the flash radiography, and so each tile was 50mm x 50mm x 5mm thick. The small size of the tile was chosen to allow penetration of the X-rays. In ballistic work materials are usually referred to by their areal density. This is defined as the weight per square meter of the material. Thus for a given material, varying the thickness varies the areal density. It is also a very convenient way of comparing the performance of two different armour systems. The mechanical properties of this material are presented in table 2.

A second alumina based material was used in the determination of the V_c's of armours. This was a 97.5% alumina material supplied by Morgan Matroc, Central Avenue,East Mosley, Surrey.. The plates were 150mm x 150mm. The mechanical properties of this material are given in table 3.

The other material used solely in the flash radiography work was ordinary Soda Lime window glass supplied by Kent Blaxhills, Colchester. The sample size used was

100mm x 100mm. The mechanical properties are given in table 4.

3.4.2 Laminate Materials.

Two backing materials were used, an aromatic polyamide laminate, also referred to as an aramid laminate, and a Glass Reinforced Plastic (GRP) laminate. The aromatic polyamide laminate was constructed from aromatic polyamide which had been woven into a square basket weave with an areal density of $0.223Kg/m^2$. This was laminated using Evode Thermoflo A6876 with an areal density of $60g/m^2$. It is a copolymer of Ethylene Vinyl Acetate. These backings were pressed at a temperature of 165 ° C and a pressure of $3.5MN/m^2$. They were cut to a final size of 150mm square. The areal density of laminates used depended on the application.

The GRP backings were used were made from glass fibre mating in an epoxy matrix, and cut to final dimensions of 150mm square. This material was chosen for its much greater stiffness over that of the aromatic polyamide laminates. Even though it has a higher areal density the ballistic performance is much inferior to that of the aromatic polyamide laminates.

3.4.3 Armour Construction

All the armours were assembled in the same way, the front was stuck to the backing using a room temperature vulcanising silicone adhesive. This was spread evenly over the rear face of the facing, then facing and backing were married up. A weight was placed on top of the armour while the adhesive set, to ensure a firm bond was formed. The only variation to this was a 1.25mm thick lead interlayer was used on the glass face aromatic polyamide armours, this was done because it was thought that the glass rubble projected into the backing at the impact site was not dense enough to show up on the X-rays. The lead was glued to the backing in the way described above, and the front tile was attached to the lead in the same way.

3.4.4 Polycarbonate

The material used in these tests was cut into squares 150mm x 150mm, supplied by Roehm, Makrolon Division, 18/19 Bermondsey trading estate, London. It was coated with a polysiloxane hard coating, which was a proprietary product supplied by Fulmer Yarsley Ltd., Trowers Way Redhill Surrey. Its trade name is "Lomarflex".

3.5 Tests Conducted and Materials Used

3.5.1 Flash Radiography

The system described in section 3.3.5 was employed to produce radiograms of three armour constructions impacted at a velocity of 1000m/s. The armours used were:

Facing Material	Thickness (mm)	Backing Material	Areal Density (kg/m^2)	Armour Areal Density (kg/m^2)
85% Alumina	5	Aramid	10	29.5
85% Alumina	5	GRP	13.8	33.3
Glass	6	Aramid	10	24.5

3.5.2 Ballistic Testing of Unfaced Laminates

The V_c of the aramid laminates was measured using the method detailed in section 3.3.6. 4.2. The V_c measurements were performed with FSPs, which were described in section 3.2.2., of the following weights 0.24g, 1.1g and 2.8g. The laminates, which were described in section 3.4.2., had these areal densities, 4.3 $\pm$ 0.25kg/m^2, 5.3 $\pm$ 0.25kg/m^2, 6.25 $\pm$ 0.25kg/m^2, and 7.9 $\pm$ 0.25kg/m^2

It was important that as wide a range of FSP sizes as possible were used. The minimum size was determined by the pendulum sensitivity. The momentum of the FSP at low velocities had to exceed the detection limit of the pendulum by a margin great enough to give confidence in the value of the V_c calculated. The lowest weight of FSP where this was possible was 0.48g. The greatest weight of FSP available was 2.8g. The weight of FSP nearest the mid-range of these two extremes was 1.1g. To eliminate any possible source of error, batches of each size of FSP were weighed, and only those of identical weight were used in the evaluation of the V_c's.

3.5.3 Testing of Armours at Oblique Angles of Impact

The V_c was measured according to the method described in section 3.3.6, using 5.56mm calibre bullets, as described in section 3.2.2, The armours were constructed from 97.5% alumina facing with an aramid laminate backing in the following combinations:

Facing Thickness (mm)	Facing Areal Density	Backing Areal Density	Armour Areal Density
2	7.6	3.8	11.4
3	11.4	5.7	17.4
4	14.6	7.3	21.9

These armours had there V_c's measured at 0°, 30°, 40°, 50°, 60°, 70°.

3.5.4 Study of Plate Bending

The coated polycarbonate, described in section 3.4.4, and the FSPs were chosen to examine plate bending because it was a material which could be penetrated without causing any significant distortion to the projectile. This was necessary to prevent additional factors entering into the results analysis and complicating it. It was known

that polycarbonate failed in a ductile manner, which was important if a permanent record of the bending was to be made, because the sample remained intact after penetration, which doesn't happen with brittle materials. The coating material was much more brittle than the substrate, and its yielding before the polycarbonate meant it could be used in this capacity.

2.9mm thick polycarbonate was used in this series of tests. Only the 1.1g size of FSP, described in section 3.2.2 was employed, with the method described in section 3.3.2.

Chapter 4

Results

This section presents the results of the visual examinations carried out, and the experimental measurements .

4.1 Visual examination of Armours.

4.1.1 Alumina facing with Aromatic Polyamide back

Every armour shot at was penetrated. The ceramic facings were completely destroyed, except for a few isolated fragments which remained stuck to the adhesive. This was because the area of disruption caused by the impact was greater than the size of the tile. When larger alumina tiles on similar backings are shot at some of the ceramic usually remains around the impact area.

A shallow indentation was observed on the front face of the laminate backing around the hole caused by the penetration, but the area disturbed on the back face was much larger, almost extending the full width of the laminate. The fibres around the hole had all been severed, and were protruding at roughly 90° to the plane of the

backing. There was no evidence of any matrix holding them together and they were all quite loose. Figure 28 shows the front of the armour, figure 29 shows the rear of the armour.

4.1.2 Alumina facing with GRP backing.

Every armour shot at was penetrated, and the ceramic was completely destroyed as in the previous series of armours. There was no evidence of a depression around the penetration hole, and the only disturbance on the back face was the split and disrupted fibres around the exit hole. There was definitely no gross distortion of the back face as observed in the previous case. Figure 30 shows the front face of the armour, and figure 31 shows the rear face. In this case the severed fibres around the exit hole have almost returned to there original positions, even though there appears to be no resin to hold them.

4.1.3 Glass facing with Aromatic Polyamide Laminate backing

The unusual orientation and larger original facing meant more of the facing remained intact, and so more detailed information could be obtained from a visual examination of the armour. There was evidence again of a depression around the penetration hole, with considerable disturbance of the rear face, similar to that portrayed in figure 28. Figure 32 shows the front face of the armour. The depression is obscured by the lead interlayer, but the examination of the remaining glass facing revealed that there was evidence of a fracture cone, but not in the orientation expected. The base of the cone was on the front face of the glass, instead of being adjacent to the backing. The fracture pattern around the penetration consisted of many radial cracks and was very similar to that described by Kolsky et al. (12). Very close examination did reveal a lip in the fracture very near to the lead lining. The pattern made by the cracks in the glass face can be seen in figure 32. They clearly radiate from the impact zone, and have travelled the thickness of the glass tile, because of the closeness of the cracks the fragments around the impact site are long thin slivers.

4.2 Radiographic Results

4.2.1 X-ray Distortion

The thickness of the ceramic and the length of the bullets were found to be greater when measured on the radiograms than was actually the case. The ratios between the measured and actual values for the bullets and ceramic were different, that for ceramics being greater. For the purposes of converting the measurements made on the radiogram to actual values, it was assumed that the magnification varied linearly as the projectile moved further from the axis of the X-ray tube. An empirical expression was produced which related these two values. The magnification factor for bullets (M_b) was found to be 0.84, calculated from 19/22.5. The magnification factor for the ceramics (M_t) was calculated by dividing the actual ceramic thickness by the measured ceramic thickness. The value for each individual measurement was calculated from the following expression.

$$M = M_b - 22.5\frac{M_b - M_t}{22.5 - L} \tag{4.1}$$

where
M = Calculated Magnification Factor
Mt = Measured magnification of the ceramic
Mb = Measured Magnification of the Bullet
L = Length of the Projectile Remaining

The value M in equation (4.1) was used to adjust the dimensions measured on the radiograms.

4.2.2 Measurements taken from the Radiograms

The measurements taken from the radiograms are detailed in tables 5 to 16. They are grouped in armour types, however it is more convenient below to treat them in groups all relating to a single common feature. Some operations are common to all tables in this series. Where a column is referred to as "Adjusted" then the values it contains include the compensation for the distortion discussed in section

4.2.1. Several tables have a column headed "Measured Tile Thickness", these are the individual measurements of the thickness of the ceramic used in calculating the compensation factor. Columns referred to as "Averaged" contain results which have been averaged over each time delay. A linear regression analysis was performed on two columns of data in each table, the values predicted by the resulting equation are presented in the column headed "Fitted", and are compared to the original data in the column headed "Percentage Variation" which is calculated from 100 x (Actual value - Predicted Value) / Actual Value . The accuracy of the comparison was also checked using Pearson's correlation coefficient "r", which is presented at the foot of each table along with calculated gradient and intercept of the fitted equation.

Tables 5,6,7: This group of three tables all refer to the erosion of the bullet as it penetrates through the ceramic. The column headed "Measured Projectile" contains the measurements of the length of the projectile remaining undistorted. The linear regression was carried out between the average time and the average adjusted measured projectile.

Tables 8,9,10: These tables all refer to the penetration of the projectile through the ceramic. The values for the penetration measured on the radiogram are presented in the column headed "Measured Pen". The linear regression was carried out between the average time and the average adjusted penetration.

Tables 11,12,13: These tables present the data relating to the displacement of the rear of the projectile as the ceramic is penetrated. The position of the projectile rear with respect to the surface of the ceramic (S) is calculated by subtracting from the original bullet length the difference between the adjusted length of the projectile (L) and depth of penetration into the ceramic (D) and , shown below

$$S = 19 - (L - D) \tag{4.2}$$

The development of this expression is shown in figure 33. The linear regression was carried out between the average time and the average adjusted rear displacement.

Tables 14,15,16: These tables present all the data relevant to the expansion of the projectile tip as it penetrates through the ceramic. The measured diameter of the distorted bullet tip is given in the column headed "Bullet Expansion". In order to calculate the radius of the distorted tip the values in this column were divided by 2,

and are presented in the next column. The linear regression was carried out between the average adjusted penetration and the average adjusted radius.

4.2.3 Cone Angle Measurements.

A fracture cone was visible only on the radiograms of the alumina faced aramid backed armours, see section 4.1.1. These results are presented in table 17. The same interpretation for the column headings was adopted as in tables 5 to 16. The cone diameter was defined as the difference between the diameter of the spreading of the bullet tip and the diameter of the base of the shaded region penetrating into the backing from the ceramic. These measurements were compensated for distortion in the same way as described in section 4.2.1.

The angle was calculated is shown as θ in figure 34. In the cases where bullet distortion had occurred before fracture of the ceramic was visible, leading to negative angles, were discarded. The angles which were used in the analysis are marked with a "*".

4.3 Ballistic Testing of Unfaced Laminates

4.3.1 Visual Examination

Each laminate that had been penetrated had an identical perforation. The yarns in the path of the penetrating projectile appeared to have split, and had little resin remaining on them. In most cases the severed yarns had returned to their original positions and there was no evidence of a plug of material removed from the hole. The only material missing was the resin.

There was little distortion of the laminate other than a small cone around the perforation except in the case of the two thinnest laminates penetrated by 2.8g FSPs.

These had a clear cross which indicated that either a pyramid had formed or bending had occurred, during penetration.

4.3.2 Experimental Measurements

Table 18 gives the experimentally measured V_c's for each combination of laminate areal density and FSP size. The actual weight of each size of the FSPs used in these measurements are presented in table 19.

4.4 Armours at Oblique Incidence

4.4.1 Visual Examination

These armours, when penetrated usually had some ceramic still adhering to the backing. As the angle of incidence increased the amount remaining was reduced. The parts remaining were above the penetration because the ceramic below was detached from the backing by the horizontal component of the force of the bullet hitting the armour. This is not found in armours impacted at normal incidence.

4.4.2 Experimental Measurements

The experimentally measured Critical Velocity (V_c) and angle of obliquity were recorded and are presented in table 20. It was not possible to measure V_c's for armours with an areal density of 11.4kg/m^2 below an angle of 40°.

4.5 Plate Bending Studies

4.5.1 Visual Examination

Two types of penetration were found. In samples which had been penetrated below about 430m/s there was a clear concentric ring structure on the rear face, with a little evidence of gross plastic distortion around the perforation. The front face of these samples had a star burst pattern of radial cracks. Samples which had been perforated above about 430 m/s had no visible ring structure on the rear face, but did have a substantial amount of material piled up forming a lip. There was also no evidence of a star burst of radial cracks on the front face.

4.5.2 Experimental Measurements

The measurements of the fracture ring radius taken from the plates of polycarbonate are recorded along with the velocity of impact in Table 21.

4.6 Bullet Shape

It was important to know the radius of the bullet as it was eroded. This changed, especially near the tip, because of the ogive, or curved shape. The distance from the bullet nose (L) was measured at nineteen points in steps of one millimetre on a straight line taken from nose to base.

$$y = 0.4249 + 5.751 * 10^{-1}L - 6.237 * 10^{-2}L^2 + 3.788 * 10^{-3}L^3 + 9.66 * 10{-}5L^4 \quad (4.3)$$

where L = Distance from the bullet tip.

This equation (4.3) is a truncated version of the original 9th order equation fitted as described. It was used to predict what the radius should be at each of these

distances and the predicted value was compared with the actual value. The accuracy of the prediction was checked using Pearson's correlation factor "r", which was found to be 0.99. The shape of the bullet is shown in figure 19. The measurements of the bullet circumference are recorded in table 23.

Chapter 5

Discussion of Radiogram Results

In this section the measurements taken from the radiograms are discussed. It was found that the Bernoulli equation for the stagnation point could be applied to describe the erosion of the bullet.

5.1 Graphical Presentation of Results

Figure 35,36,37: Bullet Erosion During Penetration of the Ceramic Facing v Time for the three armour combinations. The gradient of these graphs are given in tables 5,6 and 7. It represents the rate of erosion of the bullet, in mm/μs, as it passes through the hard facing on the armour, and as such is an important feature of the defeat process. The intercept is an indication of the experimental errors present in the measurements, the value should be 19mm, the undistorted length of the bullet used in this work. The agreement between the fitted line and adjusted results is quite good, and indicates a linear relationship between the degree of erosion and the time, which is named erosion velocity.

Figure 38,39,40: The Penetration of the Bullet Remains into the Ceramic facing v Time for the three armour combinations. The gradient of these graphs, given in

tables 8,9 and 10 is the velocity of penetration of the interface between the distorting bullet and the ceramic. Physically this represents the speed with which the bullet penetrates through the ceramic. The units are mm/μs for this velocity, and in all cases is substantially less than the impact velocity. The intercept of the graphs is an indication of the experimental errors, because it should be zero. The agreement between the fitted straight line is quite good.

Figure 41,42,43: Displacement of Bullet Rear v Time for the three armour combinations. The gradient and intercept for the fitted lines of these graphs are presented in tables 11,12 and 13. The gradient of the line represents the velocity of the rear of the projectile. Since the velocity of elastic waves in lead is 3.635mm/μs (3635 m/s), and the whole event lasts only 12μs, then the elastic wave would have time for only two reflections from the rear of the projectile during the whole penetration. This is insufficient to reduce the velocity of the projectile rear significantly. This was supported by the values calculated for the velocity of the projectile rear. In the case of the alumina faced GRP backed, and glass faced aramid laminate backed armours this value was very close to 1mm/μs (1000m/s), the impact velocity used in the testing. This meant that the assumptions made in producing the correction equation were valid, and that the adjustments applied to the "as measured" data are of the correct magnitude.

Figure 44,45,46: Sideways Expansion of the Bullet v Depth of Penetration for the three armour combinations. The gradient and intercept values for these three graphs are presented in tables 14,15 and 16. The data lie on a straight line, the gradient of which is the tangent of the half angle of the apex of a cone. For the alumina aramid armours this is 46° and for the alumina GRP armours it is 50°, however for the glass aramid armours it was only 26°. The intercept should be the radius of the undeformed bullet tip, which was 1.002mm. The intercept of the alumina faced GRP backed armour is 1.68mm. This apparently very high error in the value for the tip diameter is a consequence of the small numbers involved than real inaccuracy in the measurements.

5.2 Discussion of Bullet Erosion

There has been a lot of effort expended on studying the penetration of metal targets with deformable projectiles. However, it is quite novel to apply these ideas to ceramic composite armours. Metallic armours combine strength with ductility in the same material, whereas ceramic composite armours have the two properties of strength and ductility segregated in the front and back respectively. This made it very difficult to apply the theories for metallic armours, which considered the armour as a monolithic structure, to ceramic composite armours, which were clearly not monolithic.

Many of the theories which describe the penetration of metallic armours are based on the Bernoulli equation for pressure equilibrium at the stagnation point. The derivation of this equation is described in a paper by Wilson et al (29), and the equation is as follows:

$$\frac{1}{2}\rho_t u^2 + R = \frac{1}{2}\rho_p (v-u)^2 + Y \tag{5.1}$$

where
ρ_t = Density of the target material
ρ_p = Density of the projectile
u = Penetration velocity of the stagnation point
v = Impact Velocity
R = Strength of the target material
Y = Strength of the projectile

The known or calculated values for alumina and glass were substituted into the right hand side of this equation. The values are shown in table 4.

The following values for the projectile were substituted into the left hand side of the equation.

Projectile Density	$11.5 * 10^3 \text{kg/m}^3$
Impact Velocity	1000m/s
Projectile Strength	0.02MN/m^2

The value for the left hand side of the equation was calculated for each armour combination, and compared to the value calculated for the right hand side of the equation in table 23

There is clearly close agreement between the values calculated for both sides of the equation, and this is strong evidence that the Bernoulli equation can be applied to the erosion of projectiles as the ceramic is penetrated. The large variation between the values for the left hand side and right hand side of the equation for the alumina / GRP armour combination can be explained by the fact that the GRP backing showed much less distortion around the penetration hole. The rigidity of the GRP backing is higher than that of the aramid. This indicated that the backing rigidity does have an influence on the penetration performance of the ceramic but not as previously proposed to delay ceramic bending. Its effect appears to be to contain the crushed ceramic and enable it to support a greater load than in the unrestrained state. This is supported by work done by Wilkins (17), which showed that ceramics could continue to support a load, even after failure of the ceramic, when subjected to triaxial compression. The magnitude of the load supported was related to the confining pressure. The situation in the armour is clearly similar, with the backing and the surrounding unbroken ceramic providing the confining pressure. The rigidity of the backing will govern the magnitude of the confining pressure. Thus it is indicated that for the general case an additional term should be added in the right hand side of equation (5.1) to take account of backing rigidity.

The role of the backing is to be one of providing a confining pressure at the rear of the ceramic as it is penetrated. However it appears possible to treat the ceramic and the backing as separate entities when the backing does not provide a significant confining pressure, as in the case of the aramid laminate backings most commonly used in high velocity protective armours.

5.3 Energy expended during penetration

Bullet distortion occurs due to the resistance of the material to penetration by the projectile. Pressure is generated in the projectile which is relieved by it yielding and flowing plastically sideways. Much work has been done on the subject of impacting rods. This is covered in some detail by Graff (7, pp100–108). The initial force

generated during the impact of a rod is given as

$$F = \frac{-Z_t V_0}{1 + Z_t/Z_p} \tag{5.2}$$

where t = target material
p = projectile material
Z = Elastic Impedance of the material given by ...

$$Z = A\sqrt{E\rho} \tag{5.3}$$

where A = Area of contact
ρ = Material density
E = Material Young's Modulus.

In these expressions the assumption has been made that the area of the ceramic involved in the impact is equal to the area of the distorted tip of the projectile at any instant.

The energy expended during the penetration of the ceramic is calculated from

$$E = Fs \tag{5.4}$$

where E = Energy
F = Force, calculated as above
s = Distance travelled

Substituting equation (5.3) into equation (5.4) gives:

$$F = \frac{-Z_t V_0 s}{1 + Z_t/Z_p} \tag{5.5}$$

It should be possible to check the validity of equation (5.5) by using it to calculate the energy expended. These values can be compared to the values calculated from the measurements of the physical parameters. Table 24, 25 and 26 give the bullet radius as the bullet is eroded, as calculated in table 22, for each armour combination. From this the area of the bullet was calculated, and this was used along with the depth of penetration into the ceramic and the acoustic impedance to calculate the energy. The value for the acoustic impedance was calculated using the values for the physical properties of the alumina given in table 2

The figure finally arrived at as the energy expended by the bullet during the penetration of the ceramic was calculated by averaging all the none zero values. This was justified because of the curvature of the bullet profile varied the presented area as the bullet was eroded. By averaging the values it approximated to a rod impacting the surface of the ceramic. This final figure was used as the energy used to deform the projectile as it passed through the ceramic. This figure was compared to one calculated from the average length of the bullet remaining at the final time delay and the velocity it was known to have, 1000m/s. Fortunately the part of the projectile remaining in all three cases is almost cylindrical , but the average diameter of the projectile, as calculated from table 22 for the length remaining, was still used. Thus the calculation of the energy contained within the projectile can be calculated easily. This value is also presented in the tables. In the two alumina faced armours the agreement was fairly close. However, the glass faced armour was not in such close agreement. That the two values agreed as they did for the alumina faced armours was not expected, and may be a coincidence. For the foregoing to be correct it suggests that the ceramic retains its acoustic impedance after crushing. It is also unexpected that the equation holds under these conditions, because it is intended for use where the deformations are small and elastic, not plastic and quite large. It is possible that the ceramic was compacted enough, even after failure, to retain a similar acoustic impedance.

Chapter 6

Ballistic Behaviour of Aramid Reinforced Laminates

This section describes the theory of penetration of fibre reinforced laminates. No theory describing the penetration of a laminate panel by a projectile could be found in the literature and so this one was developed from the Recht and equation (28), presented earlier as equation (6.1). The experimental results were analysed and found to agree with the theoretical approach.

6.1 Theory

The expression for calculating the Critical Velocity of a target is given by Recht and Ipson (28) as

$$M_r = a\sqrt{V_i^2 - V_c^2} \tag{6.1}$$

where M_r = Residual Momentum
V_i = Impact Velocity
V_c = Critical Velocity
a = a constant related to the mass of the projectile and the mass of the debris collected.

When the incident velocity (V_i) is equal to the critical velocity (V_c), then the residual momentum (M_r) is zero. The laminate absorbs all the energy of the FSP if it is not penetrated. Therefore the maximum energy which a laminate can absorb can be calculated from

$$E_{\max} = \frac{1}{2}mV_c^2 \tag{6.2}$$

where E_{max} = Maximum energy absorbed.
m = projectile mass

It is known that in the case of plugging the energy absorbed is a function of the circumference of the projectile. The penetration process in this case did not involve the removal of a plug of material from the laminate. This was established both visually, and by examining the values for the constant "a" calculated when the individual V_c's were calculated,presented in table 19. These values were very close to the weight of the FSP used in the test, indicating that only the FSP had entered the pendulum.

Thus it is suggested that initial steps in developing a method of predicting the ballistics performance is that the energy absorbed by the laminate is a function of the volume of material involved in the penetration process. This volume has been calculated from the target thickness and the contact area of the FSP. It is also proposed that the energy absorbed by the laminate is spread evenly throughout this volume, giving rise to the concept of a maximum energy density (E_c), expressed in J/m^3. Thus the maximum energy which can be absorbed by a laminate of known construction when challenged with a specific projectile can be calculated from

$$E_{\max} = E_c A t \tag{6.3}$$

where A = Contact area of the projectile
t = Target thickness.

This may be an over simplification, because the impact may distribute the energy throughout a much greater volume of the target than is suggested by this expression. However if it assumed that the two volumes of material bear a constant relationship to each other, then using the simple volume calculated above should not introduce any significant errors. Substituting equation (6.2) into equation (6.3) gives:

$$\frac{1}{2}mV_c^2 = E_cAt \tag{6.4}$$

rearranging gives:

$$V_c = \sqrt{\frac{2E_cAt}{m}} \tag{6.5}$$

In the case of laminate armours any contribution by the resin to the ballistic performance is ignored. Therefore the ballistic performance is a function of the number of layers of the reinforcing material, rather than just the laminate thickness. Thus in the above expression the thickness (t) should be replaced by the number of reinforcing layers (N). This changes equation (6.5) to

$$V_c = \sqrt{\frac{2E_cAN}{m}} \tag{6.6}$$

The areal density of a single layer of reinforcement and resin is taken as 0.28kg/m^2. Therefore the number of layers is related to the areal density (D) of a laminate by

$$N = D/0.28 \tag{6.7}$$

substituting equation (6.7) into equation (6.6) gives as the final expression relating the V_c to the areal density of a laminate of known construction.

$$V_c = \sqrt{\frac{2E_cAD}{0.28m}} \tag{6.8}$$

6.2 Application to Experimental Results

The theory presented above was applied to the experimentally measured V_c values for several different areal densities of laminates, challenged with several different sizes of FSPs. Table 27 gives the energy absorbed by laminates of each areal density. Table 28 gives the energy absorbed per layer for the same laminate areal densities. The average values for the energy absorbed per layer for each FSP type were found to be:

0.48g	FSP:	2.78 J/layer
1.1g	FSP:	4.296 J/layer
2.8g	FSP:	8.449 J/layer

The contact area of each FSP type, as calculated from the data in figure 20, were found to be:

0.48g	FSP:	8.242mm^2
1.1g	FSP:	13.665mm^2
2.8g	FSP:	23.723mm^2

Dividing the energy absorbed per layer by the contact area of the relevant FSP gives the maximum energy density (E_c), which was calculated to be:

0.48g	FSP:	0.329 J/mm^2/layer
1.1g	FSP:	0.314 J/mm^2/layer
2.8g	FSP:	0.356 J/mm^2/layer

Thus the average maximum energy density is 0.336 J/mm^2/layer. Substituting this value equation (6.8) will allow the V_c's for each laminate FSP combination to be calculated. These results are presented in table 29, along with the values measured for each combination. The final column is the % variation, calculated as the difference between the measured and calculated values, divided by the measured value. Only three results exceed 5% variation. It may be significant that these are the results for the thinnest laminates. A graphical representation of these results is given in figure 47. There is clearly a departure from the predicted line for the two lowest areal density laminates when challenged with the 2.8g FSP. This is attributed to the evidence of bending found when they were examined. This energy absorbing mechanism has not been included in the calculations carried out.

6.3 Comparison with Plugging Failure.

To establish that materials which are known to fail by plugging behave in a different manner to that discussed above, the Critical Velocity for several areal densities of Polycarbonate challenged with 1.1g FSPs were also measured. These results are presented in table 30, and included in figure 47. The polycarbonate can be seen to behave very differently from the laminates.

6.4 Limits of the Predictive Model.

A close study of table 28 shows that there may be a trend towards an increase in the energy absorbed per layer as the areal density of the laminate increases. This may be due to a contribution by the resin to the energy absorption of the laminate, which was assumed zero in all cases. Alternatively the volume of material through which the energy is distributed during penetration may become larger in thicker laminates because of the increasing penetration time, and so allow more energy to be absorbed. Since the effect is quite small in laminates below $10kg/m^2$, it has not been pursued further, but an upper limit of $10kg/m^2$ is suggested for the model.

Chapter 7

Ballistic Performance of Armours Impacted at Oblique Angles

This section discusses the results of Alumina aramid composite armours when impacted at angles of increasing obliquity. An empirical relationship is developed which helps in predicting the Critical Velocities (V_c) of the armours at varying areal densities, and angles of incidence against 5.56mm L3A1 ammunition. No models for the performance of armours at oblique angles of attack have been found in the literature so one is proposed below.

7.1 Analysis of Results

As the armour is rotated then the depth through which the projectile must penetrate is proportional to the secant of the angle of rotation. This is shown in figure 48. The relationship is given as

$$t' = t \sec\theta \tag{7.1}$$

where t' = apparent thickness
t = actual thickness
θ = angle of incidence of the bullet as shown in figure 48

It was shown in section 5.2 that the length of bullet eroded is governed by the depth of ceramic penetrated, which in this case is given by the apparent thickness (t'). The relationship between the ballistic performance of the aramid laminate backing was presented in section 6.1, equation (6.6) as

$$V_c^2 = 2A(0.336)N/m \tag{7.2}$$

where V_c = Critical Velocity
A = Area of projectile tip after penetrating the ceramic
N = The number of layers of aramid.
m = Mass of the impacting projectile which in this case is the mass of the bullet remaining after erosion by the ceramic.

The value calculated for E_c in section 6.2, 0.336 J/mm^2/layer was used in equation (7.2).

The construction of the a ceramic and of a laminate are fundamentally different, and this has a major influence on how they react when impacted at oblique angles of incidence. The ceramic facing is a monolithic material, allowing the waves generated by the impact to spread out in all directions. Therefore as the angle of incidence increases the apparent thickness does so also. The laminate construction is one of many layers of textile in a plastic matrix. In section 6.4 it was stated that the matrix was assumed not to contribute to the ballistic performance of the laminate. The energy entering the laminate does not have the freedom to move in any direction, as in the ceramic, but remains restrained to the layers of textile. Thus changing the angle of incidence will not change the number of layers available to absorb the energy. The study concentrates on the apparent thickness of the ceramic, with the performance of the laminate governed by the number of layers only.

Since the values for A and m are a function of the apparent thickness ($K(t')$), and so it is possible to rewrite this equation as:

$$V_c^2 = NK(t') \tag{7.3}$$

$K(t')$ also represents the distortion and destruction of the bullet by the ceramic tile

as it is penetrated. Rearranging equation (7.3) it can be shown that

$$V_c^2/N = K(t') \tag{7.4}$$

Table 20 gives the values for the impact velocity, the apparent thickness and the value for K(t').

7.2 Empirical Relationship Between K and Apparent Thickness

An empirical power law relationship was found to exist between K and the apparent thickness (t') as shown below

$$K = C(t')^a \tag{7.5}$$

Substituting equation (7.1) in equation (7.5) gives

$$K = C(t \sec\theta)^a \tag{7.6}$$

The values given in table 20 for the constants C were found by regression analysis.

The values for the 11.4kg/m^2 and 17.1kg/m^2 armours are very close, which suggests they are the product of the same mechanism. However the values for 21.9kg/m^2 armours are substantially different, which indicates that there may be a different mechanism at work in tiles of this thickness.

The value for the constant a was chosen as 0.5. Thus equation (7.6) becomes

$$K = C(t \sec\theta)^{0.5} \tag{7.7}$$

Substituting this equation in to equation (7.3) gives

$$V_c^2 = NC(t \sec\theta)^{0.5} \tag{7.8}$$

taking the square root of both sides gives

$$V_c = \sqrt{NC}(t \sec\theta)^{0.25} \tag{7.9}$$

The results for the 11.4kg/m^2 and the 17.1kg/m^2 armours, shown in figure 49 can be divided into two separate zones. One which behaves as described above, called type I behaviour, and one which occurs at lower angles of incidence, and is named type II behaviour. This type of behaviour is discussed in section 8. Table 20 does not include values for the constant C for these two thicknesses at these angles of incidence.

The analysis of the results yielded two values for each of the constants C and a. The value for C of 10222 and that for a of 0.5 fitted the linear portion of the results for the 11.4kg/m^2 and 17.1kg/m^2 armours very well. However values of 20336 for C and 0.25 for a were found to fit the entire set of results for the 21.9kg/m^2 armours.

The line corresponding to equation (7.9), with the value 10222 assigned to C and 0.5 assigned to a, has been drawn through the results for 11.4kg/m^2 and 17.1kg/m^2 armours in figure 49. There is good agreement, and this is further demonstrated in table 20, which presents the actual results, predicted results, and the % variation. The measured values of the V_c's at higher angles of incidence were above the predicted line. This can be explained with reference to the observations that the lower part of the ceramic facing was removed during the impact. The additional energy required to do this will result in the slightly high V_c.

Table 20 also presents the actual and predicted results for the 21.9kg/m^2 armours. The predicted values for this armour were calculated using the value of 20336 for the constant C as given in table 20. There was no evidence of any type II behaviour, and the gradient of the line, dependant on the constant C is lower than that found in the two previous sets of results.. This may indicate a difference in the mechanism of penetration between the 4mm thick facings and the thinner ones. The variability in the value taken the constant C is referred to in section Section 10.4.

Chapter 8

Plate Bending

This section examines the proposal that the ceramic facing of armours undergoes bending as a result of the impact of a projectile. Two sets of plate equations are reviewed, and the behaviour predicted by both sets compared. From which one set is studied further and is applied to experimentally measured data of armour behaviour. This demonstrates that there is a critical velocity associated with each plate thickness, above which bending waves will not propagate through the plate. This is an extension of the current understanding of ceramic plate failure as a consequence of ballistic impact.

8.1 Theory

8.1.1 Classical Plate Equations

The derivation of the classical equations which describe the bending motion of a plate when impacted in the centre is presented by Graff (7, pp 229–244). These equations are based on a consideration of the stresses and moments acting on the body. The expression relating the frequency and wave number for low wave numbers is:

$$c = \sqrt{D/b\rho\gamma} \tag{8.1}$$

where
- c = wave velocity
- b = thickness
- ρ = material density
- γ = wave number
- D = Rigidity Modulus of the material given as $D = Eb^3/12(1-\nu^2)$
- E = Young's Modulus
- ν = Poisson's ratio for the material

Remembering that $\gamma = 2\pi/\lambda$, (where λ is the wave length). It is clear there is no short wavelength limit to this expression, thus as the wave length decreases the velocity of propagation increases, infinitely. This is obvious nonsense and is the product of the original assumptions and neglect of the rotary inertial and shear effects. However the theory in this form has been used successfully by Medick (30) to investigate the transverse motion of plates of thin aluminium subjected to impact by a .22 bullet. A set of conditions not apparently dissimilar to this work. These experiments did in fact show close agreement between the predicted and measured motion for the plates. Further confirmation of the bending motion induced in plates by various forms of impact on the surface of plates has been provided by several other workers (31,32). This all supports the proposal that the ceramic plate bends upon being impacted by the bullet, and failure only occurs when the backing yields allowing the plate to deform and so fracture

8.1.2 Exact Plate Equations

There is an alternative to the Classical equations, the Exact Plate equations. The derivation of these is also given by Graff (7 , pp 432–460). These equations are based upon the equations of elasticity and are considerably more complex than the classical plate equations. The relationship between the phase velocity and wave number is divided into three regions. These expressions are given below:

Region 1

where the $\gamma > wc_2$, which means that the wave velocity is below that of the shear wave velocity.

$$c = \gamma b \sqrt{\frac{E}{3\rho(1-\nu^2)}} \tag{8.2}$$

where c_1 = Dilational wave velocity
c_2 = Shear wave velocity
E = Young's Modulus
ρ = material density
ν = Poisson's ratio for the material
γ = wave number
ω = frequency

Region 2

where $w/c_2 > \gamma > w/c_1$, which means that the wave velocity falls between that of the shear wave and dilatational wave velocities.

$$c = \sqrt{\frac{E}{\rho(1-\nu^2)}} \tag{8.3}$$

Region 3

where $w/c_1 > \gamma$ which means that the wave velocity exceeds that of the dilatational wave velocity. This region is not involved in the behaviour discussed here.

Equation (8.2) describes the bending waves travelling through a flat plate. This shows a linear relationship between the velocity of propagation and the wave number. It is the relationship which was derived in the previous section for the classical plate theory for flexural waves. From the previous definition of the regions concerned with the solution to these equations, it can be seen that the flexural waves have a limited

range of existence. As the wave number tends to infinity, or the wavelength becomes shorter the expression reduces to that for Rayleigh surface waves. This happens because at short wave lengths even a finite thickness plate appears to be semi-infinite to the wave. It should be stated that these equations are for the propagation of established wave trains, as would be found some distance from the point of impact on a target. However it is clear that flexural waves only occur in flat plates above a critical wavelength.

Returning to equation (8.2), it was shown that it was only applicable when $\gamma > w/c_2$, or $c < c_2$, then a transition to the behaviour described by the equations governing region 2. If the transition occurs when $c = c_2$, and remembering that $\gamma = 2\pi/\lambda$, then equation (8.2) can be rewritten as

$$c_2 = \frac{-b}{\lambda_t}\sqrt{\frac{E}{3\rho(1-\nu^2)}} \tag{8.4}$$

$$c_2^2 = G/\rho \tag{8.5}$$

where G = Shear modulus

λ_t = The transition wave length

squaring both sides of equation (8.4) and substituting equation (8.5) into it gives

$$G/\rho = \frac{b^2 E}{\lambda_t^2 3\rho(1-\nu^2)} \tag{8.6}$$

$$\text{But} \quad G = E/2(1+\nu) \tag{8.7}$$

Therefore substituting equation (8.4) into equation (8.5) and factorising $(1-\nu^2)$ as $(1-\nu)(1+\nu)$ then re-arranging gives

$$\lambda_t^2 = \frac{2b^2}{3(1-\nu)} \tag{8.8}$$

$$\Longrightarrow \quad \lambda_t = b\sqrt{\frac{2}{3(1-\nu)}} \tag{8.9}$$

As the wave length at which bending waves cease to exist.

When a projectile impacts a surface the pressure rises from zero to a value determined by the impact velocity. The shape of this curve can be analysed by Fourier

analysis, generating the frequency spectrum for the curve. The pressure curves for impacts are known to become steeper as the velocity increases (7 , p 108), and so the fundamental frequency of the Fourier spectrum will move to higher frequencies. The foregoing analysis states that only those components below a critical frequency, or a wavelength greater than the transition value will propagate as bending waves, and the remainder are confined to the impact surface, as surface waves.

From equation (8.9) the critical frequency is inversely proportional to the plate thickness. For thin plates this frequency is high, so that bending will occur up to quite high frequencies, but as the thickness increases then the wavelength at which bending can occur gets longer also. A longer wavelength means a lower frequency. In the extreme a semi-infinite block of material will have a critical frequency of zero, in other words no bending can possibly occur and most of the energy is transported by surface waves, as was demonstrated by Miller and Pursey. Equation (8.9) appears to be dependant only upon the Poisson's ratio of the material. This agrees with the observations of penetrations of metallic armours where the failure mode is dependant upon thickness. Thick plates fail by either spalling or the formation of adiabatic shear bands, while thinner specimens fail by petalling. The formation of petals indicates the presence of bending, whilst spallation of shearing suggests another mechanism.

8.2 Discussion of Experimental Results

8.2.1 Polycarbonate Targets

The expressions presented above gives an equation which implies that a wavelength exists above which bending waves can not be present in a plate of a given thickness. This was demonstrated by impacting, with FSPs, pieces of polycarbonate, which were coated with a brittle polysiloxane . This coating failed at a stress below the yield stress of the bulk polycarbonate, thus it can maintain a permanent record of the gross elastic deformation of the substrate. The surface waves generated by wavelengths less than the threshold have a much smaller amplitude and are unlikely to break the surface coating.

A graph of the results is presented in figure 50. The diameter of the rings found

started at 25mm for an impact velocity of 158m/s reducing to 15mm for an impact velocity of about 320m/s. At the lowest two velocities penetration did not occur, but rings were still formed. Above this threshold value all evidence of the circles of fracture vanished, which agreed with the proposed behaviour. It is assumed that the frequency profile remains the same for all impact velocities, but moves up the frequency scale as the impact velocity increases. Thus an impact velocity is reached where the fundamental frequency is above that where bending can occur.

The increasing diameter of the rings with decreasing impact velocity is unimportant and probably connected to the increased time of penetration. The maximum diameter reached with any impact velocity will be governed by the decay of the wave as it radiates outward from the impact point.

Unfortunately it is not possible yet to either measure or predict the exact pressure pulse shape produced by the impact of the FSP on the plate. However the observations do agree with the proposed theory, and it also explains the observations made by Medick on the bending of thin plates impacted by .22 bullets. This type of projectile is much slower than the 5.56mm rounds in this work, and the .30inch calibre rounds in Wilkins work. Additionally it provides an explanation for why thin plates are seen to produce petals when they are penetrated at almost any velocity.

8.2.2 Alumina Composite Armours at Oblique Incidence

The experimentally measured V_c's for alumina faced aramid laminate backed armours impacted at varying angles of obliquity were presented in figure 49 of Section 7.2. The results for the two lowest areal densities considered, 11.4kg/m^2 with 2mm thick alumina, and 17.1kg/m^2 with 3mm thick alumina, exhibited two distinct types of behaviour. That exhibited by the higher angles of incidence, type I, was discussed in section 7.2. However it was not possible there to provide an explanation of the cause of the departure from the predicted line, type II behaviour. Now that bending of plates has been discussed, it is possible to begin to explore the causes of this type of behaviour.

It is suggested that when the apparent thickness of the ceramic, which was discussed in the previous section, is below a critical value bending waves can exist.

Bending waves travelling through a ceramic plate will induce a tensile stress on one of the surfaces. Since alumina is considerably weaker in tension than compression this means the plate will suffer premature failure.

The two possible transition points between the two behaviour zones are joined by a line in figure 49. The apparent thickness of the alumina facing at these two points are 3.11mm for the 11.4kg/m^2 (2mm alumina) armour corresponding to an angle of 50, and a secant of 1.55, and approximately 3.3mm for the 17.1kg/m^2 (3mm alumina) armour, corresponding to an angle of 25°, and a secant of 1.1. This suggests that the transition from type I behaviour to type II behaviour occurs at approximately the same apparent thickness for both armours.

Figure 51 shows the graph of the ballistic performance against the areal density. The performance of the armours falls off rapidly as the areal density is reduced. However it can be shown if the values for ballistic performance calculated for the type I behaviour, using the method outlines in section 7.1. for zero degrees obliquity, then these results fall on a straight line. This is evidence for a change in mechanism below a critical facing thickness. The transition point is at 3.2mm.

Thus bending cannot be excluded as a failure mechanism in ceramic composite armours. It is shown here that under some circumstances bending could occur. Therefore the phenomenon of bending should be studied further to find what factors control whether it occurs or not.

Chapter 9

Discussion of observed features

The aim of this section is to examine the observations made in this work or reported by others with a view to advancing possible explanations of the causes, which have not been previously proposed.

9.1 Fracture Cone and Cone Angles

Fracture cones are a regular feature of ceramic faced laminate armours after the impact of a high velocity bullet. Wilkins (17) attributed the formation to a form of Hertzian cone cracking. However a possible alternative explanation is proposed here.

The equations presented by Miller and Pursey (9) which describe the behaviour of waves within a semi-infinite solid body have been considered in connection with the development of the fracture cone in the ceramic facing of a ceramic composite armour. These equations are shown below.

$$U_r = \frac{-a^2 P_0 e^{i(wt-c_1 R)}}{2GR}\Theta_1(\theta) \tag{9.1}$$

$$U_\theta = \frac{-ia^2\mu^3 P_0 e^{i(wt-c_2 R)}}{2GR}\Theta_2(\theta) \tag{9.2}$$

$$\Theta_1(\theta) = \frac{(\cos\theta)(\mu^2 - 2\sin^2\theta)}{F_0(\sin\theta)} \tag{9.3}$$

$$\Theta_2(\theta) = \frac{(\sin 2\theta)\sqrt{\mu^2\sin^2\theta - 1}}{F_0(\mu\sin\theta)} \tag{9.4}$$

$$F_0(\zeta) = (2\zeta^2 - \mu^2)^2 - 4\zeta^2\sqrt{\zeta^2 - \mu^2}\sqrt{\zeta^2 - 1} \tag{9.5}$$

where $\zeta = \sin\theta$ or $\mu\sin\theta$

$$\mu = \sqrt{\frac{2(1-\nu)}{2\nu}} \tag{9.6}$$

where

ν	=	Poisson's Ratio
θ	=	Angle from central axis
U_r	=	Displacement in the radial direction
U_θ	=	Displacement in the transverse direction
a	=	Radius of disk vibrating normally to the surface of the plate
P_0	=	Stress beneath the disk
R	=	Radius from the vibrating disk
c_1	=	Dilatational wave velocity
c_2	=	Shear wave velocity
G	=	Shear Modulus

These equations are presented graphically in figs 52 and 53. Fig 52 shows how the amplitude of the compression wave (U_r) varies with the angle from the axis (θ), and figure 53 shows how the amplitude of the shear wave (U_θ) varies with the angle from the axis (θ). In order to plot these two equations an arbitrarily chosen constant value was used to represent "mechanical" part of the equations, namely

$$\frac{a^2 P_0}{2GR} \quad \text{and} \quad \frac{ia^2\mu^3 P_0}{2GR} \tag{9.7}$$

Thus the figures show the dependence of the displacement on the angular variation. Woods (10) who discussed this work in the context of seismic waves defined a "shear window" as a zone extending either side of the point where the shearing changes direction. Within this zone the material experienced a high shear displacement. It is proposed that this is the cause of the cone shaped fracture which occurs in the ceramic facing of a ceramic composite armour soon after impact.

This relationship is demonstrated by the experimentally measured angle subtended by the material ejected from the back of the tile, as discussed in section 4.2.3, which are presented in Table 17. They were drawn as a histogram on the existing diagram of the displacement against angle, figure 52. This format was chosen because the curve represented the change in displacement amplitude with angular variation. A large displacement means that there is a large strain developed between the displaced and un-displaced material. Where the strain is high, the probability of a defect nucleating and propagating a crack is also high. So the curve can also be considered as the variation of the probability of developing a crack with angle. The displacement scale was chosen arbitrarily. The histogram follows the shape of the curve quite closely, with most of the angles of the fracture cones clustering around the zones of greatest displacement. The two peaks of the histogram do not coincide exactly with the two peaks of the predicted curve. The predicted curve was constructed using a Poisson's ratio of 0.24, it is possible that the passage of the compression wave preceding the shear wave had produced a number of microcracks. According to Case (3) this would reduce the moduli and Poisson's ratio. This would have the effect of increasing the angle of the cross over, which would fit the results even better. The change in sense of the histogram was done simply to make interpretation easier. The important factor is the amplitude of the displacement, rather than its direction. A fracture will occur at a given angle only if the fracture path at this angle contains a large enough flaw, and the displacement is large enough to activate it. This would account for the multiplicity of fracture cones found by Wilkins (17) in partially penetrated ceramics.

The possibility that the cone angle was influenced directly by the compression wave was examined by superimposing the histogram of angle distribution on to the curve representing the amplitude and shape of the wave front for the compression wave, figure 53. The amplitude is greatest on the axis, but no fracture cones were found near this point. The amplitude of the compression wave tails away as the angle increases, but the number of cones recorded at higher angles do not.

There is a tendency for the measured angle to increase as the depth of penetration increases, as shown in figure 54, the graph of angle against penetration. It must be remembered that the cone angle measured is the outer cone angle, there may, in fact almost certainly will be, cones formed previously within that measured angle which can not be detected. The cone angle is measured from the outer edge of the squashed head, which will initiate new fracture cones as it advances. This process is detailed in figure 55. It is possible that the angle increases with the penetration because the pressure built up within the ceramic during penetration causes the cone to expand sideways. Another possibility is that other factors cause the ceramic around the cone

to fail, and this may confuse the detail on the radiogram.

There appears to be some degree of correlation between the measured cone angle and the apex angle measured for the sideways distortion of the bullet tip for the alumina faced armours. The angle for the alumina aramid armour was found to be 46 and the angle for the alumina GRP armours 50° . The angle around which many of the fracture cones wee found is 47° . This suggests that the fracture cone forms a boundary between the broken and unbroken ceramic which restrains the expanding bullet tip. However, the apex angle formed by the spreading tip of the bullet as it penetrated the glass faced armour was 26° . This is about half the angle of the cross over predicted Miller and Pursey's formula for glass, 52° . This does not necessarily disprove the theory, because glass is a much weaker material, and so the forces causing the bullet to expand are smaller. It may that the fracture cone restrains the expanding tip if the force resisting its progress is great enough to cause it to expand that far.

9.2 Axial Cracking

Wilkins (17) observed that soon after projectile impact a crack developed directly opposite on the rear face of the ceramic tile. This was attributed to plate bending, which occurred after the backing had yielded and the support to the ceramic was reduced. This suggestion was suspected because in section 8 it was shown that plate bending was unlikely in these circumstances, and so an alternative explanation is presented here.

The acoustic mismatch between the ceramic and backing was of an order where reflection of the wave incident on the rear face of the ceramic was a more likely event. The case of waves reflected from an inclined plane was studied by Kolsky (12). When a dilatational wave is incident on an inclined surface it is reflected as both dilatational and shear waves, the amplitudes are dependant on the angle of incidence, as shown in figure 56. Similarly with a shear wave incident on an inclined surface, both dilatational and shear waves are produced.

Thus when a spherical dilatational wave, as described by Miller and Pursey (9), is incident on the rear face of a ceramic tile, its intersection with the rear surface of

the plate is at a constantly changing angle of incidence. The shape of the reflection of a spherical dilatational wave with a varying amplitude, of the type shown in figure 53, is presented in figure 57. The abscissa is the distance from the axis, the solid line represents the shape of the reflected dilatational wave and the broken line represents the shear wave produced by the same incident spherical dilatational wave.

It can be seen in figure 57 reveals that the amplitude of the reflected dilatational wave reaches a peak which is concentrated in a narrow zone directly opposite the source of the disturbance. Since the incident wave is a compression wave, then the reflection is a tensile wave. Alumina is much weaker in tension than compression, so much more likely to fail in this region as a result of this reflected wave. This is the most likely explanation for the axial crack found on the back face of the ceramic armours described by Wilkins (17). Superimposed on this effect is the natural attenuation of the wave amplitude caused by spherical expansion, thus limiting further the zone where any substantial tension damage could occur on the back face of the tile. The peak for the shear component occurs at a greater distance from the point of impact, around 3mm either side.

9.3 Radial Cracking

Radial cracking of the armour facing has been reported by several workers (12,14). The number of radial cracks in the facing varies from material to material, but seems to remains fairly constant for each facing material. It is proposed that the number of cracks observed is a function of the elastic wave speed of the material.

The material surrounding the site of an impact which experiences the compression wave is moved outward from the point of impact. In doing so a tensile hoop stress is induced in the material which is displaced. As the level of the stress increases several cracks will be initiated and begin to propagate. Once a crack has begun to propagate then a relief wave radiates out in the direction of the original hoop stress. This relief wave inhibits the nucleation or propagation of other cracks in the region it travels through. Therefore there are three competing factors involved in producing the radial cracks. The rate of increase of the hoop stress, the velocity of the relief wave produced by the propagation of a crack, and the size and distribution of defects in the material. The rate of increase of the hoop stress is governed ultimately by the

stress pulse produced by the impacting projectile. If this is much greater than the relief wave velocity, then many radial cracks will be produced. If the converse is true few cracks will be produced, because once one crack is propagating it brings relief to large sectors of the ceramic, preventing further cracks propagating.

It is therefore concluded that the cone crack is the product of the shear wave caused by the impact of the projectile on the ceramic. The axial crack is produced by the reflection of the dilatational wave from the rear face. Radial cracking is dependant on three factors, the rate of increase of the dilatational wave, the velocity of the relief waves, and the defect structure of the material.

Chapter 10

Construction of the Model

This section presents the sequence of events during the penetration of a ceramic composite armour. Followed by a more detailed study of the specific features involved, leading to a method for modelling each one. Finally all the individual models are combined into a single model which can predict the Critical Velocity (V_c) of a range of facing materials on aramid laminate backings. The limits of the model, both in terms of its performance and the materials it can be applied to are then discussed.

10.1 Sequence of Events

It is now possible to extend description of the sequence of events developed by Wilkins (17). Pressure is developed at the tip of bullet, and when this exceeds its yield strength the bullet begins to deform. This deformation consists of spreading the bullet material side ways, and continues during the penetration of the armour facing. The degree of sideways spreading appears to be influenced by the strength of the ceramic facing.

The time after impact at which fracturing of the ceramic begins is also apparently dependant on the strength of the ceramic facing. A fracture cone is known to develop, and is important at this stage to spread the load of the impact over as great an area

of backing as possible, to prevent premature backing failure. The fracture cone may also act as a restraint on the spreading of the bullet as it penetrates the ceramic.

The interface between the distorted bullet and the crushed ceramic progresses through the thickness of the tile at a constant velocity, which again appears dependant on the strength of the ceramic facing. As the bullet penetrates the ceramic it continues to be eroded, losing its length and energy as a consequence. The velocity of the rear of the bullet remains that of the impact velocity throughout the entire penetration of the ceramic facing.

The distortion of the bullet is one of the energy absorption mechanisms. Another absorption mechanism is that of the backing, which dominates when the tile has been fully penetrated. The energy absorbed by the backing is governed by the number of layers of aramid textile in its construction and the presented area of the projectile.

10.2 Individual Methods of Models Penetration Features

10.2.1 Modelling Bullet Erosion

In section 5.2 the relationship between the bullet eroded and the strength of the material was established and was given in equation (5.1). This included a value for the velocity of penetration through the facing of the interface between the bullet and crushed ceramic (u). In order to use this equation, it is necessary to re arrange it, collecting all the u^2 terms together. This is shown below.

$$(R + \frac{1}{2}\rho_p v^2) - \rho_p uv + u^2 \frac{\rho_p - \rho_t}{2} = 0 \qquad (10.1)$$

This is a quadratic in u. The roots of this equation, two values for u, one of which is the penetration velocity through the ceramic. The correct root was found

by comparison with the measured values. It was established in Section 5.2 equation (5.1) that there was a relationship between this velocity, the impact velocity and the rate of erosion. Thus the rate of erosion was calculated, and with the thickness of the facing the length of the bullet eroded can easily be calculated also.

10.2.2 Modelling the Bullet Volume

The volume of the bullet which is eroded has to be found in order to calculate the energy remaining in the projectile after it has penetrated the ceramic. This energy remaining is the energy which has to be absorbed by the laminate backing. The shape of the bullet used in this work is shown in figure 19. The shape of the ogive was fitted to a polynomial as described in section 4.6 equation (4.3). In order to calculate the volume of the bullet this equation was integrated term by term. The final equation giving the volume of the bullet eroded, V is

$$V = \pi(0.4249L + 0.24436L^2 + 0.09257L^3 - 0.008565L^4) \qquad (10.2)$$

where L = Length of bullet eroded
V = Volume of bullet eroded

Equation (10.2) is presented in a truncated format for the sake of brevity in the text. The full form appears in Annex A.

The mass of the bullet eroded can now be calculated from the volume eroded. The energy expended during erosion is the difference between the kinetic energy of the bullet before impact and the kinetic energy after penetration of the ceramic.

10.2.3 Modelling Bullet Tip Distortion

The spreading of the tip of bullet is important because this is one of the factors governing the energy absorbed by the laminate backing. In order to model the spreading

of the bullet tip, the empirical relationship between the final radius and the energy lost during penetration of the ceramic, derived in section 5.3, was developed. This relationship is shown below.

$$\pi R^2 = Ek \tag{10.3}$$

where R = Tip radius
E = Energy lost during penetration
k = a constant

This relationship was established for bullets impacting the target at 1000 m/s. There is a strong possibility that the impact velocity influences the behaviour of the projectile during penetration. The velocity may influence the temperature of the tip and the ease with which it can deform. In order to make the expression applicable to different velocity it was decided to incorporate the velocity into the expression by making the assumption that

$$k = QV_i \tag{10.4}$$

, where Q is a constant of proportionality. Substituting this into the above gives:

$$\pi R^2 = EQV_i \tag{10.5}$$

This is the expression used in the model to calculate the radius of the distorted tip of the projectile after it has penetrated the ceramic facing. The value for Q was found empirically to be 0.000136 mms/J. The value for the energy lost during pentration is calculated in the program from

$$E = HL \tag{10.6}$$

where L = length of projectile destroyed
H = a constant of proportionality

The value for H was found empirically to be 72.3 J/mm. Combining equations (10.5) and (10.6) gives

$$\pi R^2 = QV_iHL \tag{10.7}$$

10.3 Model Construction

It is now possible to combine the expressions discussed previously into a single unified model predicting the ballistic performance of ceramic composite armours. The flow diagram for this is shown in figure 58. A computer program to calculate the Critical Velocity of an armour combination given the material properties of the ceramic facing, and assuming the backing is the standard aromatic polyamide laminate is presented in Annex A. The first form of the model was used to predict the Critical velocity for a given armour combination. Calculation was always begun by assuming an impact velocity of 1000m/s, which was either increased or decreased depending on the whether the could absorb more energy than that of the projectile which had penetrated the ceramic, or the energy of the penetrating projectile exceeded the capability of the backing. The programme continued until it was calculated that the armour could just absorb the energy of the impacting projectile, as this was declared to be the V_c.

10.4 Agreement Between Actual and Predicted Critical Velocities

In order to assess the accuracy of the model proposed above, several armour combinations, for which the critical velocities had previously been measured, were evaluated using the program. The results are shown in table 31. The model was validated with armours constructed from 97.5% alumina facing, with an aramid backing. This material is used frequently in armour construction.

The program was also applied to several other facing materials. Of these two appeared to have close agreement between their measured ballistic performance and that predicted quite well, as is also shown in table 31. The model was not applicable to all materials, and there was no clear feature which indicated those materials to which it was applicable. The measured Critical Velocities and the mechanical properties for these materials were taken from published results. Good agreement is defined as a % variation of 5% or less. Further work is needed to produce a relationship between the spreading of the projectile tip and the factors which influence it. Further work is

also needed to identify the reason why the model seems to predict the performance of some materials quite well, and other only poorly.

10.5 Limits of Model Applicability

If the areal density of 97.5% alumina is progressively reduced then the Critical Velocity predicted approaches a single value of about 719m/s. This is far higher than the 450m/s which was measured for this armour. A graph of the variation of ballistic performance, both measured and predicted, is presented in figure 59. The lower areal densities of the series would be unlikely candidates for armour applications, and so could be argued would fall outside the range normally required of any predictive model. However this limitation should be examined and explained.

The value for the constant "C" derived in Section 7.2 was found to change between 3mm and 4mm thick facings. In section 8.3 fig 51, it was demonstrated that there was a change in the behaviour of alumina faced armours with changing areal density. There is evidence that this was due to the generation of bending waves in the thinner facings. A mechanism of armour failure including bending was not considered in this model. Whether bending was or was not the cause of the transition, this may be the reason why the performance of some facing materials was not predicted accurately by the model. Certainly the model predicted the performance of the 4mm thick facing well, but was at some variance with the results for thinner armours.

Other factors which may assume greater importance in determining the mechanism as the velocity of impact decreases are that the strength of the lead projectile was assumed zero in all of the calculations. This will be approximately true at the higher impact velocities when it is known that the lead is molten. However, at the lower impact velocities associated with lower areal densities this may not be true, and so should form a term in expression (5.1). The other reason is that the expression derived for the spreading of the bullet is empirical, and so cannot be expected to be valid for conditions significantly different from those used in the initial derivation. The factor most likely to cause the departure from the predicted behaviour is the viscosity of the lead. This is known to be temperature dependant, and the temperature generated during the impact will be related to the impact velocity. It does not appear explicitly in expression (5.1), but is "included" in the constant term. It is

unreasonable to assume that it is constant and so further work is needed to clarify the effect of the projectile viscosity on the spreading of its tip.

Table 31 also contains results for armours faced with other materials, but still with an aramid laminate backing. These are the best of several materials which were attempted. The performance predicted was compared to the actual measured values for the V_c. There was insufficient data available to be able make a definite suggestions as to why some materials were similar in there performance to the model, and others markedly different. It is possible that the failure mechanism was not the same in all cases. The difference found between the 3mm and 4mm thick alumina facings, may apply to many materials, but at different thicknesses, putting those which are below the threshold in a regime not addressed by this model.

Thus the model is reasonably reliable for alumina, boron carbide, and silicon carbide faced armours, provided that the areal density of the armour is sufficient to have a Critical Velocity around 1000m/s. Thus it can be used as a design tool when an armour is required to defeat a 5.56mm bullet at between 850m/s and muzzle velocity, which the most common situation. The criterion which determines those materials that it does apply to and those it does not has not fully been established. However it has been found that the appearance of bending waves in the facing material is a candidate for this criterion.

Chapter 11

Conclusions

1. A model has been developed which can predict the ballistic performance of Alumina faced aramid backed laminate armours. It can be used as a design tool to calculate the areal densities of armours of this type required to defeat 5.56mm bullets with impact velocities in the range 850m/s to 1000m/s.

2. The model developed can be applied to other ceramic facing materials also. It has been found that it cannot be applied to all ceramic materials, and at present there is no indication which materials amenable to the application of the model an those which are not.

3. It has been established that there is a change in the ballistic behaviour of alumina faced armours which occurs when the facing is between 3mm and 3.5mm thick. There is evidence that this change is from a failure mechanism dominated by bending to one which is not.

4. It is proposed that the model cannot be applied to a wide range of materials because they may not exceed the transition thickness for that material in the armour analysed.

5. It has been established that the armour can be analysed by separating the behaviour of the facing and that of the laminate backing and analysing each individually

6. It has been established that the modified Bernoulli equation, developed for the penetration of metallic armours, can be applied to the ceramic facing.

7. The fracture cone known to develop has been found to be dependant upon the shear wave produced by the impact of the projectile on the armour.

8. The axial crack observed to develop on the rear face of the ceramic has been attributed to the reflection of the dilatational wave from that face.

9. A model has been developed which can predict the ballistic performance of aramid laminates.

10. An empirical relationship between the angle of incidence of the bullet and the performance has been developed for alumina faced aramid backed laminate armours.

11. It was found that the rigidity of the backing did influence the performance of the ceramic facing. This was not by preventing the ceramic bending, but by confining the crushed ceramic so that it could support a load during the penetration of the projectile.

Chapter 12

Further Work

The model developed has limitations. These have been attributed to the change in the behaviour of the armours which occurs as the facing thickness changes. The candidate mechanism for failures below the transition thickness is bending. Further work is needed in order to clarify whether bending is involved and to what extent. The factors controlling the transition also have to be definitely established.

Another of the limitations found with the model as it has been presented here is that is fails to accurately predict the behaviour of amours at low areal densities. This is partly attributable to the transition in the armour behaviour, but may also be due to a change in the factors controlling the behaviour of the bullet. More work is required on the dependence of the behaviour of the bullet on the impact velocity.

It was also found the model could be applied to some facing materials but not all. More work is needed on the reasons behind this. The model for predicting the performance of the laminates was limited. Work is needed to extend this model to other fibres and constructions. In addition, the term for the specific energy to failure has not been related to any material properties. If the model is to be universally applicable then this must be done.

Chapter 13

References

1. Men at Arms Series No. 157 Osprey
2. Churchill W S. History of the English Speaking People.
3. Case E D. The Effect of Microcracking upon the Poisson's Ratio for Brittle Materials. J Mat Sci 19 (1984) 3702-3712
4. Lankford J. The Role of Subcritical Tensile Microfracture Processes in Compression Failure of Ceramics. IN Bradt R C, ed. Fracture Mechanics of Ceramics Vol 5, pp 625 - 637.
5. Liaw B M, Kobayashi A S, Emery A F. Theoretical Model of Impact Damage in Structural Ceramics. J American Ceramic Soc. Vol 67, No8. pp 544 - 548
6. Kumar A. The Effect of Stress Rate and Temperature on the Strength of Basalt and Granite. Geophysics Vol 33, No3 1968. pp 501 - 510
7. Graff K F. Wave Motion in Elastic Solids. Clarendon Press Oxford. pp 5 - 7
8. Lamb H. On the Propagation of Tremors Over the Surface of an Elastic Solid. Philosophical Transactions Royal Soc A 1904 p203 pp 1 - 42
9. Miller G F, Pursey H. The field and radiation impedance of mechanical radiators on the free surface of a semi-infinite isotropic solid. Proc R Soc A223 pp 521 - 541

10. Woods R D J. Screening of Surface Waves in Soils. Soil Mech Founds Div Am Soc Civ Eng 94, 951-79

11. Kolsky H, Shearman A C. Investigation of fractures produced by transient stress waves. Research 1949, 2 pp 384 - 389

12. Kolsky H, Christie D G. The fracture produced in glass and plastics by the passage of a stress pulse. Trans Soc Glass Tech 1952, Vol 36T, pp 65 - 73

13. Christie D G. An investigation of cracks and stress waves in glass and plastics by high speed photography. Trans Soc Glass Tech 1952, Vol 36T, pp 74 - 89

14. Kolsky H, Shi Y Y. Fractures produced by stress pulses in glass like solids. Proc Phys Soc 1958, 72, 447

15. Tsai Y M, Kolsky H. The study of the fractures produced in glass blocks by impact. J Mech Phys Solids, 1967, Vol 15. pp 263 - 278

16. Evans W M, Taylor G I. Deformation and fractures produced by intense stress pulses in steel. Research 1952, 5 pp 502 - 509

17. Wilkins M L, Cline C F, Honodel C A. Fourth progress report of light armour programme. URCL 50694 Lawrence Livermore University of California

18. Rosenberg Z, Yeshurun Y. The Relation Between Ballistic Efficiency and Compressive Strength of Ceramic Tiles. Int J Imp Eng. Vol 7 (3). 357-362

19. Prior A M, Hetherington J G. The Penetration of Composite Armour by Small Arms Ammunition. 9th Int Conf on Ballistics. RMCS Shrivenham.

20. Prosser R A. Penetration of Nylon Ballistic Panels by Fragment Simulating Projectiles. Part I. Textile Research Journal Feb 88. pp 61 - 85

21. Frechette V D, Cline C F. Fractography of ballistically tested ceramics. Bulletin of the American Ceramic Soc Vol 47, 1970 pp 994 - 997

22. Hohler V, Stilp A J. Hypervelocity impact of rod projectiles with L/D from 1 to 32. Int J Impact Engng Vol 5 1987 pp 323-331

23. Dehn J J. A unified theory of penetration. Int J Impact Engng Vol 5 1987 pp 239-248

24. Goldar D, Paldas M. Dynamic Response of Transversely Impacted Beams of Different Materials. Fifth Int Cong on Exp Mech, 10 - 15 June 84. Soc Exp Mech pp 584 - 589

25. Tate A. An Estimate of Temperature Effects During Rod Penetration. 9th Int Conf on Ballistics RMCS Shrivenham.

26. Janach W. Impact of a steel cylinder on a rock half space. Inst Phys Conf Ser 47, 1979 pp 331 - 336

27. Hornemann U, Rothenhäusler H, Senf H. Experimental investigation of wave and fracture propagation in glass slabs loaded by steel cylinders at high impact velocities. 3rd Conf Mech Prop High Rates of Strain Oxford 84, Inst Phys Conf Ser No70. pp 291 - 298

28. Recht R F, Ipson T W. Ballistic Penetration Resistance and its Measurement. Denver Research Institute for Weapons Development NWC TP 5648.

29. Wilson L L. Experimental Rod Impact Results. Int J Impact Eng.Vol 8 (1) 15-25.

30. Medick M A. On Classical Plate Theory and Wave Propagation. J Appl Mech 28, 223-8 (1961)

31. Press F, Oliver J. Model Study of air Coupled Surface Waves. J Acoust Soc Am 27, 43-6 (1955)

32. Dohrenwend C O, Drucker D C, Moore P. Transverse Impact Transients. Exp Stress Analysis 1 1-10 (1944)

Chapter 14

Annex A

```
1   REM          Program to predict the ballistic performance
                        of ceramic armours
2   REM                 against 5.56mm ball rounds.

5   REM input section
10  DP=11700!:PI=3.141592654#
20  INPUT "Target Density";DT
30  INPUT "Target Thickness (mm)";T
40  INPUT "Backing Areal Density";AD
50  INPUT "Ceramic Compressive Strength";RT
70  VI=1000
79  REM ====================Calculation 1
                             penetration velocity
80  A1=.5*DP-.5*DT
90  B1=-DP*VI
100 C1= .5*DP*VI*VI-RT
110 PVEL=(-B1-SQR(B1*B1-4*A1*C1))/2/A1
120 LDEST=(VI-PVEL)*T/PVEL
129 REM ====================Calculation 2
                             volume eroded
130 A2=.4249:B2=.5751:C2=-.06237:D2=.003788:E2=-.0000966
140 X=LDEST
```

```
150 VOL=PI*((A2*X)+(A2*B2*X*X)+((2*A2*C2+B2*B2)*X^3/3)
          +((A2*D2+B2*C2)*2*X^4/4)+((2*(A2*E2+B2*D2)+C2*C2)*X^5/5)
          +((B2*E2+C2*D2)*2*X^6/6)+((2*C2*E2+D2*D2)*X^7/7)
          +(2*D2*E2*X^8/8)+(E2*E2*X^9/9))
159 REM ==================Calculation 3
                          mass distorted and mass
                          remaining undistorted.
160 MDIST=DP*VOL/1000000!
170 MASS=3.5-MDIST
179 REM ==================Calculation 4
                          energy remaining and energy
                          in distorted portion
180 EREM=MASS*VI*VI/2000
190 EDIST=MDIST*PVEL*PVEL/2000
199 REM ==================Calculation 5
                          radius of the distorted tip
200 A5=.000136*VI*72.3*LDEST:
    R=SQR(A5/PI)
209 REM ==================Calculation 6
                          energy absorbed by the backing
210 EBACK=.336*PI*R*R*AD/.28
219 REM ==================Calculation 7
                          Calculating whether the
                          projectile would penetrate.
220 ETOTAL=EDIST+EREM
230 E=ETOTAL-EBACK
231 PRINT "E= ";E:
    PRINT "EREM= ";EREM:
    PRINT "ETOTAL=  ";ETOTAL:
    PRINT "EDIST=  ";EDIST:
    PRINT "EBACK=  ";EBACK
232 PRINT "R=  ";R:
    PRINT "LDEST=  ";LDEST:
    PRINT "PVEL=  ";PVEL
233 PRINT "VI=  ";VI
234 PRINT "VOL=  ";VOL:
    PRINT
240 IF E>0 THEN VI=VI-5:GOTO 80
250 IF E<-20 THEN VI=VI+1:GOTO 80
259 REM ==================printing section
```

```
260 PRINT:PRINT:PRINT CHR$(7)
270 PRINT "Tile thickness  ";T
280 PRINT "Backing AD  ";AD
290 PRINT "Total AD  ";T*DT/1000+AD
300 PRINT "The Critical Velocity for this Armour is  ";VI
310 PRINT "Bottom Limit (5%) is  ";VI*.95
320 PRINT "Top Limit (5%) is  ";1.05*VI
330 END
```

14.1 Notation Used in the Computer Program

DP	=	Projectile Density (kg/m^3)
DT	=	Target Density (kg/m^3)
T	=	Target thickness (mm)
AD	=	Backing Areal Density (kg/m^3)
RT	=	Ceraimc Compressive Strength (N/m^2)
VI	=	Impact Velocity (m/s)
A1	=	Calculation of the coefficient a in the formula $(-b \pm \sqrt{b^2 - 4ac})/2a$
B1	=	Calculation of b in the above formula
C1	=	Calculation of c in the above formula
PVEL	=	Velocity of penetreatraion through the ceramic facing (m/s)
LDEST	=	Length of projectile distorted (mm)
VOL	=	Volume of projectile distorted (mm^3)
MDIST	=	Mass of projectile distorted (g)
MASS	=	Mass of projectile remaining undistorted (g)
EREM	=	Energy remaining in the undistorted part of the projectile (J)
EDIST	=	Energy in the distorted part of the projectile (J)
A5	=	Area of distorted projectile tip (mm^2)
R	=	Radius of distorted projectile tip (mm)
EBACK	=	Energy which can be absorbed by backing (J)
ETOTAL	=	Total energy of the projectile after penetrating the ceramic (J)
A2	=	Coefficient in equation (10.2)
B2	=	Coefficient in equation (10.2)
C2	=	Coefficient in equation (10.2)
D2	=	Coefficient in equation (10.2)
E2	=	Coefficient in equation (10.2)

			Virgin			After Fracture		
Materials	$-\sigma_1^*$	*Behaviour*	$-\sigma_3^+$	$\frac{\sigma_1-\sigma_3}{2}$	P^c	$-\sigma_3$	$\frac{\sigma_1-\sigma_2}{2}$	P
BeO	0	Brittle	13.6	6.8	4.5	0	0	0
	1.0	Brittle	29.7	14.4	10.6	6.2	2.6	2.7
	2.0	Brittle	31.6	14.8	11.9	13.8	5.9	5.9
	2.0	Brittle	31.3	14.7	11.8	20.0	9.0	8.0
	3.5	Ductile	36.3	16.4	14.4	-	-	-
	7.5	Ductile	40.4	16.5	18.5	-	-	-
	10.0	Ductile	44.2	17.1	21.4	-	-	-
Al_2O_3	0	Brittle	13.3	6.7	4.4	0	0	0
	1.0	Brittle	53.3	26.2	18.4	14.2	6.6	5.4
	1.0	Brittle	43.9	21.5	15.3	11.0	5.0	4.3
	2.0	Brittle	52.7	25.4	18.9	19.4	8.7	7.8
	2.0	Brittle	46.2	22.6	16.7	17.6	7.8	7.2
	2.0	Brittle	60.8	29.4	21.6	13.4	5.7	5.8
	3.5	Brittle	55.1	25.8	20.7	32.9	14.7	13.3
	5.6	Brittle	58.3	26.4	23.1	36.0	15.2	15.7
	8.3	Brittle	71.4	31.6	29.3	43.7	17.7	20.1
	8.3	Brittle	69.7	30.7	28.7	49.5	20.6	22.0
	9.2	Brittle	62.2	26.5	26.8	33.4	12.1	17.2
	11.0	Brittle	72.6	30.8	31.5	49.8	19.4	23.9
	12.5	Brittle	71.5	29.5	32.2	36.7	12.2	20.6

TABLE 1
Summary of Pressured Measured in Triaxial Compression tests (After Wilkins)

Materials	$-\sigma_1^*$	*Behaviour*	$-\sigma_3^+$	$\frac{\sigma_1-\sigma_3}{2}$	P^c	$-\sigma_3$	$\frac{\sigma_1-\sigma_2}{2}$	P
B_4C	0	Brittle	13.0	6.5	4.3	0	0	0
	1.0	Brittle	54.2	26.6	18.7	7.3	3.1	3.1
	2.0	Brittle	62.6	30.3	22.2	20.1	9.1	8.0
	4.2	Brittle	67.3	31.6	25.2	27.4	11.6	11.9
	7.2	Brittle	81.7	37.3	32.0	35.6	14.2	16.7
	9.0	Brittle	70.2	30.6	29.3	39.0	15.0	19.0
	15.8	Brittle	91.8	38.0	41.1	54.2	19.2	28.6

Sign Conventions: Tensiile Stress taken as Positive
All Pressures in Kbar

* $\sigma_1=\sigma_2$=*confining stress*

\+ σ_3=*load stress*

c $P = -\left(\frac{\sigma_1+\sigma_2+\sigma_3}{3}\right)$

TABLE 1 (continued)
Summary of Pressures Measured in Triaxial Compression tests (After Wilkins)

Density	= 3.24 x 10^3	kgm^{-3}
Youngs Modulus	= 152 x 10^9	Nm^{-2}
Compressive Strength	= 2.1 x 10^9	Nm^{-2}

Properties of AD - 85 Alumina

TABLE 2

Density	= 3.79 x 10^3	kgm^{-3}
Youngs Modulus	= 338 x 10^9	Nm^{-2}
Compressive Strength	= 2.4 x 10^9	Nm^{-2}

Properties of 975 Alumina

TABLE 3

Density	= 2.47 x 10^3	kgm^{-3}
Youngs Modulus	= 152 x 10^9	Nm^{-2}
Compressive Strength	= 0.7 x 10^9	Nm^{-2}

Properties of glass

TABLE 4

	AVERAGE TIME µs	MEASURED TILE THICKNESS (mm)	MEASURED PROJECTILE LENGTH (mm)	ADJUSTED PROJECTILE LENGTH (mm)	AVERAGE ADJUSTED PROJECTILE LENGTH (mm)	FITTED PROJECTILE LENGTH (mm)	PERCENTAGE VARIATION (%)
B75	2.00	8.50	20.50	16.76	17.31	16.2267	6.27
B79		8.50	20.50	16.76			
B76		8.00	20.50	16.83			
B77		8.00	22.50	18.90			
B80	4.00	8.00	19.00	15.32	14.52	14.9067	-2.69
B74		8.00	18.50	14.83			
B83		8.00	18.00	14.35			
B88	6.00	7.50	17.00	13.56	13.33	13.5867	-1.93
B85		7.50	17.00	13.56			
B86		7.50	16.00	12.64			
B87		7.50	17.00	13.56			
B84		8.00	17.00	13.39			
B93	8.00	8.00	15.50	11.98	11.94	12.2667	-2.70
B91		7.75	16.00	12.54			
B92		7.50	15.50	12.18			
B90		8.00	14.50	11.07			
B89		7.50	14.50	11.29			
B98	10.00	7.75	14.00	10.73	10.00	10.9467	-9.45
C01		7.50	13.00	9.97			
B96		8.00	14.00	10.62			
B99		7.50	11.50	8.69			

TABLE 5
Alumina Faced Armour with GRP Backing
Measured, Adjusted and Fitted Data for Projectile Erosion

	AVERAGE TIME ms	MEASURED TILE THICKNESS (mm)	MEASURED PROJECTILE LENGTH (mm)	ADJUSTED PROJECTILE LENGTH (mm)	AVERAGE ADJUSTED PROJECTILE LENGTH (mm)	FITTED PROJECTILE LENGTH (mm)	PERCENTAGE VARIATION (%)
C04	12.00	8.00	12.50	9.31	9.41	9.6267	-2.30
C05		7.75	11.50	8.56			
C02		7.50	12.00	9.11			
C03		7.00	13.50	10.66			
C09	14.00	8.00	13.50	10.18	8.90	8.3067	6.63
C11		7.50	11.00	8.27			
C08		7.50	12.00	9.11			
C07		8.00	11.00	8.03			
C09		7.50	13.00	9.97			
C10		8.00	12.50	9.31			
C12	16.00	8.00	10.00	7.21	7.44	6.9867	6.09

Gradient of Fitted Length v Time	-0.66
Intercept of Fitted Length v time	17.55
Correlation coeffiecient	0.97

TABLE 5 (continued)
Alumina Faced Armour with GRP Backing
Measured, Adjusted and Fitted Data for Projectile Erosion

	AVERAGE TIME µs	MEASURED TILE THICKNESS (mm)	MEASURED PROJECTILE lENGTH (mm)	ADJUSTED PROJECTILE LENGTH (mm)	AVERAGE ADJUSTED PROJECTILE LENGTH (mm)	FITTED ADJUSTED PROJECTILE LENGTH (mm)	PERCENTAGE VARIATION (%)
B16	2.00	7.87	22.50	18.29	17.99	18.2820	-1.61
B17		7.87	22.00	16.75			
B21		7.87	23.50	18.09			
B19		7.87	24.00	18.54			
B22		7.87	23.00	17.64			
B20		7.87	24.50	19.00			
B18		7.87	23.00	17.64			
B27	4.00	7.87	20.50	16.34	17.23	16.8340	2.32
B23		7.87	20.50	16.34			
B25		7.87	20.50	16.34			
B26		7.87	25.00	20.81			
B28		7.87	20.50	16.34			
B34	6.00	7.87	20.00	15.86	15.11	15.3860	-1.83
B32		7.87	19.50	15.39			
B31		7.87	18.50	14.45			
B30		7.87	19.50	15.39			
B33		7.87	18.50	14.45			

TABLE 6
Alumina Faced Armour with Aromatic Polyamide Laminate Backing
Measured, Adjusted, and Fitted Data for Projectile Erosion

	AVERAGE TIME µs	MEASURED TILE THICKNESS (mm)	MEASURED PROJECTILE lENGTH (mm)	ADJUSTED PROJECTILE LENGTH (mm)	AVERAGE ADJUSTED PROJECTILE LENGTH (mm)	FITTED ADJUSTED PROJECTILE LENGTH (mm)	PERCENTAGE VARIATION (%)
B39	8.00	7.87	18.00	13.99	14.32	13.9380	2.66
B37		7.87	18.50	14.45			
B35		7.87	20.50	16.34			
B36		7.87	16.50	12.63			
B38		7.87	18.20	14.18			
B41	10.00	7.87	15.50	11.74	12.46	12.4900	-0.26
B42		7.87	16.00	12.18			
B46		7.87	16.00	12.18			
B47		7.87	16.00	12.18			
B43		7.87	18.00	13.99			
B52	12.00	7.87	15.00	11.30	10.87	11.0420	-1.54
B51		7.87	13.50	10.01			
B49		7.87	15.00	11.30			
B50		7.87	15.00	11.30			

Gradient of Fitted Length v Time	-0.72
Intercept of Fitted Length v Time	19.73
Correlation coefficient	0.99

TABLE 6 (continued)
Alumina Faced Armour with Aromatic Polyamide Laminate Backing
Measured, Adjusted, and Fitted Data for Projectile Erosion

	AVERAGE TIME µs	MEASURED TILE THICKNESS (mm)	MEASURED PROJECTILE LENGTH (mm)	ADJUSTED PROJECTILE LENGTH (mm)	AVERAGE ADJUSTED PROJECTILE LENGTH (mm)	FITTED ADJUSTED PROJECTILE LENGTH (mm)	PERCENTAGE VARIATION (%)
C27	4.00	7.500	18.50	15.408	16.80	16.634	0.987
C28		7.500	20.00	16.711			
C30		7.500	21.00	17.584			
C29		7.500	20.00	16.711			
C26		7.500	21.00	17.584			
C35	6.00	7.500	19.50	16.276	15.61	15.766	-1.011
C33		7.000	18.50	15.596			
C32		7.000	18.00	15.182			
C34		7.500	18.00	14.976			
C31		7.000	19.00	16.011			
C40	8.00	7.000	17.50	14.767	14.93	14.898	0.231
C39		7.500	17.00	14.114			
C38		7.000	17.50	14.767			
C37		7.000	18.50	15.596			
C36		6.500	18.00	15.419			

TABLE 7
Glass Faced Armour with Aromatic Polyamide Laminate Backing
Measured, Adjusted, and Fitted Data for the Projectile Erosion

	AVERAGE TIME µs	MEASURED TILE THICKNESS (mm)	MEASURED PROJECTILE LENGTH (mm)	ADJUSTED PROJECTILE LENGTH (mm)	AVERAGE ADJUSTED PROJECTILE LENGTH (mm)	FITTED ADJUSTED PROJECTILE LENGTH (mm)	PERCENTAGE VARIATION (%)
C45	10.00	7.000	17.00	14.351	13.77	14.030	-1.877
C25		7.000	15.00	12.686			
C41		7.500	17.00	14.114			
C43		7.000	16.50	13.935			
C46	12.00	7.000	15.50	13.103	13.38	13.162	1.601
C48		7.500	16.50	13.684			
C47		7.500	17.00	14.114			
C52		7.500	17.00	14.114			
C50		7.700	14.50	11.867			

Gradient for Fitted Length v Time	-0.434
Intercept for Fitted Length v Time	18.370
Correlation coefficient	0.989

TABLE 7 (continued)
Glass Faced Armour with Aromatic Polyamide Laminate Backing
Measured, Adjusted, and Fitted Data for the Projectile Erosion

	AVERAGE TIME µs	MEASURED TILE THICKNESS (mm)	MEASURED PENETRATION (mm)	ADJUSTED PENETRATION (mm)	AVERAGE ADJUSTED PENETRATION (mm)	FITTED PENETRATION (mm)	PERCENTAGE VARIATION (%)
B75	2.00	8.50	0.00	0.00	0.00	0.2752	-
B79		8.50	0.00	0.00			
B76		8.00	0.00	0.00			
B77		8.00	0.00	0.00			
B80	4.00	8.00	2.00	1.25	1.25	0.9172	26.62
B74		8.00	2.00	1.25			
B83		8.00	2.00	1.25			
B88	6.00	7.50	2.50	1.67	1.84	1.5592	15.15
B85		7.50	3.00	2.00			
B86		7.50	2.00	1.33			
B87		7.50	3.00	2.00			
B84		8.00	3.50	2.19			
B93	8.00	8.00	3.00	1.88	2.07	2.2012	-6.10
B91		7.75	3.00	1.94			
B92		7.50	3.00	2.00			
B90		8.00	2.50	1.56			
B89		7.50	4.50	3.00			
B98	10.00	7.75	4.50	2.90	2.68	2.8432	-6.13
C01		7.50	3.50	2.33			
B96		8.00	4.50	2.81			
B99		7.50	4.00	2.67			

TABLE 8
Alumina Faced Armour with GRP Backing
Measured, Adjusted and Fitted Data for Penetration of the Ceramic

	AVERAGE TIME µs	MEASURED TILE THICKNESS (mm)	MEASURED PENETRATION (mm)	ADJUSTED PENETRATION (mm)	AVERAGE ADJUSTED PENETRATION (mm)	FITTED PENETRATION (mm)	PERCENTAGE VARIATION (%)
C04	12.00	8.00	5.00	3.13	3.33	3.4852	-4.71
C05		7.75	4.50	2.90			
C02		7.50	4.50	3.00			
C03		7.00	6.00	4.29			
C09	14.00	8.00	4.00	2.50	4.03	4.1272	-2.29
C11		7.50	6.00	4.00			
C08		7.50	5.00	3.33			
C07		8.00	7.00	4.38			
C09		7.50	7.50	5.00			
C10		8.00	8.00	5.00			
C12	16.00	8.00	8.00	5.00	5.00	4.7692	4.62

Gradient of Fitted Penetration v Time	0.32
Intercept of Fitted Penetration v Time	-0.37
Correlation coefficient	0.98

TABLE 8 (continued)
Alumina Faced Armour with GRP Backing
Measured, Adjusted and Fitted Data for Penetration of the Ceramic

	AVERAGE TIME µs	MEASURED TILE THICKNESS (mm)	MEASURED PENETRATION (mm)	ADJUSTED PENETRATION (mm)	AVERAGE ADJUSTED PENETRATION (mm)	FITTED ADJUSTED PENETRATION (mm)	PERCENTAGE VARIATION (%)
B16	2.00	7.87	0.00	0.00	0.00	-0.0427	-
B17		7.87	0.00	0.00			
B21		7.87	0.00	0.00			
B19		7.87	0.00	0.00			
B22		7.87	0.00	0.00			
B20		7.87	0.00	0.00			
B18		7.87	0.00	0.00			
B27	4.00	7.87	1.00	0.64	0.51	0.6833	-34.45
B23		7.87	1.00	0.64			
B25		7.87	1.00	0.64			
B26		7.87	0.00	0.00			
B28		7.87	1.00	0.64			
B34	6.00	7.87	2.50	1.59	1.59	1.4093	11.27
B32		7.87	2.50	1.59			
B31		7.87	2.50	1.59			
B30		7.87	3.00	1.91			
B33		7.87	2.00	1.27			
B39	8.00	7.87	4.00	2.54	2.35	2.1353	9.16
B37		7.87	4.00	2.54			
B35		7.87	2.00	1.27			
B36		7.87	5.00	3.18			
B38		7.87	3.50	2.22			

TABLE 9
Alumina Faced Armour with Aromatic Polyamide Laminate Backing
Measured, Adjusted, and Fitted Data for the Penetration of the Projectile into the Ceramic

	AVERAGE TIME µs	MEASURED TILE THICKNESS (mm)	MEASURED PENETRATION (mm)	ADJUSTED PENETRATION (mm)	AVERAGE ADJUSTED PENETRATION (mm)	FITTED ADJUSTED PENETRATION (mm)	PERCENTAGE VARIATION (%)
B41	10.00	7.87	3.50	2.22	2.38	2.8613	-20.10
B42		7.87	5.00	3.18			
B46		7.87	4.00	2.54			
B47		7.87	2.75	1.75			
B43		7.87	3.50	2.22			
B52	12.00	7.87	7.50	4.76	3.81	3.5873	5.89
B51		7.87	5.00	3.18			
B49		7.87	5.50	3.49			
B50		7.87	6.75	4.29			

Gradient of Fitted Penetration v Time	0.36
Intercept of Fitted Penetration v Time	-0.77
Correlation Coefficient	0.98

TABLE 9 (continued)
Alumina Faced Armour with Aromatic Polyamide Laminate Backing
Measured, Adjusted, and Fitted Data for the Penetration of the Projectile into the Ceramic

	AVERAGE TIME µs	MEASURED TILE THICKNESS (mm)	MEASURED PENETRATION (mm)	ADJUSTED PENETRATION (mm)	AVERAGE ADJUSTED PENETRATION (mm)	FITTED ADJUSTED PENETRATION (mm)	PERCENTAGE VARIATION (%)
C27	4.00	7.500	3.00	2.400	1.44	1.6880	-17.222
C28		7.500	3.00	2.400			
C30		7.500	1.00	0.800			
C29		7.500	1.00	0.800			
C26		7.500	1.00	0.800			
C35	6.00	7.500	3.00	2.400	2.92	2.8240	3.288
C33		7.000	3.50	3.000			
C32		7.000	3.50	3.000			
C34		7.500	4.00	3.200			
C31		7.000	3.50	3.000			
C40	8.00	7.000	5.00	4.286	4.29	3.9600	7.789
C39		7.500	5.00	4.000			
C38		7.000	5.00	4.286			
C37		7.000	5.00	4.286			
C36		6.500	5.00	4.615			

TABLE 10
Glass Faced Armour with Aromatic Polyamide Laminate Backing
Measured, Adjusted, and Fitted Data for the Penetration of the Projectile into the Ceramic

	AVERAGE TIME µs	MEASURED TILE THICKNESS (mm)	MEASURED PENETRATION (mm)	ADJUSTED PENETRATION (mm)	AVERAGE ADJUSTED PENETRATION (mm)	FITTED ADJUSTED PENETRATION (mm)	PERCENTAGE VARIATION (%)
C45	10.00	7.000	6.50	5.571	5.17	5.0960	1.459
C25		7.000	6.00	5.143			
C41		7.500	5.50	4.400			
C43		7.000	6.50	5.571			
C46	12.00	7.000	7.00	6.000	6.00	6.2320	-3.894
C48		7.500	7.50	6.000			
C47		7.500	7.50	6.000			
C52		7.500	7.50	6.000			
C50		7.700	7.69	5.992			

Gradient for Fitted Penetration v Time	0.568
Intercept for Fitted Penetration v Time	-0.584
Correlation Coefficient	0.99

TABLE 10 (continued)
Glass Faced Armour with Aromatic Polyamide Laminate Backing
Measured, Adjusted, and Fitted Data for the Penetration of the Projectile into the Ceramic

	AVERAGE TIME µs	ADJUSTED PROJECTILE (mm)	ADJUSTED PENETRATION (mm)	MEASURED REAR DISPLACEMENT (mm)	AVERAGE REAR DISPLACEMENT (mm)	FITTED REAR DISPLACEMENT (mm)	PERCENTAGE VARIATION (%)
B75	2.00	16.76	0.00	2.24	1.69	3.1200	-84.91
B79		16.76	0.00	2.24			
B76		16.83	0.00	2.17			
B77		18.90	0.00	0.10			
B80	4.00	15.32	1.25	4.93	5.42	5.1400	5.09
B74		14.83	1.25	5.42			
B83		14.35	1.25	5.90			
B88	6.00	13.56	1.67	7.11	7.50	7.1600	4.49
B85		13.56	2.00	7.44			
B86		12.64	1.33	7.69			
B87		13.56	2.00	7.44			
B84		13.39	2.19	7.80			
B93	8.00	11.98	1.88	8.89	9.26	9.1800	0.88
B91		12.54	1.94	8.40			
B92		12.18	2.00	8.82			
B90		11.07	1.56	9.49			
B89		11.29	3.00	10.71			
B98	10.00	10.73	2.90	11.17	11.68	11.2000	4.09
C01		9.97	2.33	11.36			
B96		10.62	2.81	11.19			
B99		8.69	2.67	12.98			

TABLE 11
Alumina Faced Armour with GRP Backing
Measured, Adjusted, and Fitted Data for Displacement of Projectile Rear

	AVERAGE TIME µs	ADJUSTED PROJECTILE (mm)	ADJUSTED PENETRATION (mm)	MEASURED REAR DISPLACEMENT (mm)	AVERAGE REAR DISPLACEMENT (mm)	FITTED REAR DISPLACEMENT (mm)	PERCENTAGE VARIATION (%)
C04	12.00	9.31	3.13	12.82	12.92	13.2200	-2.34
C05		8.56	2.90	13.34			
C02		9.11	3.00	12.89			
C03		10.66	4.29	12.62			
C09	14.00	10.18	2.50	11.32	13.89	15.2400	-9.71
C11		8.27	4.00	14.73			
C08		9.11	3.33	13.22			
C07		8.03	4.38	15.34			
C09		9.97	5.00	14.03			
C10		9.31	5.00	14.69			
C12	16.00	7.21	5.00	17.00	17.00	17.2600	-1.53

Gradient of Fitted Displacement v Time	1.01
Intercept of Fitted Displacement v Time	1.10
Correlation coefficient	0.98

TABLE 11 (continued)
Alumina Faced Armour with GRP Backing
Measured, Adjusted, and Fitted Data for Displacement of Projectile Rear

	AVERAGE TIME µs	ADJUSTED PROJECTILE (mm)	ADJUSTED PENETRATION (mm)	MEASURED REAR DISPLMENT (mm)	AVERAGE REAR DISPLMENT (mm)	FITTED REAR DISPLMENT (mm)	PERCENTAGE VARIATION (%)
B16	2.00	18.29	0.00	0.71	1.01	0.6680	33.70
B17		16.75	0.00	2.25			
B21		18.09	0.00	0.91			
B19		18.54	0.00	0.46			
B22		17.64	0.00	1.36			
B20		19.00	0.00	0.00			
B18		17.64	0.00	1.36			
B27	4.00	16.34	0.64	3.30	2.27	2.8420	-24.98
B23		16.34	0.64	3.30			
B25		16.34	0.64	3.30			
B26		20.81	0.00	-1.81			
B28		16.34	0.64	3.30			
B34	6.00	15.86	1.59	4.73	5.48	5.0160	8.45
B32		15.39	1.59	5.20			
B31		14.45	1.59	6.13			
B30		15.39	1.91	5.52			
B33		14.45	1.27	5.82			
B39	8.00	13.99	2.54	7.55	7.03	7.1900	-2.24
B37		14.45	2.54	7.09			
B35		16.34	1.27	3.93			
B36		12.63	3.18	9.55			
B38		14.18	2.22	7.05			

TABLE 12
Alumina Faced Armour with Aromatic Polyamide Laminate Backing
Measured, Adjusted, Fitted Data for the Displacement of the Projectile Rear

	AVERAGE TIME µs	ADJUSTED PROJECTILE (mm)	ADJUSTED PENETRATION (mm)	MEASURED REAR DISPLMENT (mm)	AVERAGE REAR DISPLMENT (mm)	FITTED REAR DISPLMENT (mm)	PERCENTAGE VARIATION (%)
B41	10.00	11.74	2.22	9.48	8.92	9.3640	-4.92
B42		12.18	3.18	9.99			
B46		12.18	2.54	9.36			
B47		12.18	1.75	8.56			
B43		13.99	2.22	7.23			
B52	12.00	11.30	4.76	12.46	11.94	11.5380	3.34
B51		10.01	3.18	12.16			
B49		11.30	3.49	11.19			
B50		11.30	4.29	11.98			

Gradient of Fitted Rear Displacement v Time	1.09
Intercept of Fitted Rear Displacement v Time	-1.51
Correlation coefficient	0.99

TABLE 12 (continued)
Alumina Faced Armour with Aromatic Polyamide Laminate Backing
Measured, Adjusted, Fitted Data for the Displacement of the Projectile Rear

	AVERAGE TIME µs	ADJUSTED PROJECTILE (mm)	ADJUSTED PENETRATION (mm)	REAR DISPLACEMENT (mm)	AVERAGE REAR DISPLACEMENT (mm)	FITTED REAR DISPLACEMENT (mm)	PERCENTAGE VARIATION (%)
C27	4.00	15.408	2.400	5.992	3.64	4.0560	-11.420
C28		16.711	2.400	4.689			
C30		17.584	0.800	2.216			
C29		16.711	0.800	3.089			
C26		17.584	0.800	2.216			
C35	6.00	16.276	2.400	5.124	6.31	6.0610	3.974
C33		15.596	3.000	6.404			
C32		15.182	3.000	6.818			
C34		14.976	3.200	7.224			
C31		16.011	3.000	5.989			
C40	8.00	14.767	4.286	8.519	8.36	8.0660	3.540
C39		14.114	4.000	8.886			
C38		14.767	4.286	8.519			
C37		15.596	4.286	7.689			
C36		15.419	4.615	8.196			

TABLE 13
Glass Faced Armour with Aromatic Polyamide Laminate Backing
Measured, Adjusted, and Fitted Data for the Displacement of the Projectile Rear

	AVERAGE TIME µs	ADJUSTED PROJECTILE (mm)	ADJUSTED PENETRATION (mm)	REAR DISPLACEMENT (mm)	AVERAGE REAR DISPLACEMENT (mm)	FITTED REAR DISPLACEMENT (mm)	PERCENTAGE VARIATION (%)
C45	10.00	14.351	5.571	10.220	10.40	10.0710	3.162
C25		12.686	5.143	11.457			
C41		14.114	4.400	9.286			
C43		13.935	5.571	10.636			
C46	12.00	13.103	6.000	11.897	11.62	12.0760	-3.904
C48		13.684	6.000	11.316			
C47		14.114	6.000	10.886			
C52		14.114	6.000	10.886			
C50		11.867	5.992	13.126			

Gradient for Fitted Displacement v Time	1.003
Intercept for Fitted Displacement v Time	0.046
Correlation Coefficient	0.99

TABLE 13 (continued)
Glass Faced Armour with Aromatic Polyamide Laminate Backing
Measured, Adjusted, and Fitted Data for the Displacement of the Projectile Rear

	AVERAGE ADJUSTED PENETRATION (mm)	MEASURED TILE THICKNESS (mm)	BULLET DIAMETER (mm)	ADJUSTED BULLET DIAMETER (mm)	ADJUSTED BULLET RADIUS (mm)	AVERAGE BULLET RADIUS (mm)	FITTED BULLET RADIUS (mm)	PERCENTAGE VARIATION (%)
B75	0.00	8.50	4.50	2.65	1.32	1.20	1.68	-39.80
B79		8.50	5.50	3.24	1.62			
B76		8.00	5.00	3.13	1.56			
B77		8.00	1.00	0.63	0.31			
B80	1.25	8.00	9.50	5.94	2.97	3.23	3.21	0.45
B74		8.00	11.50	7.19	3.59			
B83		8.00	10.00	6.25	3.13			
B88	1.84	7.50	11.50	7.67	3.83	3.95	3.93	0.35
B85		7.50	12.50	8.33	4.17			
B86		7.50	12.50	8.33	4.17			
B87		7.50	11.00	7.33	3.67			
B84		8.00	12.50	7.81	3.91			
B93	2.07	8.00	15.50	9.69	4.84	4.54	4.22	7.02
B91		7.75	13.50	8.71	4.35			
B92		7.50	14.50	9.67	4.83			
B90		8.00	15.00	9.38	4.69			
B89		7.50	12.00	8.00	4.00			
B98	2.68	7.75	17.00	10.97	5.48	5.68	4.96	12.60
C01		7.50	20.00	13.33	6.67			
B96		8.00	12.50	7.81	3.91			
B99		7.50	20.00	13.33	6.67			

TABLE 14
Alumina Faced Armour with GRP Backing
Measured, Adjusted, and Fitted Data for the Spreading of the Projectile Tip

	AVERAGE ADJUSTED PENETRATION (mm)	MEASURED TILE THICKNESS (mm)	BULLET DIAMETER (mm)	ADJUSTED BULLET DIAMETER (mm)	ADJUSTED BULLET RADIUS (mm)	AVERAGE BULLET RADIUS (mm)	FITTED BULLET RADIUS (mm)	PERCENTAGE VARIATION (%)
C04	3.33	8.00	18.00	11.25	5.63	6.17	5.76	6.66
C05		7.75	18.50	11.94	5.97			
C02		7.50	20.00	13.33	6.67			
C03		7.00	18.00	12.86	6.43			
C09	4.03	8.00	18.00	11.25	5.63	5.63	6.63	-17.72
C11		7.50	15.00	10.00	5.00			
C08		7.50	20.00	13.33	6.67			
C07		8.00	16.50	10.31	5.16			
C09		7.50	18.50	12.33	6.17			
C10		8.00	16.50	10.31	5.16			
C12	5.00	8.00	25.00	15.63	7.81	7.81	7.81	0.05

Gradient of Fitted Radius v Penetration	1.23
Intercept of Fitted Radius v Penetration	1.68
Correlation Coefficient	0.96

TABLE 14 (continue)
Alumina Faced Armour with GRP Backing
Measured, Adjusted, and Fitted Data for the Spreading of the Projectile Tip

	AVERAGE ADJUSTED PENETRATION (mm)	MEASURED TILE THICKNESS (mm)	BULLET DIAMETER (mm)	ADJUSTED BULLET DIAMETER (mm)	ADJUSTED BULLET RADIUS (mm)	AVERAGE ADJUSTED RADIUS (mm)	FITTED ADJUSTED RADIUS (mm)	VARIATION (%)
B16	0.00	7.87	3.50	2.22	1.11	1.07	1.24	-16.33
B17		7.87	4.00	2.54	1.27			
B21		7.87	3.00	1.91	0.95			
B19		7.87	2.50	1.59	0.79			
B22		7.87	3.50	2.22	1.11			
B20		7.87	3.00	1.91	0.95			
B18		7.87	4.00	2.54	1.27			
B27	0.51	7.87	7.00	4.45	2.22	1.81	1.77	2.44
B23		7.87	7.50	4.76	2.38			
B25		7.87	7.50	4.76	2.38			
B26		7.87	0.00	0.00	0.00			
B28		7.87	6.50	4.13	2.06			
B34	1.59	7.87	12.20	7.75	3.88	3.00	2.88	3.83
B32		7.87	8.50	5.40	2.70			
B31		7.87	10.00	6.35	3.18			
B30		7.87	7.00	4.45	2.22			
B33		7.87	9.50	6.04	3.02			

TABLE 15
Alumina Faced Armour with Aromatic Polyamide Laminate Backing
Measured, Adjusted, and Fitted Data for Spreading of the Projectile Tip

	AVERAGE ADJUSTED PENETRATION (mm)	MEASURED TILE THICKNESS (mm)	BULLET DIAMETER (mm)	ADJUSTED BULLET DIAMETER (mm)	ADJUSTED BULLET RADIUS (mm)	AVERAGE ADJUSTED RADIUS (mm)	FITTED ADJUSTED RADIUS (mm)	VARIATION (%)
B39	2.35	7.87	11.00	6.99	3.49	3.41	3.67	-7.55
B37		7.87	8.75	5.56	2.78			
B35		7.87	9.50	6.04	3.02			
B36		7.87	12.00	7.62	3.81			
B38		7.87	12.50	7.94	3.97			
B41	2.38	7.87	11.00	6.99	3.49	3.65	3.71	-1.43
B42		7.87	15.50	9.85	4.92			
B46		7.87	11.50	7.31	3.65			
B47		7.87	10.00	6.35	3.18			
B43		7.87	9.50	6.04	3.02			
B52	3.81	7.87	15.50	9.85	4.92	5.16	5.18	-0.43
B51		7.87	21.50	13.66	6.83			
B49		7.87	12.00	7.62	3.81			
B50		7.87	16.00	10.17	5.08			

Gradient of Fitted Radius v Penetration	1.03
Intercept of Fitted Radius v Penetration	1.24
Correlation Coefficient	0.99

TABLE 15 (continued)
Alumina Faced Armour with Aromatic Polyamide Laminate Backing
Measured, Adjusted, and Fitted Data for Spreading of the Projectile Tip

	AVERAGE ADJUSTED PENETRAION (mm)	MEASURED TILE THICKNESS (mm)	BULLET EXPANSION (mm)	ADJUSTED BULLET DIAMETER (mm)	ADJUSTED BULLET RADIUS (mm)	AVERAGE ADJUSTED RADIUS (mm)	FITTED ADJUSTED RADIUS (mm)	PERCENTAGE VARIATION (%)
C27	1.44	7.500	5.50	4.400	2.200	2.240	2.493	-11.316
C28		7.500	7.50	6.000	3.000			
C30		7.500	4.00	3.200	1.600			
C29		7.500	5.50	4.400	2.200			
C26		7.500	5.50	4.400	2.200			
C35	2.92	7.500	7.00	5.600	2.800	3.423	3.230	5.624
C33		7.000	8.50	7.286	3.643			
C32		7.000	8.50	7.286	3.643			
C34		7.500	9.00	7.200	3.600			
C31		7.000	8.00	6.857	3.429			
C40	4.29	7.000	10.00	8.571	4.286	4.255	3.915	7.986
C39		7.500	9.50	7.600	3.800			
C38		7.000	10.00	8.571	4.286			
C37		7.000	10.00	8.571	4.286			
C36		6.500	10.00	9.231	4.615			

TABLE 16
Glass Faced Armour with Aromatic Polyamide Laminate Backing
Measured, Adjusted, and Fitted Data for the Spreading of the Projectile Tip

	AVERAGE ADJUSTED PENETRAION (mm)	MEASURED TILE THICKNESS (mm)	BULLET EXPANSION (mm)	ADJUSTED BULLET DIAMETER (mm)	ADJUSTED BULLET RADIUS (mm)	AVERAGE ADJUSTED RADIUS (mm)	FITTED ADJUSTED RADIUS (mm)	PERCENTAGE VARIATION (%)
C45	5.17	7.000	11.50	9.857	4.929	4.325	4.351	-0.609
C25		7.000	10.00	8.571	4.286			
C41		7.500	9.50	7.600	3.800			
C43		7.000	10.00	8.571	4.286			
C46	6.00	7.000	9.50	8.143	4.071	4.509	4.763	-5.628
C48		7.500	10.50	8.400	4.200			
C47		7.500	12.00	9.600	4.800			
C52		7.500	12.00	9.600	4.800			
C50		7.700	12.00	9.351	4.675			

Gradient of Fitted Radius v Penetration	0.498
Intercept of Fitted Radius v Penetration	1.777
Correlation Coefficient	0.96

TABLE 16 (continued)
Glass Faced Armour with Aromatic Polyamide Laminate Backing
Measured, Adjusted, and Fitted Data for the Spreading of the Projectile Tip

	ADJUSTED PENETRATION (mm)	BULLET DIAMETER (mm)	FRACTURE CONE DIAMETER (mm)	FRACTURE CONE ANGLE	
B16	0.00	3.50	0.00	-12.34	
B17	0.00	4.00	0.00	-14.04	
B21	0.00	3.00	0.00	-10.62	
B19	0.00	2.50	0.00	-8.88	
B22	0.00	3.50	0.00	-12.34	
B20	0.00	3.00	0.00	-10.62	
B18	0.00	4.00	0.00	-14.04	
B27	0.64	7.00	19.00	40.60	*
B23	0.64	7.50	19.00	39.40	*
B25	0.64	7.50	17.50	35.54	*
B26	0.00	0.00	0.00	0.00	
B28	0.64	6.50	14.50	29.74	*
B34	1.59	12.20	25.00	49.33	*
B32	1.59	8.50	22.50	51.84	*
B31	1.59	10.00	22.00	47.49	*
B30	1.91	7.00	18.00	47.73	*
B33	1.27	9.50	21.50	45.00	*
B39	2.54	11.00	22.00	53.97	*
B37	2.54	8.75	14.50	35.71	*
B35	1.27	9.50	16.00	28.44	*
B36	3.18	12.00	23.00	61.39	*
B38	2.22	12.50	18.75	34.78	*
B41	2.22	11.00	24.00	55.30	*
B42	3.18	15.50	28.00	64.36	*
B46	2.54	11.50	19.25	44.09	*
B47	1.75	10.00	17.00	33.69	*
B43	2.22	9.50	19.00	46.55	*
B52	4.76	15.50	23.00	82.41	*
B51	3.18	21.50	25.00	30.26	*
B49	3.49	12.00	16.50	41.99	*
B50	4.29	16.00	22.50	68.96	*

Table 17
Fracture Cone Angles for
Alumina Faced Armour with Aramatic Polyamide Backing

Number of Layers	Areal Density kgm^{-2}	Vc/(m/s)		
		Nominal Fragment Weight		
		0.48g	1.1g	2.8g
15	4.30	392	330	307
19	5.30	471	378	335
22	6.25	505	424	352
28	7.90	593	487	400

Measured Vc's for Laminates
TABLE 18

Laminate Areal Density kgm^{-2}	Actual FSP Weight (g)	Value of Constant "a" x 10^{-3}	Actual FSP Weight (g)	Value of Constant "a" x 10^{-3}	Actual FSP Weight (g)	Value of Constant "a" x 10^{-3}
4.3	0.48	0.43	1.11	1.19	2.91	3.98
5.3	0.47	0.49	1.10	1.03	2.90	3.79
6.25	0.47	0.41	1.10	1.08	2.91	3.70
7.90	0.48	0.48	1.11	1.0	2.89	3.06

Values for the Constant "a" and the Measured Weight of the Fragment Simulating Projectiles
TABLE 19

2mm Alumina Faced Armour with Aramid Backing
at an Areal Density of 11.4kg/ sq m

ANGLE	CRITICAL VELOCITY m/s	SECANT	APPARENT THICKNESS t' (mm)	K	C	PREDICTED CRITICAL VELOCITY m/s	% VARIATION
0	-	-	-	-	-	442	-
30	-	-	-	-	-	458	-
40	381	1.306	2.611	10752	6653	472	-23.885
50	504	1.556	3.113	18816	10665	493	2.183
60	522	2.001	4.003	20184	10088	525	-0.575
70	590	2.928	5.856	25785	10656	578	2.034

Table 20 (Part I)
Results for Alumina Faced Armours with Aromatic Polyamide Backing
Impacted at Oblique Angles of Incidence

3mm Alumina Faced Armour with Aramid Backing
at an Areal Density of 17.1kg/sq

ANGLE	CRITICAL VELOCITY m/s	SECANT	APPARENT THICKNESS t′ (mm)	K	C	PREDICTED CRITICAL VELOCITY m/s	% VARIATION
0	450	1.000	3.000	10125	5845.671	-	
30	617	1.155	3.465	19034	10226.060	617	0.000
40	640	1.306	3.917	20480	10347.730	636	0.625
50	665	1.556	4.669	22111	10232.708	664	0.150
60	724	2.001	6.004	26208	10695.464	707	2.348
70	811	2.928	8.783	32886	11096.414	778	4.069

Table 20 (Part II)
Results for Alumina Faced Armours with Aromatic Polyamide Backing
Impacted at Oblique Angles of Incidence

4mm Alumina Faced Armour with Aramid Backing
at an Areal Density of 21.9kg/sq m

ANGLE	CRITICAL VELOCITY m/s	SECANT	4mm ALUMINA APPARENT THICKNESS t' (mm)	K	C	PREDICTED CRITICAL VELOCITY m/s	% VARIATION
0	854	1.000	4.000	28050	14025.000	847	0.820
30	859	1.155	4.619	28380	19358.283	860	-0.116
40	857	1.306	5.223	28248	18685.752	872	-1.750
50	900	1.556	6.226	31153	19722.242	889	1.222
60	924	2.001	8.006	32837	19521.432	914	1.082
70	950	2.928	11.711	34711	18763.690	953	-0.316

Table 20 (Part III)
Results for Alumina Faced Armours with Aromatic Polyamide Backing
Impacted at Oblique Angles of Incidence

TEST NUMBER	MAXIMUM RING DIAMETER (mm)	IMPACT VELOCITY (m/s)
1	26.72	158
2	24.76	214
3	23.90	229
4	25.13	231
5	20.00	254
6	15.24	299
7	16.92	305
8	14.72	315
9	14.90	323
10	16.30	366
11	0.00	409
12	0.00	415
13	15.22	423
14	0.00	432
15	0.00	454
16	0.00	454
17	0.00	464
18	0.00	476
19	0.00	501
20	0.00	505
21	0.00	509
22	0.00	537
23	0.00	595
24	0.00	599

TABLE 21
Maximum Diameter of the Rings
Measured on 2.9mm Thick Polycarbonate

DISTANCE FROM TIP (mm)	MEASURED DIAMETER (mm)	MEASURED RADIUS (mm)	FITTED RADIUS (mm)	PERCENTAGE VARIATION (%)
1	2.004	1.002	0.941	6.056
2	2.656	1.328	1.354	-1.986
3	3.268	1.634	1.683	-3.018
4	3.790	1.895	1.945	-2.643
5	4.258	2.129	2.154	-1.187
6	4.660	2.330	2.323	0.292
7	4.996	2.498	2.462	1.448
8	5.280	2.640	2.578	2.356
9	5.500	2.750	2.676	2.673
10	5.640	2.820	2.761	2.096
11	5.672	2.836	2.832	0.150
12	5.688	2.844	2.887	-1.526
13	5.544	2.772	2.924	-5.480
14	5.730	2.865	2.935	-2.446
15	5.770	2.885	2.912	-0.945
16	5.780	2.890	2.845	1.569
17	5.700	2.850	2.719	4.597
18	5.280	2.640	2.520	4.555
19	4.194	2.097	2.229	-6.300

Measured and Fitted Values for Radius of 5.56mm Bullets
TABLE 22

	Alumina/Aramid	Alumina/GRP	Glass/Aramid
Facing Density (kgm^{-3})	3.53×10^3	3.53×10^3	2.47×10^3
Penetration Velocity (m/s)	365	321	564
Facing Compressive Strength (GNm^{-2})	2.1	2.1	0.7
Calculated Value (L.H.S) (GNm^{-2})	2.35	2.28	1.096
Calculated Value (R.H.S) (GNm^{-2})	2.31	2.65	1.112
% Difference	0.7	16.1	1.4

The Values Calculated from both Sides of the Bernoulli Equation for all the armour Combinations Studied
TABLE 23

	ADJUSTED PROJECTILE LENGTH (mm)	BULLET RADIUS (mm)	BULLET AREA (mm^2)	AVERAGE BULLET AREA (mm^2)	BULLET ENERGY (J)
B75	16.76	1.440	6.52	5.02	0.00
B79	16.76	1.440	6.52		0.00
B76	16.83	1.416	6.30		0.00
B77	18.90	0.482	0.73		0.00
B80	15.32	1.867	10.95	12.33	238.62
B74	14.83	1.983	12.36		269.42
B83	14.35	2.087	13.69		298.32
B88	13.56	2.233	15.67	16.17	455.34
B85	13.56	2.233	15.67		546.41
B86	12.64	2.376	17.75		412.54
B87	13.56	2.233	15.67		546.41
B84	13.39	2.262	16.08		613.26
B93	11.98	2.464	19.08	19.37	623.70
B91	12.54	2.390	17.96		605.91
B92	12.18	2.438	18.68		651.45
B90	11.07	2.570	20.76		565.52
B89	11.29	2.547	20.38		1065.97
B98	10.73	2.606	21.34	22.45	1080.34
C01	9.97	2.679	22.56		917.82
B96	10.62	2.617	21.52		1055.28
B99	8.69	2.785	24.37		1133.02
C04	9.31	2.737	23.54	23.33	1282.25
C05	8.56	2.793	24.52		1241.32
C02	9.11	2.752	23.81		1245.21
C03	10.66	2.613	21.46		1603.31
C09	10.18	2.660	22.24	23.70	969.17
C11	8.27	2.814	24.89		1735.89
C08	9.11	2.752	23.81		1383.56
C07	8.03	2.830	25.17		1919.52
C09	9.97	2.679	22.56		1966.75
C10	9.31	2.737	23.54		2051.60
C12	7.21	2.877	26.02	26.02	2268.16

CALCULATED ENERGY EXPENDED (J) 1026

ACTUAL ENERGY EXPENDED (J) 979

TABLE 24
BULLET TIP RADIUS, TIP AREA, AND CALCULATED ENERGY
FOR ALUMINA FACED GRP BACKED ARMOURS

	ADJUSTED PROJECTILE LENGTH (mm)	BULLET RADIUS (mm)	BULLET AREA (mm^2)	AVERAGE BULLET AREA (mm^2)	BULLET ENERGY (J)
B16	18.29	0.804	2.03	2.97	0.00
B17	16.75	1.445	6.56		0.00
B21	18.09	0.899	2.54		0.00
B19	18.54	0.675	1.43		0.00
B22	17.64	1.101	3.81		0.00
B20	19.00	0.425	0.57		0.00
B18	17.64	1.101	3.81		0.00
B27	16.34	1.580	7.85	6.73	86.90
B23	16.34	1.580	7.85		86.90
B25	16.34	1.580	7.85		86.90
B26	20.81	-0.847	2.25		0.00
B28	16.34	1.580	7.85		86.90
B34	15.86	1.723	9.33	11.53	258.38
B32	15.39	1.850	10.76		297.97
B31	14.45	2.065	13.40		371.13
B30	15.39	1.850	10.76		357.56
B33	14.45	2.065	13.40		296.91
B39	13.99	2.156	14.61	13.55	647.13
B37	14.45	2.065	13.40		593.81
B35	16.34	1.580	7.85		173.80
B36	12.63	2.377	17.76		983.82
B38	14.18	2.121	14.13		547.94
B41	11.74	2.494	19.54	18.04	757.56
B42	12.18	2.438	18.68		1034.64
B46	12.18	2.438	18.68		827.71
B47	12.18	2.438	18.68		569.05
B43	13.99	2.156	14.61		566.24
B52	11.30	2.544	20.35	20.88	1690.34
B51	10.01	2.675	22.49		1245.61
B49	11.30	2.544	20.35		1239.58
B50	11.30	2.544	20.35		1521.30

ACTUAL ENERGY EXPENDED (J)	515
CALCULATED ENERGY EXPENDED (J)	597

TABLE 25
BULLET TIP RADIUS, TIP AREA, AND CALCULATED ENERGY
FOR ALUMINA FACED ARAMID LAMINATE BACKED ARMOURS

	ADJUSTED PROJECTILE LENGTH (mm)	BULLET DIAMETER (mm)	BULLET AREA (mm^2)	AVERAGE BULLET AREA (mm^2)	BULLET ENERGY (J)
C27	15.408	1.845	10.702	6.400	255.519
C28	16.711	1.457	6.674		159.354
C30	17.584	1.125	3.975		31.632
C29	16.711	1.457	6.674		53.118
C26	17.584	1.125	3.975		31.632
C35	16.276	1.600	8.045	10.077	192.084
C33	15.596	1.796	10.140		302.624
C32	15.182	1.902	11.367		339.267
C34	14.976	1.951	11.959		380.712
C31	16.011	1.680	8.872		264.802
C40	14.767	1.998	12.548	12.040	534.985
C39	14.114	2.133	14.295		568.861
C38	14.767	1.998	12.548		534.985
C37	15.596	1.796	10.140		432.321
C36	15.419	1.843	10.670		489.934
C45	14.351	2.086	13.675	15.092	757.990
C25	12.686	2.370	17.647		902.906
C41	14.114	2.133	14.295		625.747
C43	13.935	2.166	14.749		817.479
C46	13.103	2.307	16.733	16.000	998.797
C48	13.684	2.211	15.371		917.489
C47	14.114	2.133	14.295		853.292
C52	14.114	2.133	14.295		853.292
C50	11.867	2.478	19.306		1150.877

ACTUAL ENERGY EXPENDED (J)	264.000
CALCULATED ENERGY EXPENDED (J)	518.738

TABLE 26
BULLET TIP RADIUS, TIP AREA, AND CALCULATED ENERGY
FOR GLASS FACED ARAMID LAMINATE BACKED ARMOURS

Areal Density (kgm^{-2})	Calculated Energy of the Fragment Simulating Projectiles (FSP) (J)		
	0.48g FSP	1.1g FSP	2.8g FSP
4.30	36.879	60.440	137.132
5.30	52.133	78.586	162.726
6.25	59.931	98.877	180.280
7.90	84.396	131.629	231.200

Calculated Energy of The Fragments
TABLE 27

Areal Density (kgm^{-2})	Calculated Energy per Layer for three Fragment Simulating Projectile (FSP) Weights (J/Layer)		
	0.48g FSP	1.1g FSP	2.8g FSP
4.30	2.401	3.936	8.930
5.30	2.754	4.152	8.597
6.25	2.685	4.430	8.077
7.90	2.991	4.665	8.194

Calculated Energy per Layer of the Laminates
TABLE 28

Fragment Simulating Projectile	Areal Density kgm^{-2}	Measured Vc (m/s)	Percentage Error in Vc (%)	Calculated Vc (m/s)	Percentage Variation (%)
0.48g FSP	4.30	392	2.8	419	6.9
	5.30	471	6.1	470	-0.175
	6.25	505	4.5	510	1.1
	7.90	593	2.5	568	-4.2
1.1g FSP	4.30	330	1.1	354	7.3
	5.30	378	2.5	395	4.4
	6.25	424	2.1	428	1.1
	7.90	487	1.0	480	-1.4
2.8g FSP	4.30	307	3.6	289	-5.7
	5.30	335	1.4	321	-3.9
	6.25	352	2.5	348	-0.9
	7.90	400	2.2	393	-1.6

Calculated and Measured Critical Velocites for Laminates against FSP's
TABLE 29

Thickness (mm)	Vc (m/s)	Energy (J)	Areal Density (kgm^{-2})
2	150	12.75	2.4
3	180	17.82	3.6
5	300	49.5	6.0
9	525	151	10.8

Critical Velocities of 1.1g FSP's
Against Polycarbonate Sheet
TABLE 30

FACING MATERIAL	TILE THICKNESS (mm)	BACKING AREAL (kgm^{-2})	ARMOUR AREAL (kgm^{-2})	PREDICTED CRITICAL VELOCITY (m/s)	MEASURED CRITICAL VELOCITY (m/s)	VARIATION (%)	FACING MATERIAL DENSITY (kgm^{-3})	FACING MATERIAL MODULUS (Nm^{-2}) $x10^9$	FACING MATERIAL STRENGTH (Nm^{-2}) $x10^9$
ALUMINA (97.5%)	4.00	7.50	22.62	916	855	-7.13	3.79	338	2.40
ALUMINA (97.5%)	5.00	5.00	23.90	938	861	-8.94	3.79	338	2.40
ALUMINA (97.5%)	5.00	7.00	25.90	975	956	1.99	3.79	338	2.40
ALUMINA (97.5%)	5.00	10.00	28.90	1025	1060	3.30	3.79	338	2.40
BORON CARBIDE	5.22	7.78	20.54	1051	1021	-2.94	2.52	482	2.76
SILICON CARBIDE	3.97	7.78	20.57	920	872	-5.50	3.11	401	2.43
SILICON CARBIDE	3.21	8.97	19.49	885	836	-5.86	3.11	401	2.43
SILICON NITRIDE	5.50	7.35	25.17	867	885	2.03	3.23	300	1.70

TABLE 31
COMPARASON OF THE MEASURED AND PREDICTED CRITICAL VELOCITY FOR SOME CERAMIC FACING MATERIALS

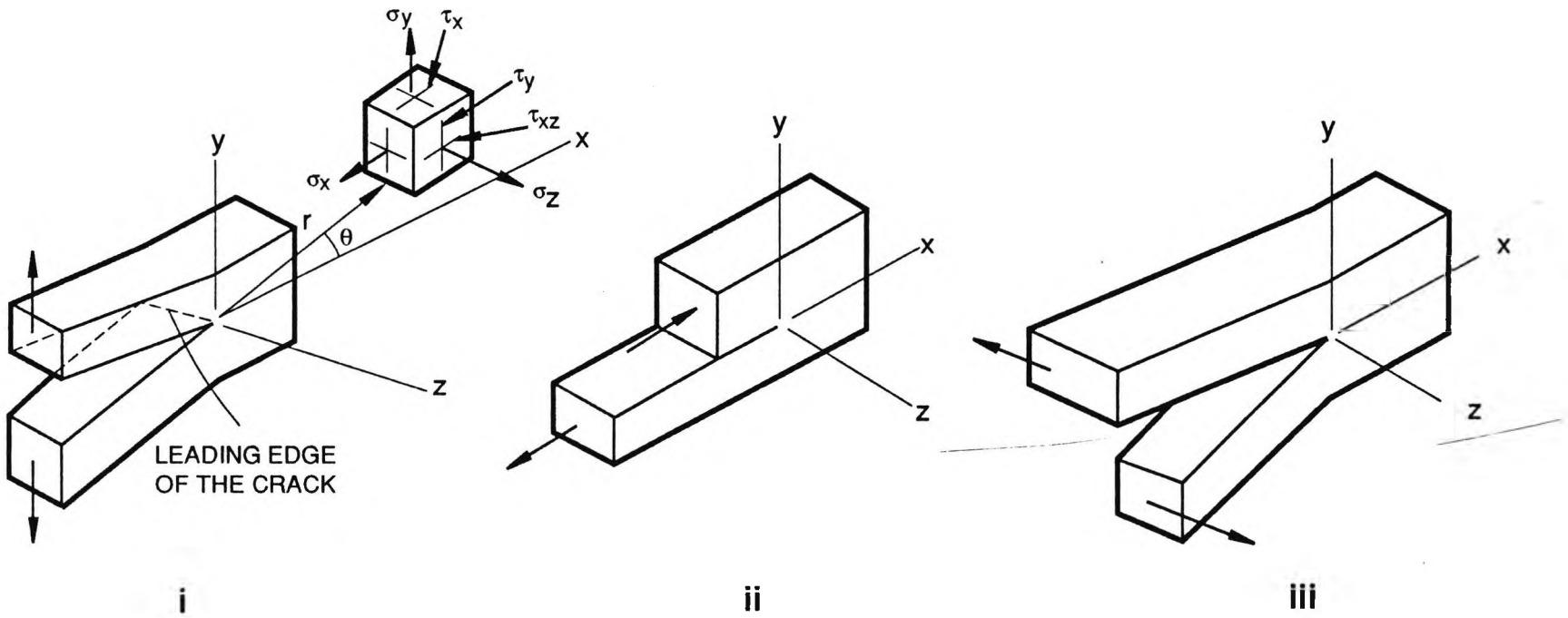

FIG. 1. BASIC MODES OF CRACK LOADING :
I OPENING MODE : II EDGE SLIDING MODE : III TEARING MODE

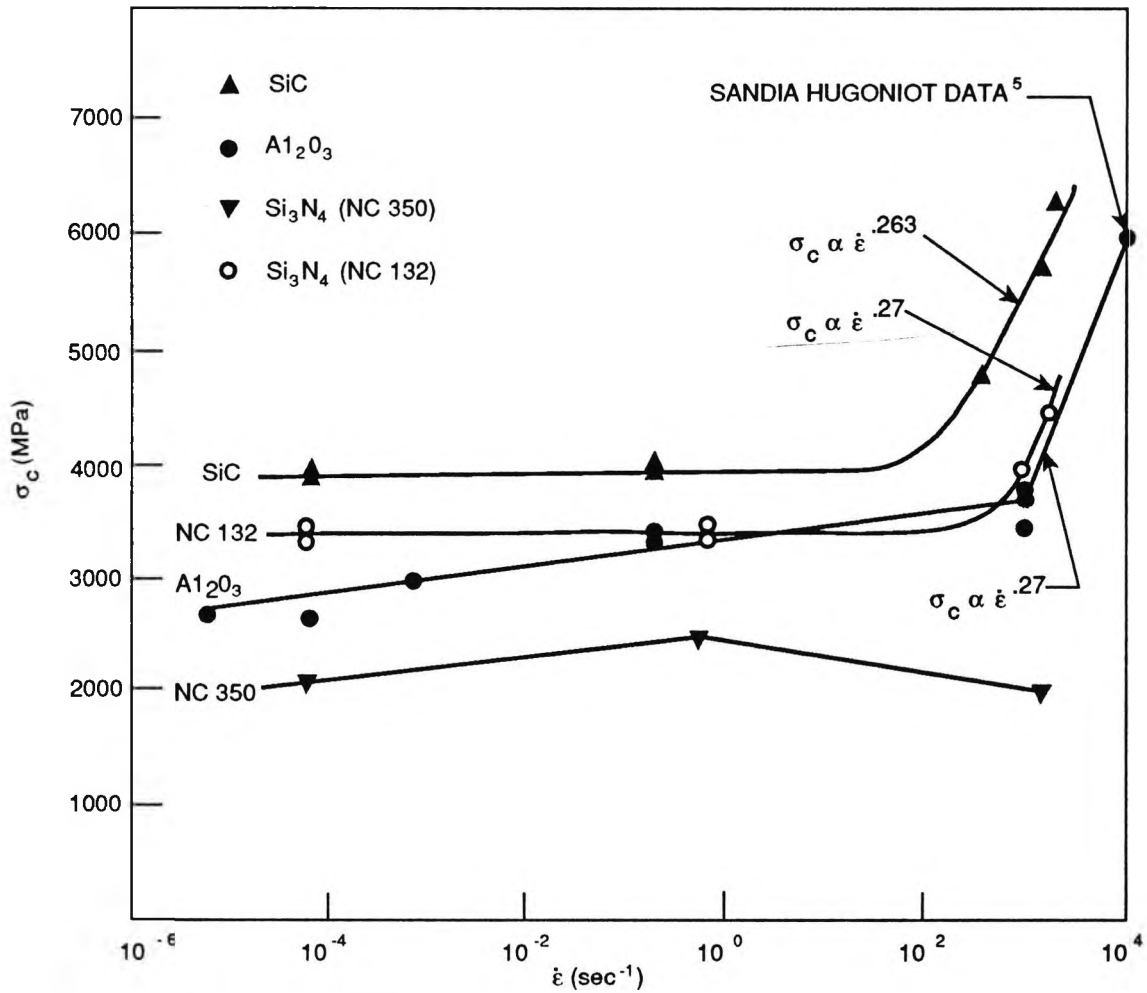

COMPRESSIVE STRENGTH VERSUS STRAIN RATE

FIG. 2. SUBCRITICAL TENSILE MICROFRACTURE PROCESSES (AFTER LANGFORD).

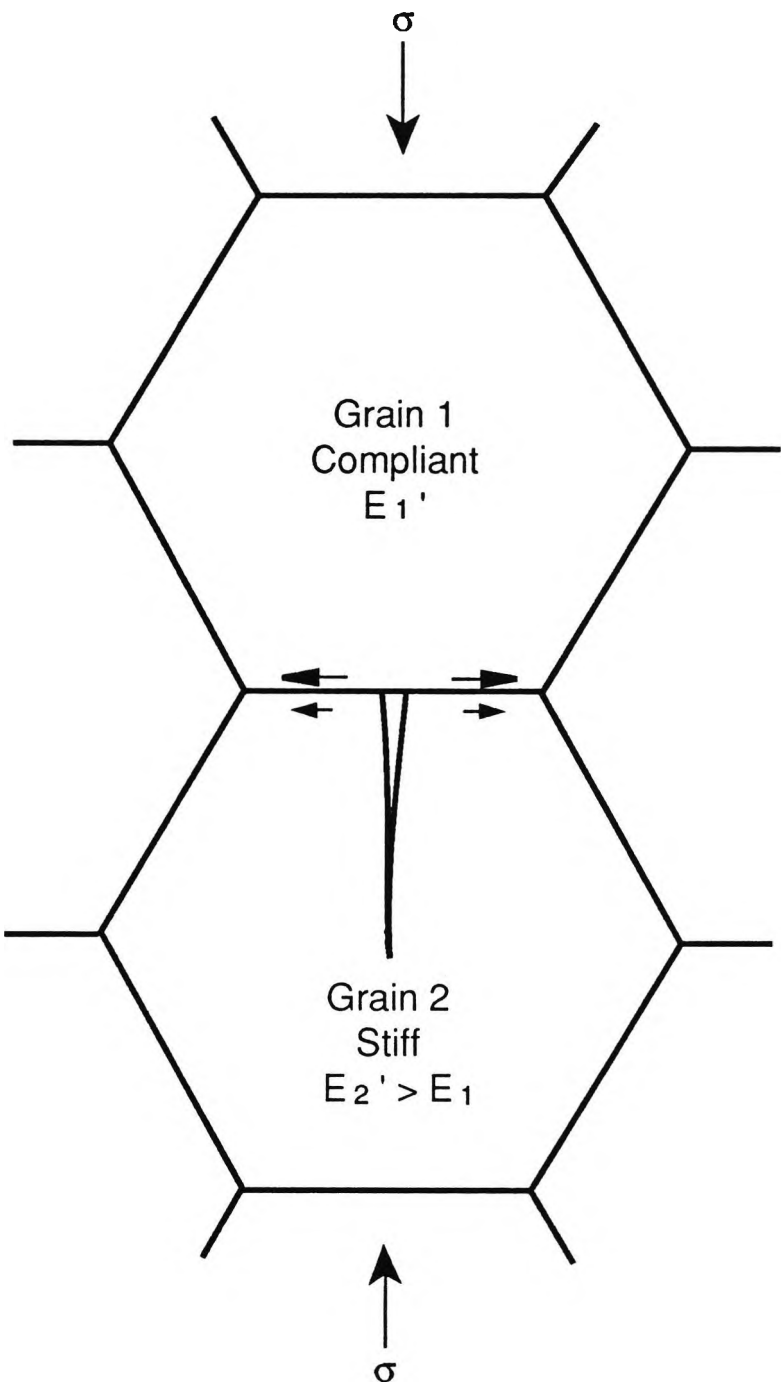

FIG. 3

Conceptual sketch of resolution of applied compressive stress into local tensile stress normal to plane of axial microcrack. Interfacial arrows represent unequal elastic lateral displacements in the two grains, producing local tensile stress field at the interface. (After Langford).

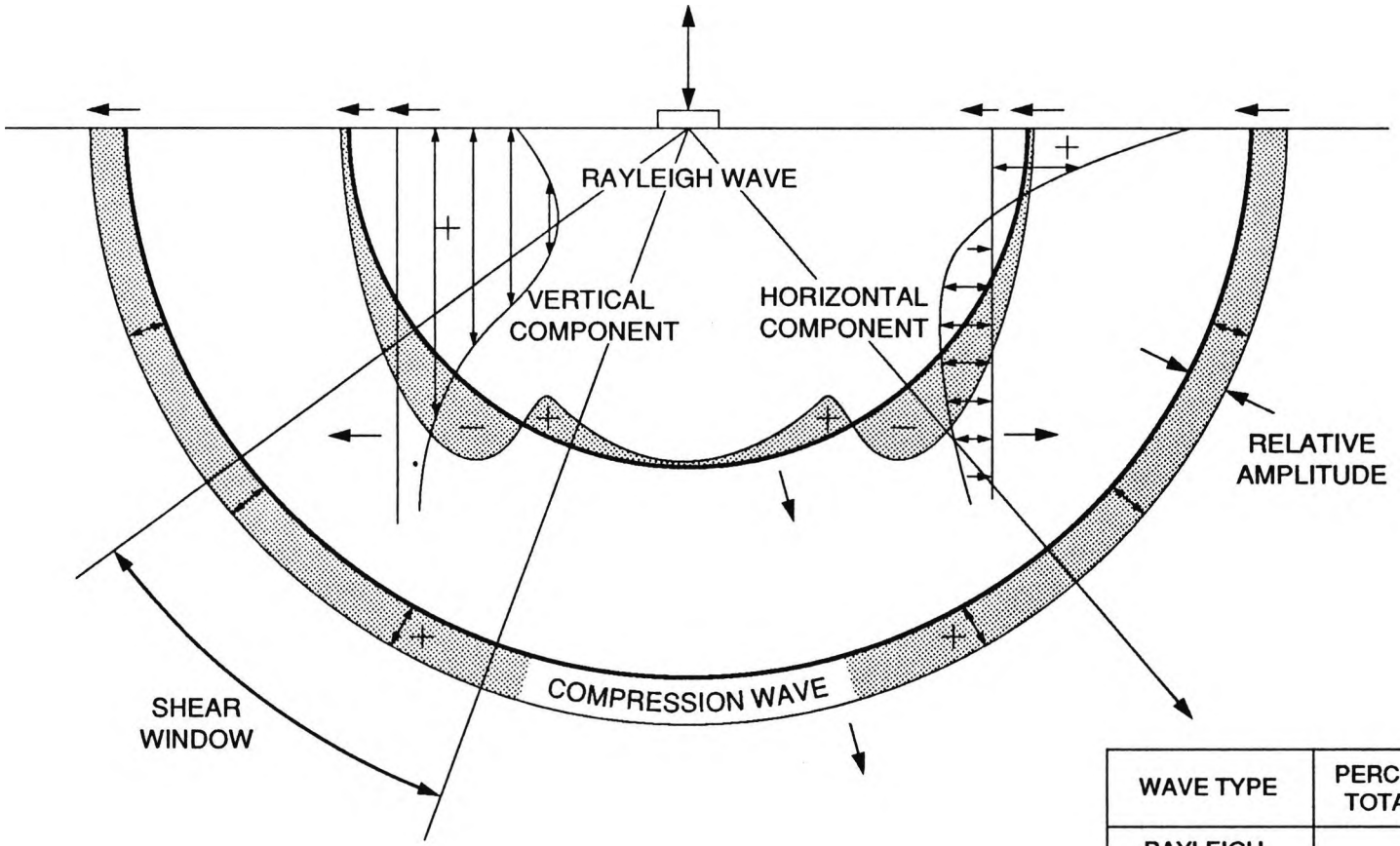

WAVE TYPE	PERCENTAGE OF TOTAL ENERGY
RAYLEIGH	67
SHEAR	26
COMPRESSION	7

FIG.4. STRUCTURE OF WAVES WITHIN A SEMI-INFINITE SOLID (AFTER WOODS).

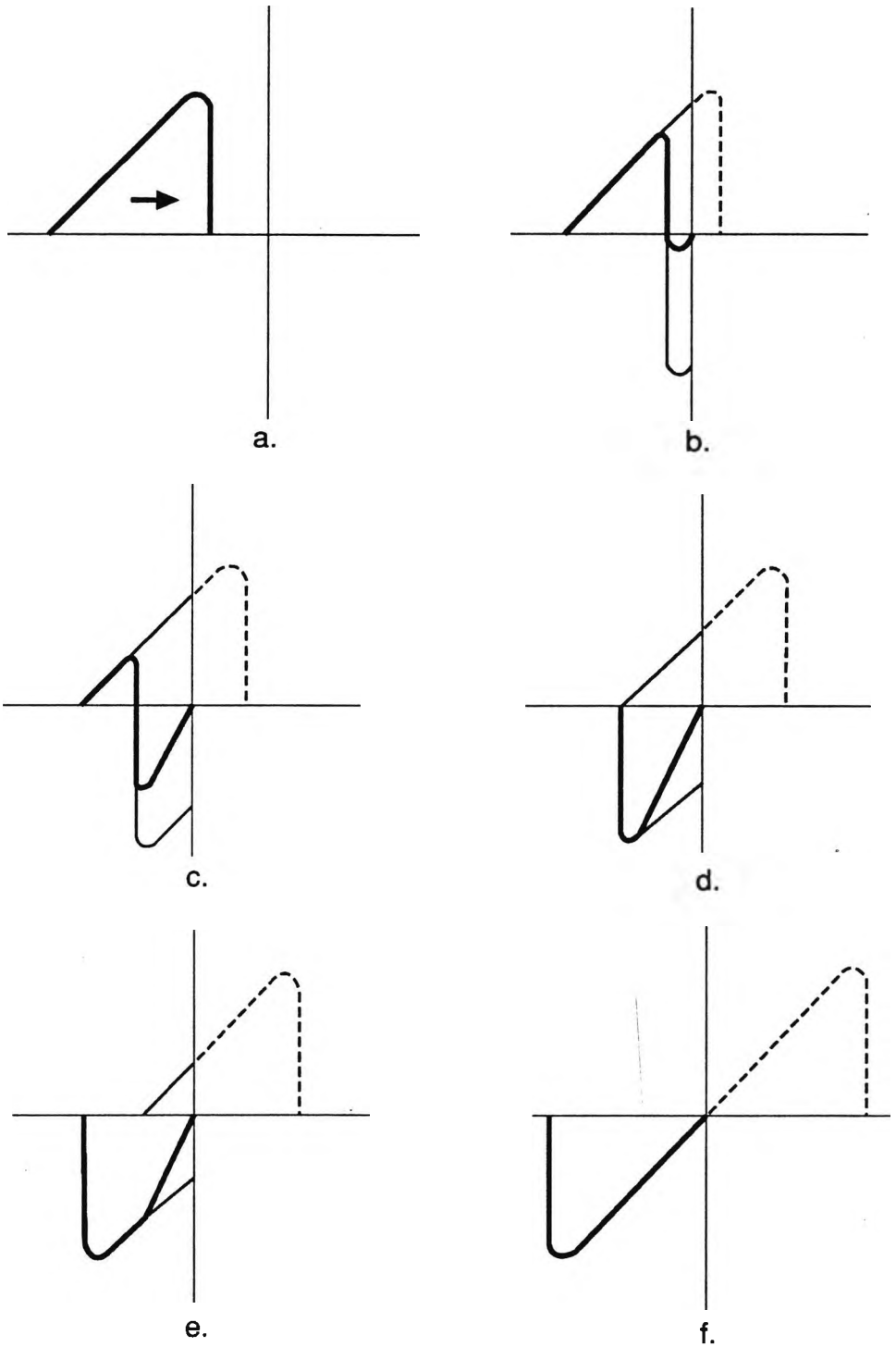

FIG.5.
REFLECTION OF PRESSURE PULSE WITH STEEP FRONT.
(AFTER KOLSKY)

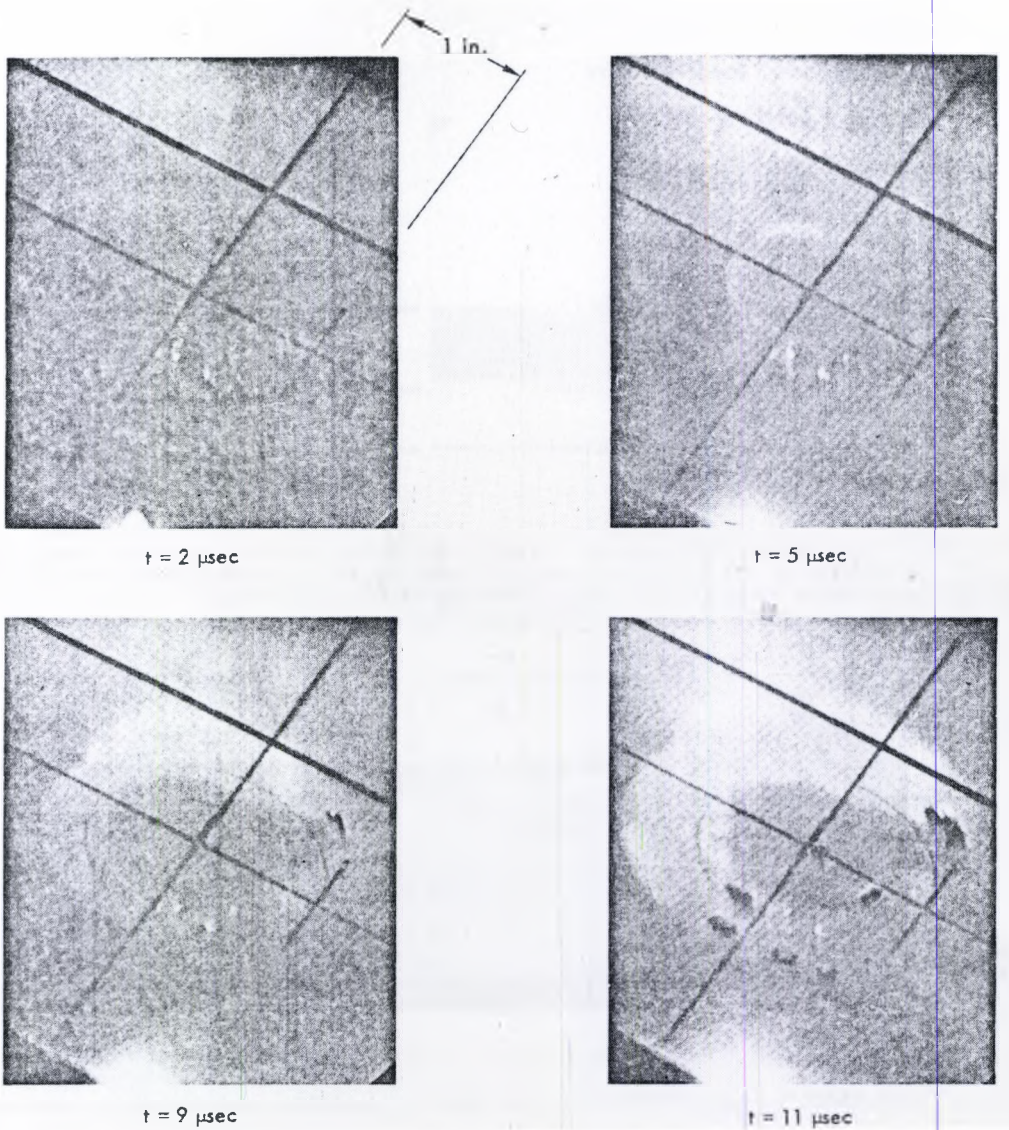

FIG. 6. EXPERIMENTAL BREAKOUT OF THE FRACTURE CONOID IN Al_2O_3 CERAMIC WITH A GLASS BACKUP PLATE. (AFTER WILKINS).

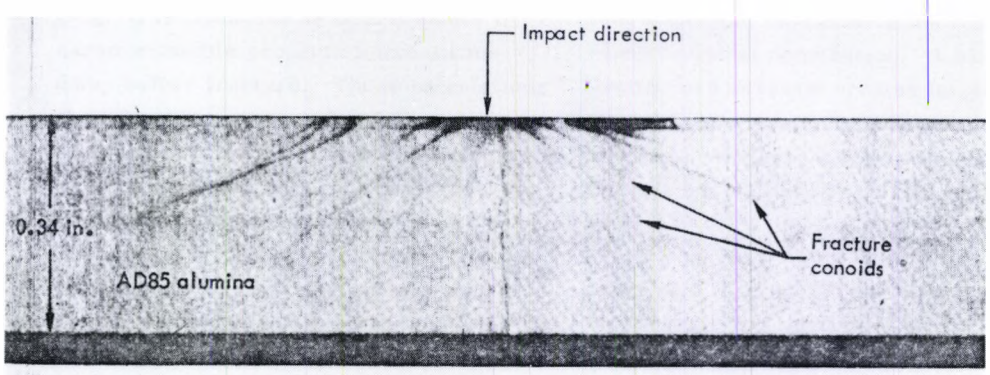

FIG. 7. SECTION VIEW OF RIGID CERAMIC STRUCK BY A SHARP STEEL PROJECTILE AT 2300 ft/sec. (AFTER WILKINS).

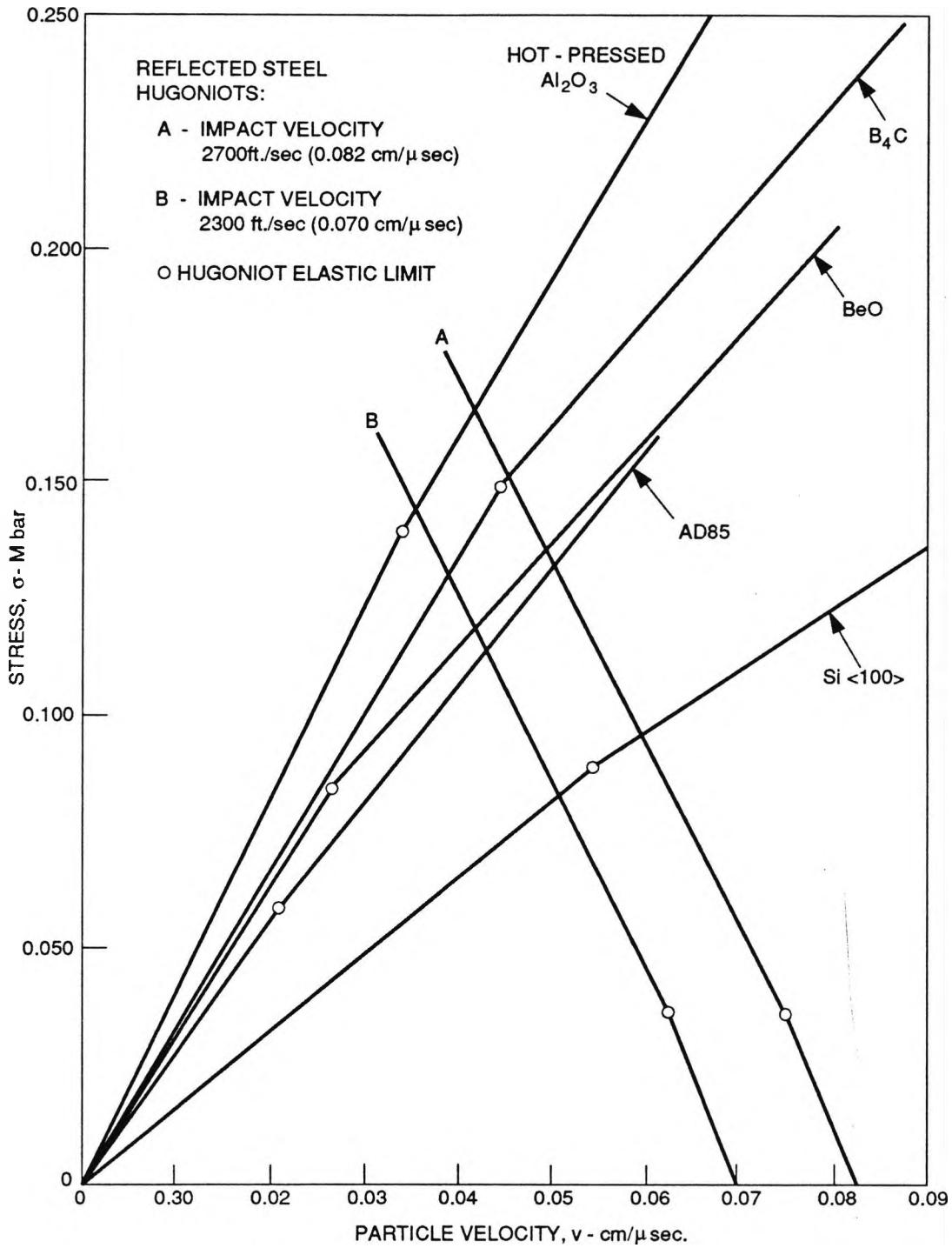

FIG. 8. ONE-DIMENSIONAL STRAIN IMPACTS OF STEEL ON CERAMICS (AFTER WILKINS).

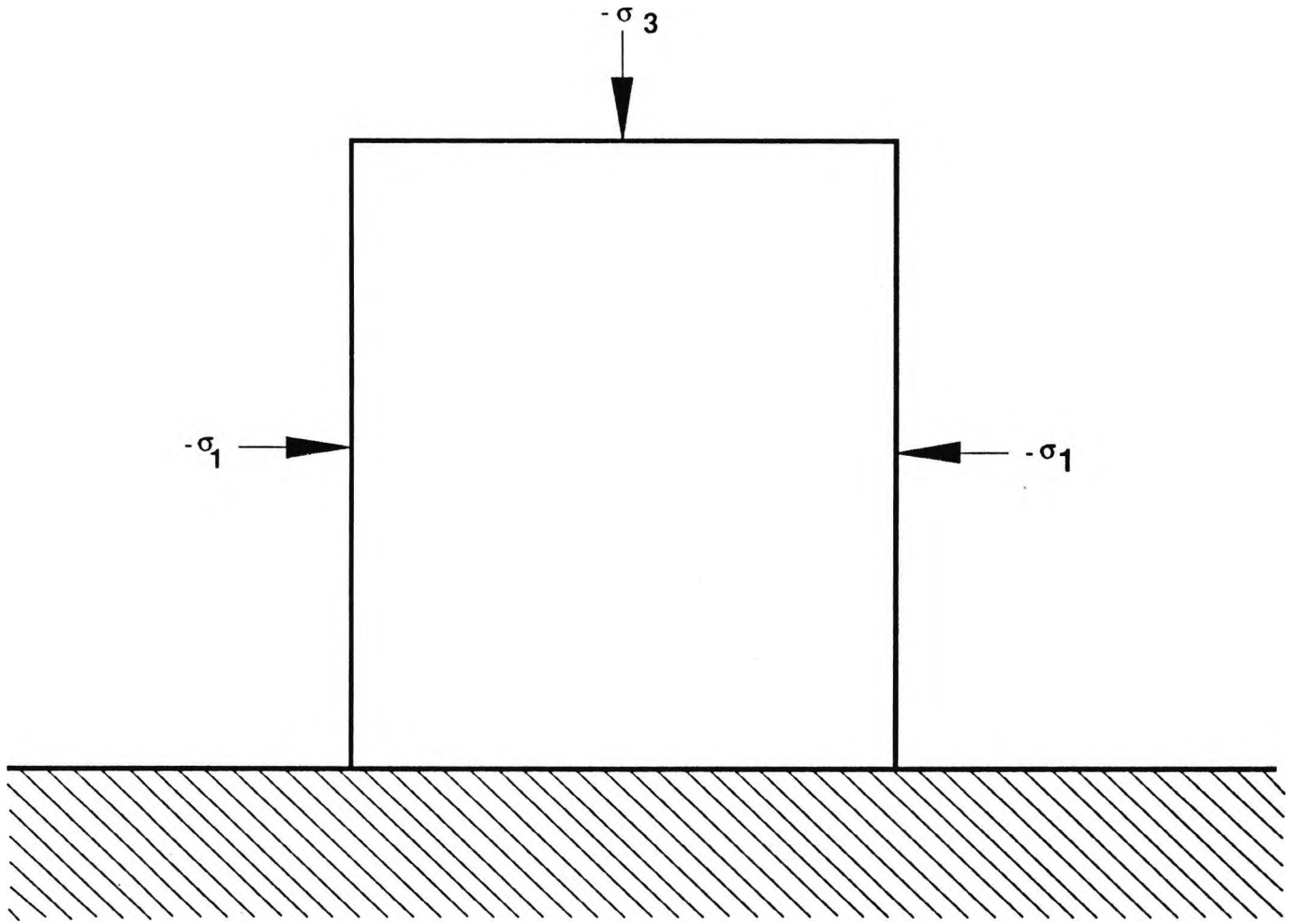

FIG. 9. SCHEMATIC OF EXPERIMENTAL STRESS CONFIGURATION (AFTER WILKINS).

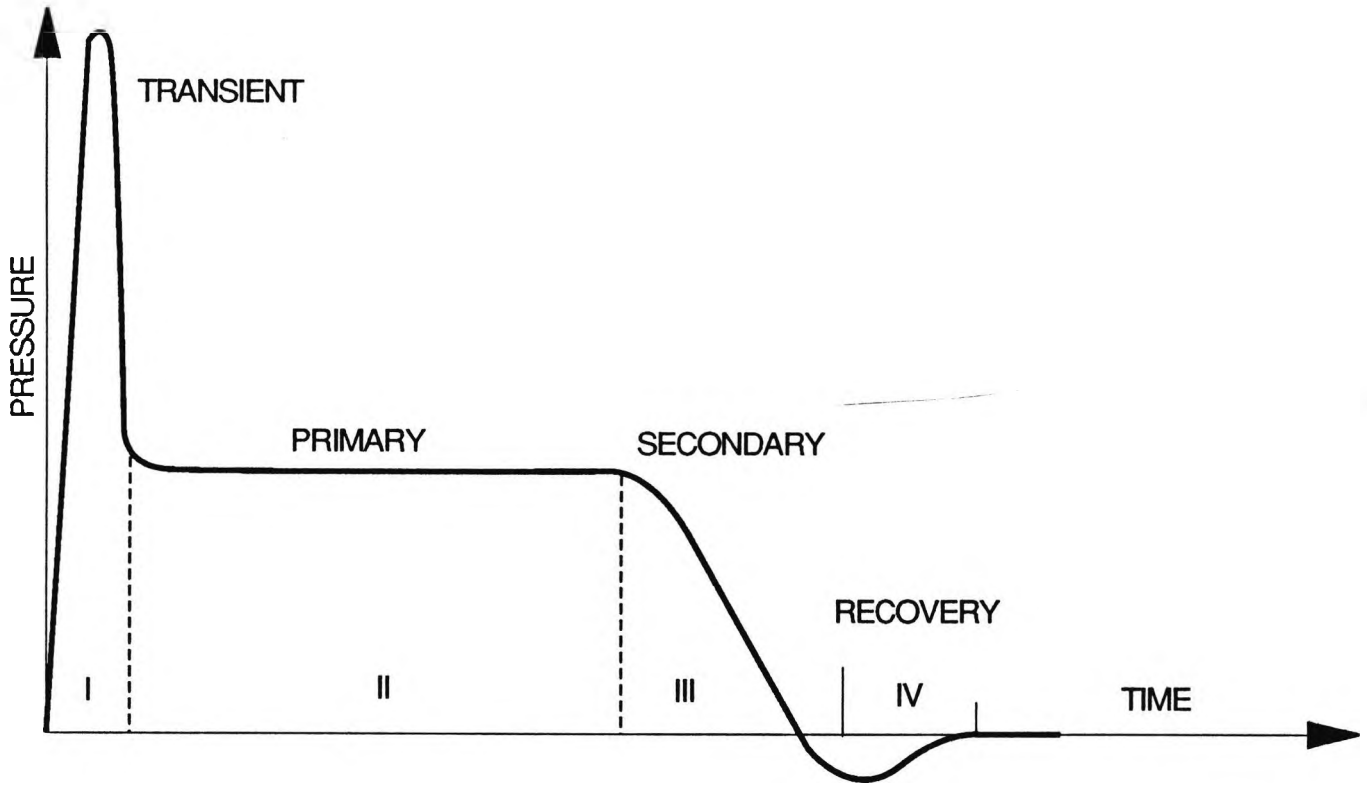

FIG. 10. SCHEMATIC PRESSURE-TIME PRESENTATION OF THE FOUR PHASES OF HIGH VELOCITY PENETRATION (AFTER HOHLER & STILP).

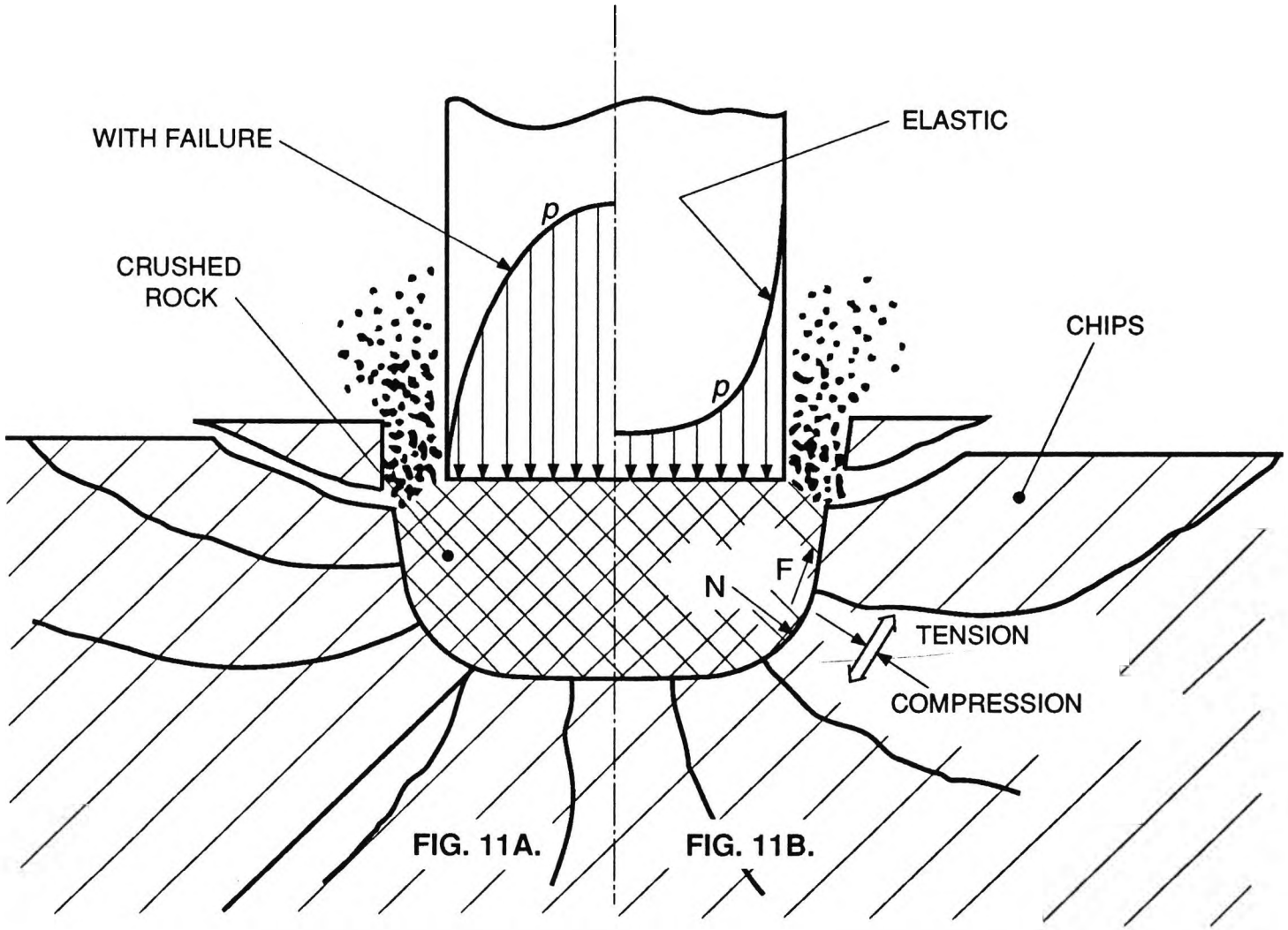

CRATER - FORMING PROCESS (AFTER JANACH).

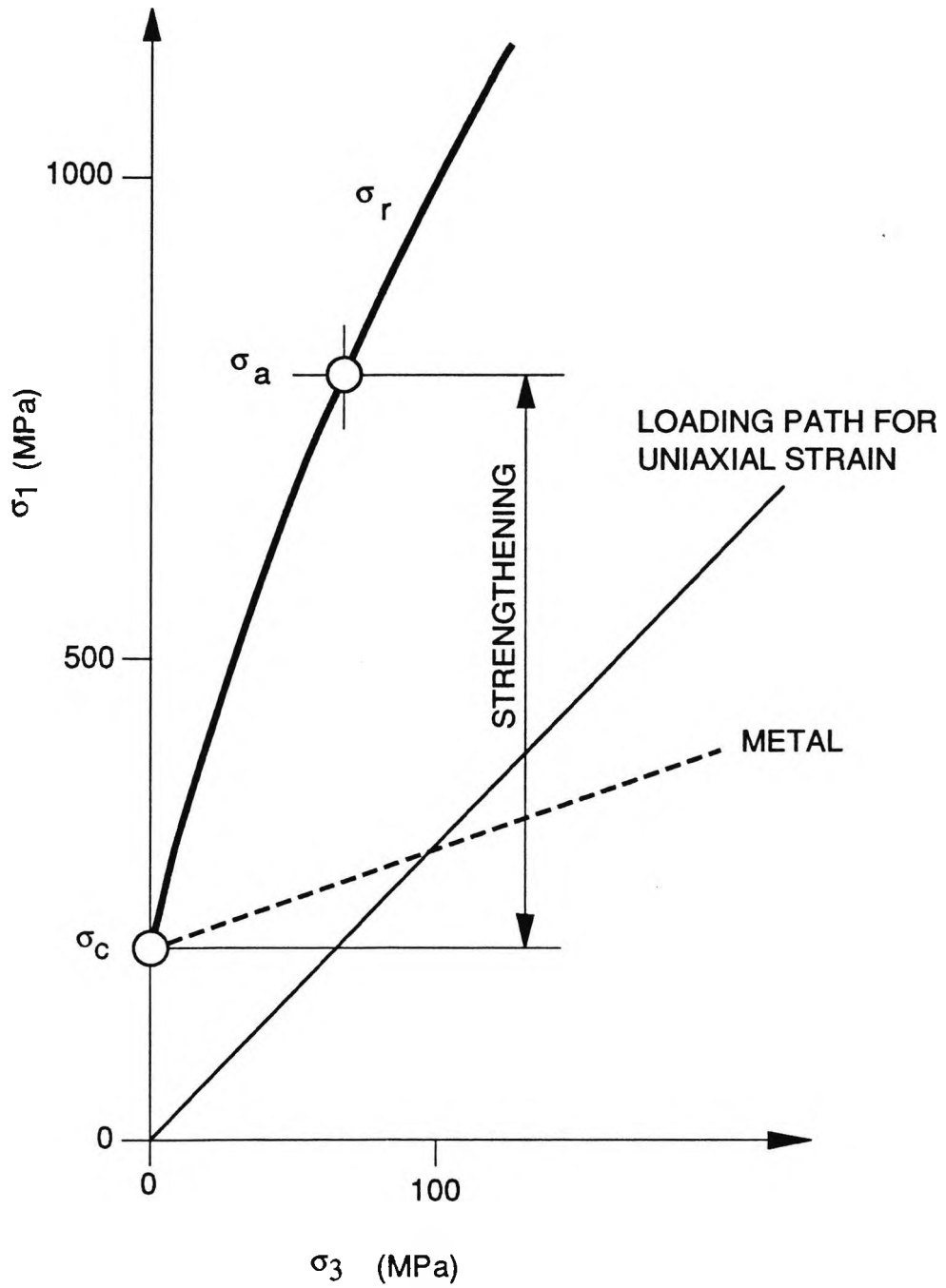

FIG.12. FAILURE ENVELOPE FOR GRANITE UNDER TRIAXIAL COMPRESSION (AFTER JANACH).

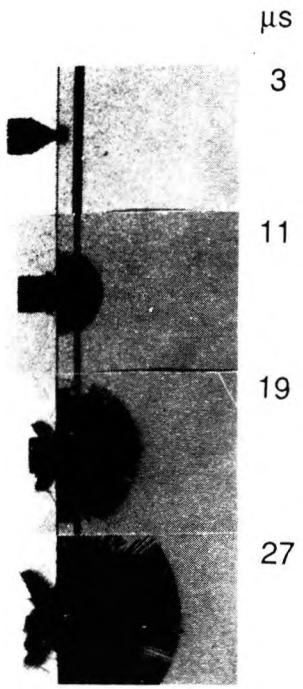

FIG.13.

v_p = 548 m/s
Conically - nosed

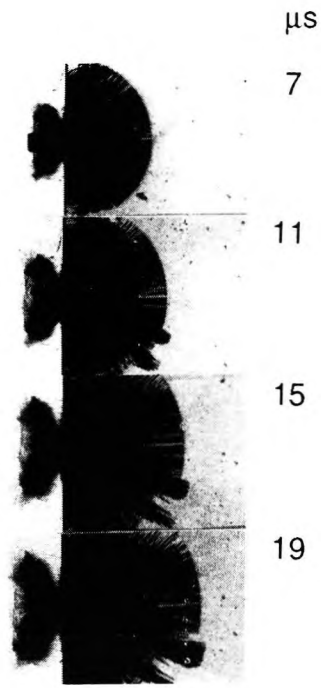

FIG. 14.

v_p = 825 m/s
Conically - nosed

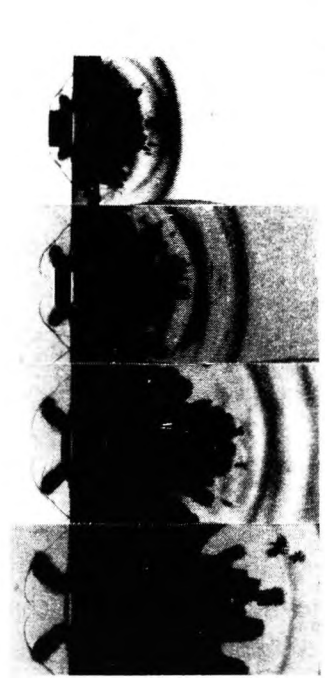

FIG. 15.

v_p = 785 m/s
Blunt

DAMAGE DEVELOPMENT AT DIFFERENT IMPACT VELOCITIES AND FOR DIFFERENT SHAPES OF THE PROJECTILE. (AFTER HORNEMANN).

FIG.16

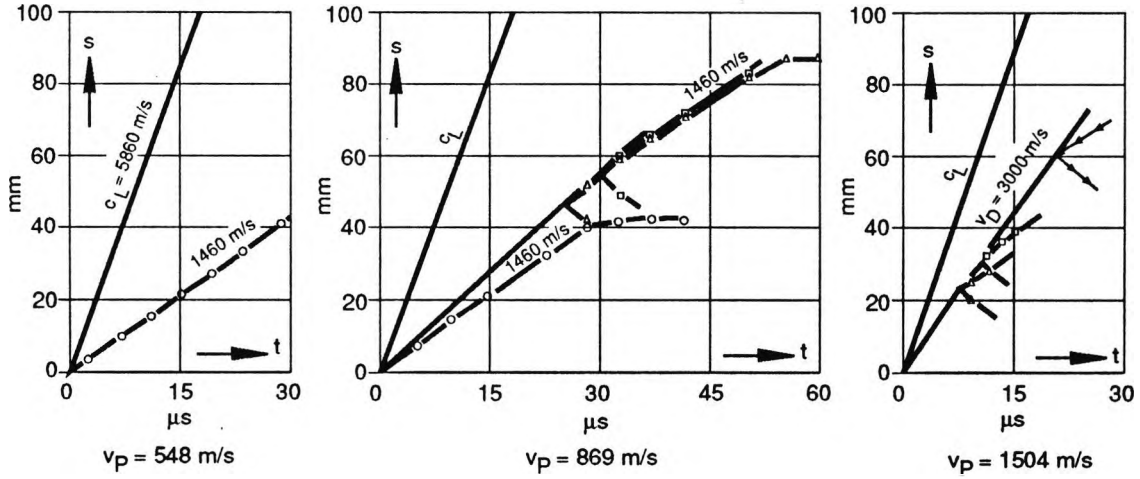

FIG.17

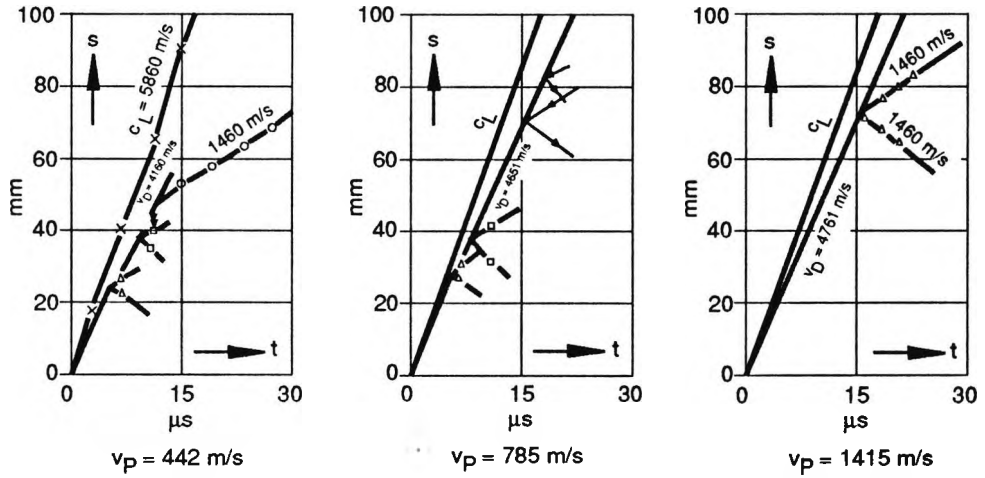

WAVE AND CRACK PROPAGATION IN GLASS TARGETS FOR DIFFERENT IMPACT VELOCITIES (HORIZONTAL DIRECTION)AND SHAPE OF IMPACTOR (VERTICAL DIRECTION). (AFTER HORNEMANN).

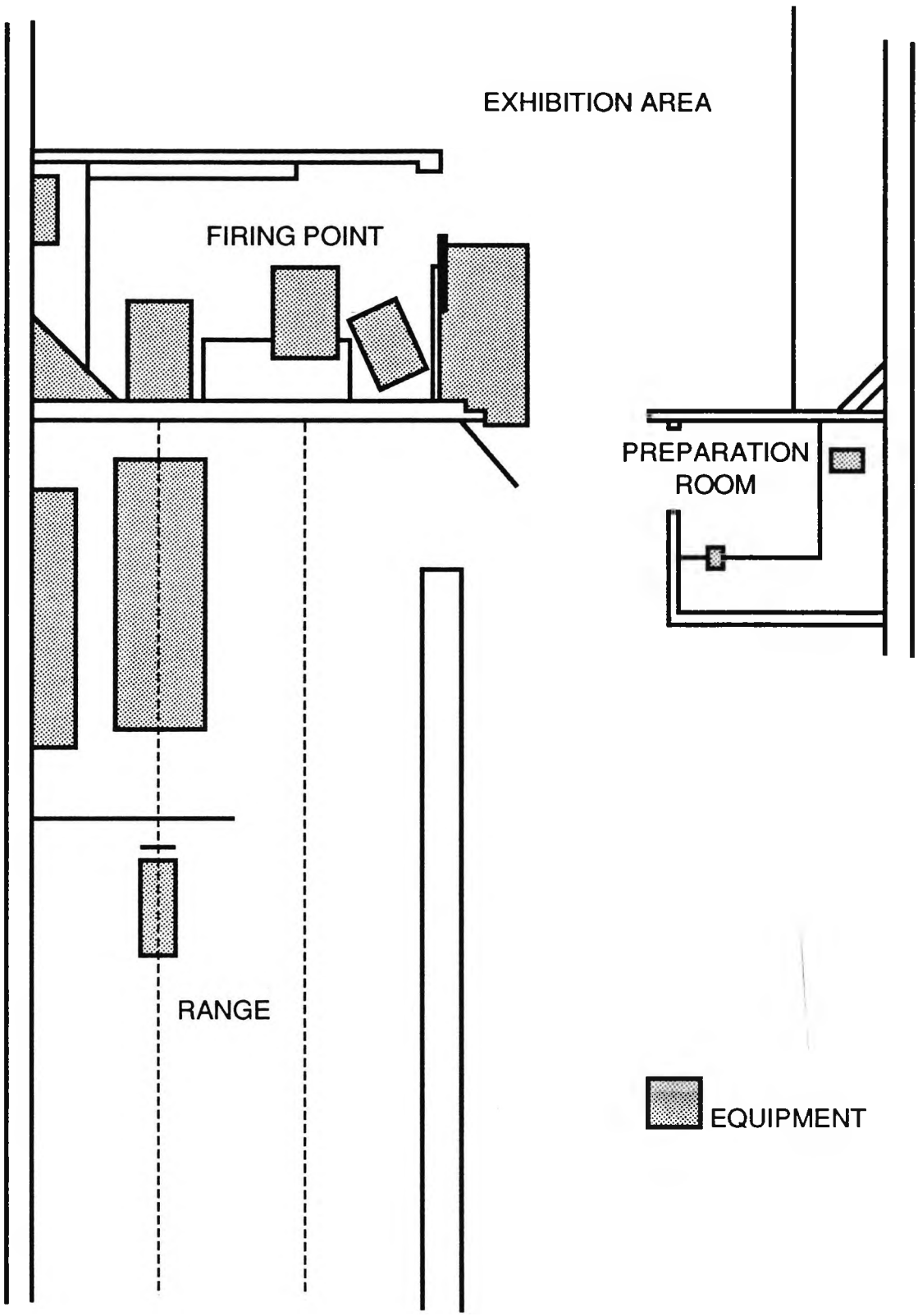

FIG. 18 PLAN OF BALLISTIC TEST FACILITY.

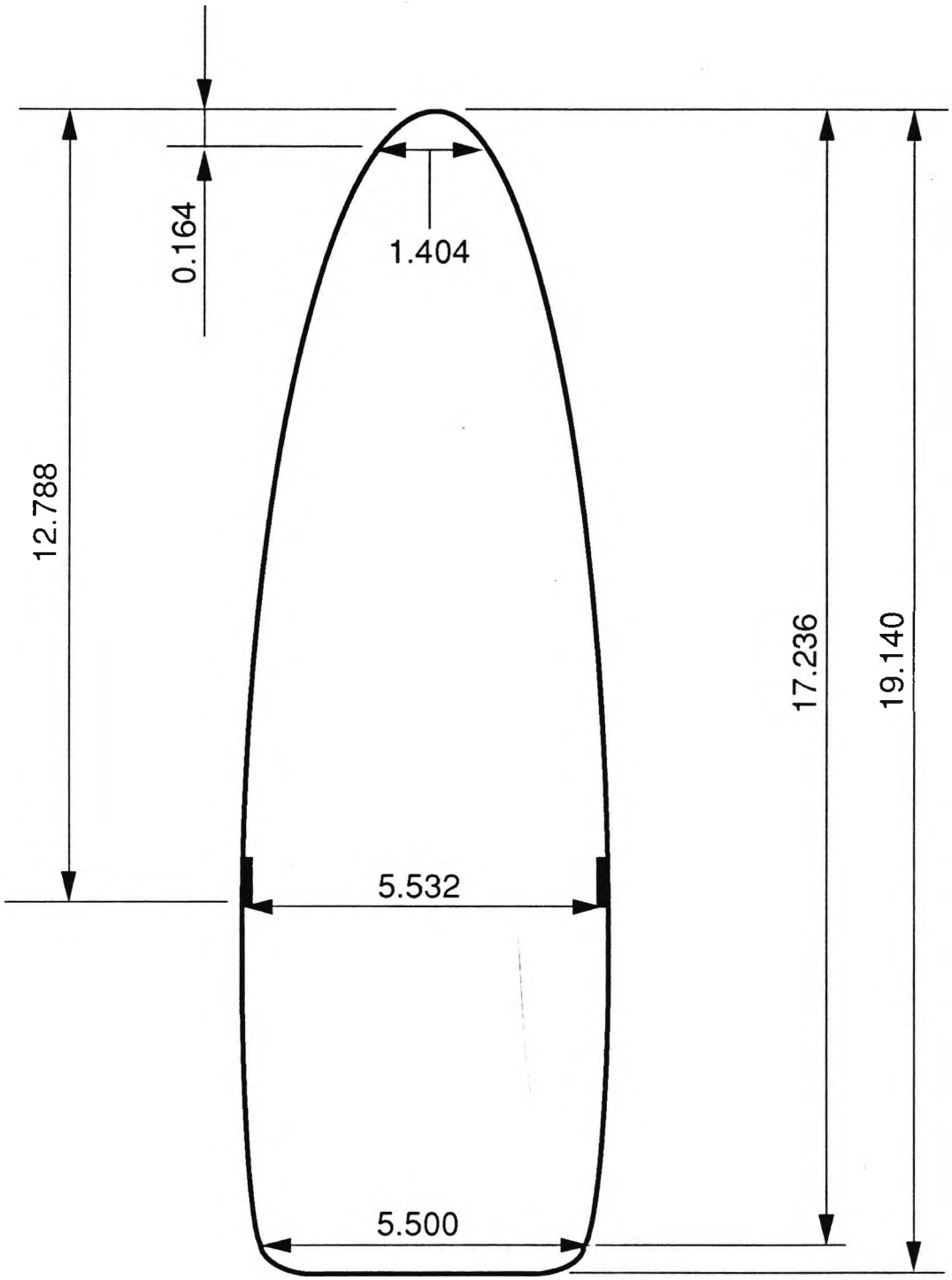

FIG. 19. MAJOR LANDMARKS ON BULLET (mm).

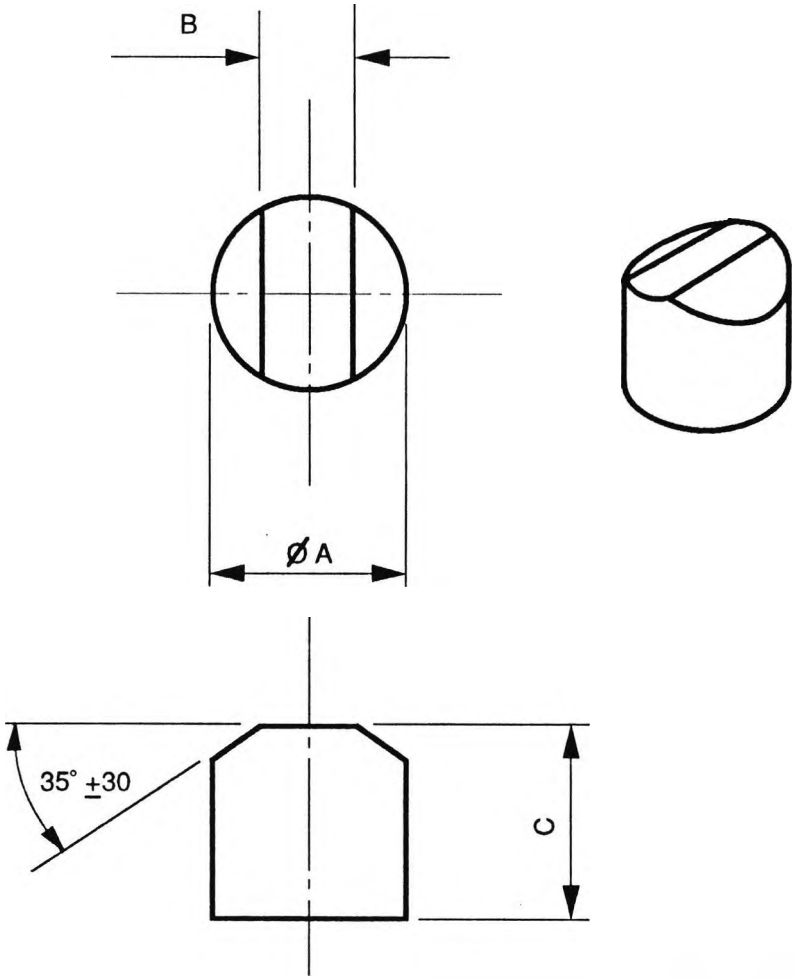

NOTES.

1. AFTER MANUFACTURE ITEM SHALL HAVE A HARDNESS VALUE OF HRC 30 ± 5.
2. ADJUST DIMENSION C TO GIVE CORRECT WEIGHT.

IDENTITY	WEIGHT	DIM. A ± 0.02	DIM. B $^{+0.0}_{-0.5}$	DIM. C SEE NOTE 2
A3/6723/1	1.102g ± 0.02	5.385	2.54	6.350
A3/6723/2	0.162g ± 0.01	2.642	1.27	3.175
A3/6723/3	0.237g ± 0.02	3.251	1.52	3.810
A3/6723/4	0.486g ± 0.02	4.064	2.03	4.572
A3/6723/5	2.786g ± 0.02	7.493	3.18	8.763
A3/6723/6	0.325g ± 0.01	3.600	1.750	4.313

MATERIAL : TO B.S. 1407 HIGH CARBON BRIGHT STEEEL (SILVER STEEL)

TOLERANCES : AS STATED. FINISH : N8 TO B.S. 308 PART 2 1972

DIMENSIONS IN mm. SCALE : N.T.S.

DRG. No.A3/6723 HELD BY SCRDE DRAWING OFFICE.

FIG. 20. FRAGMENT SIMULATING PROJECTILE.

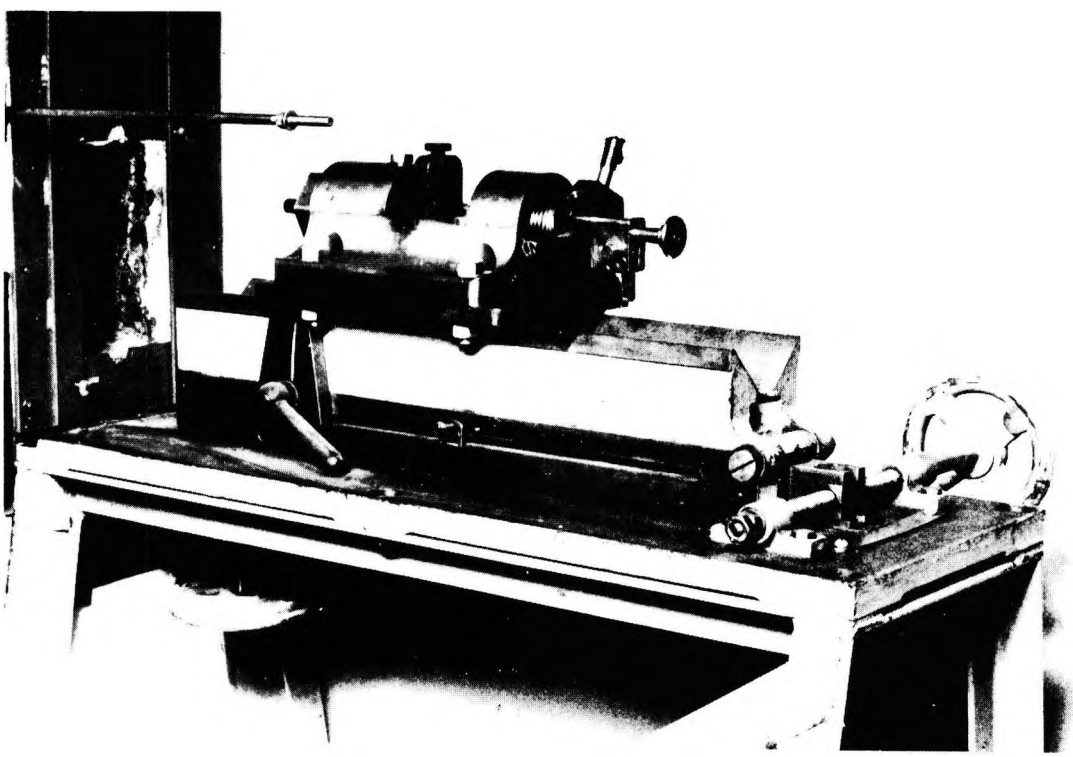

FIG. 21. PRESSURE HOUSING FOR BALLISTIC TESTING.

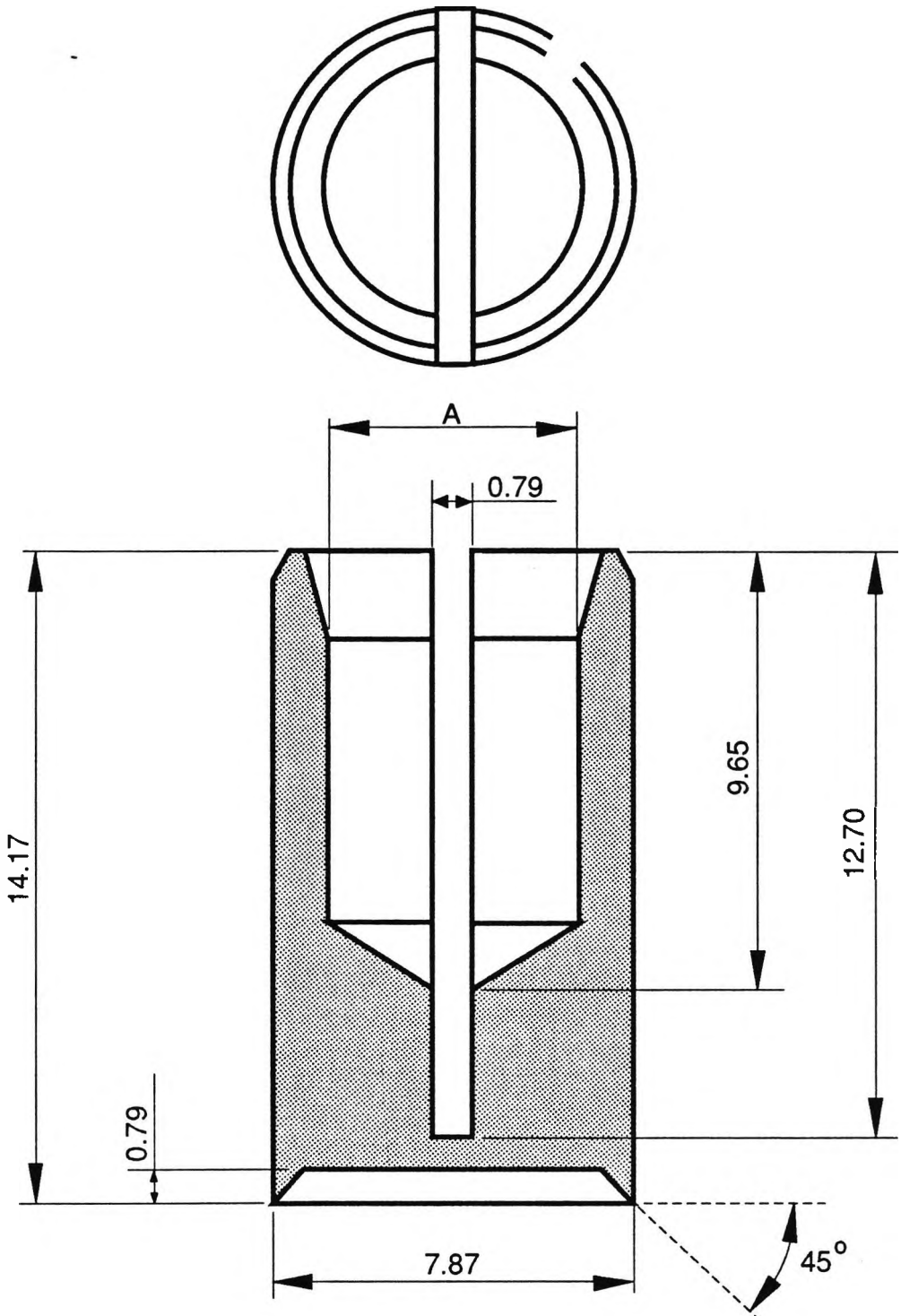

A is 2.69, 3.26, 4.09 or 5.41

DIMENSIONS IN mm.

MATERIAL : POLYPROPYLENE

FIG. 22. SABOT

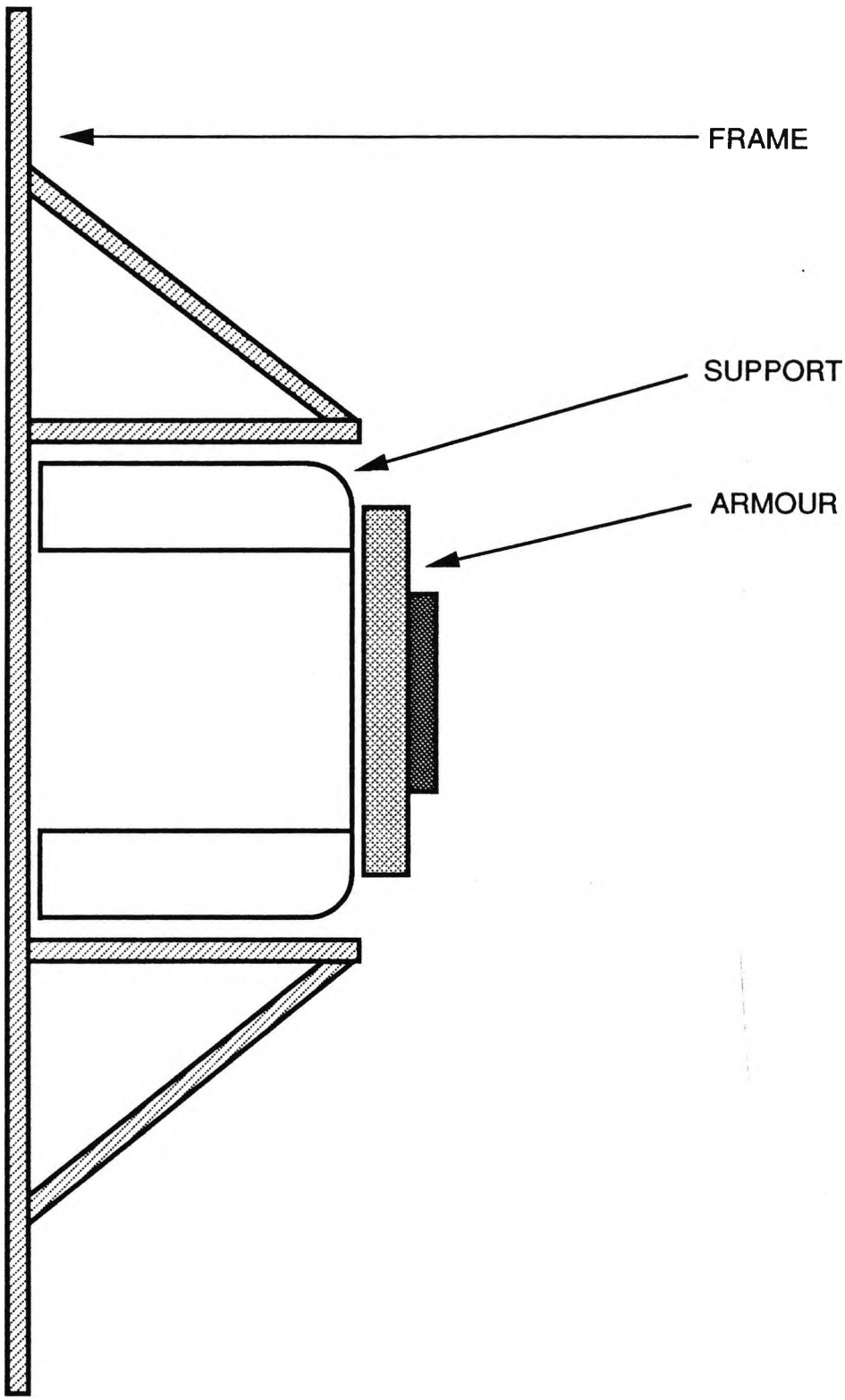

FIG. 23. FRAME FOR SUPPORT OF ARMOUR DURING X-RAY EXAMINATION.

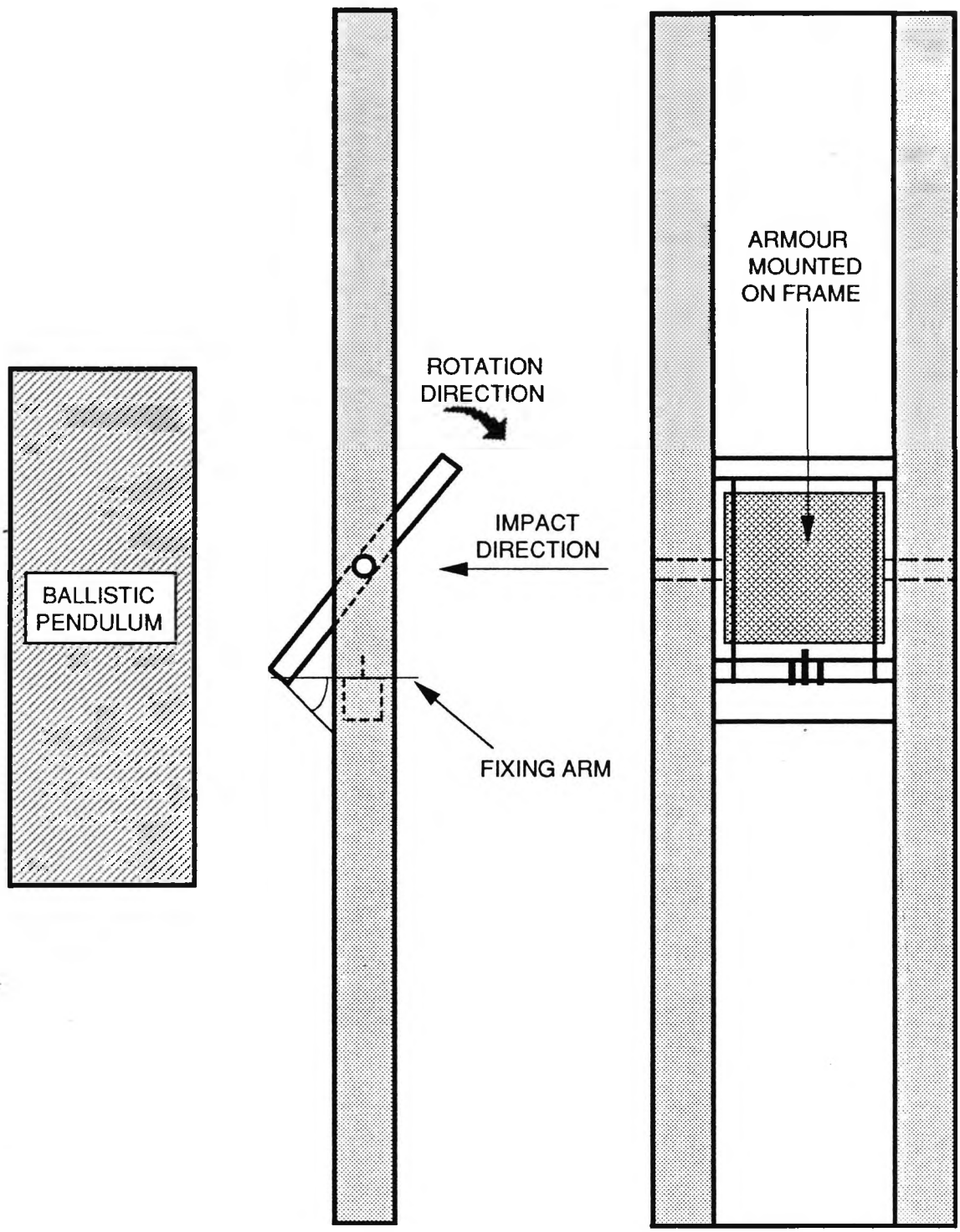

FIG. 24. FRAME FOR SUPPORT OF ARMOUR DURING TESTING AT OBLIQUE ANGLES OF ATTACK.

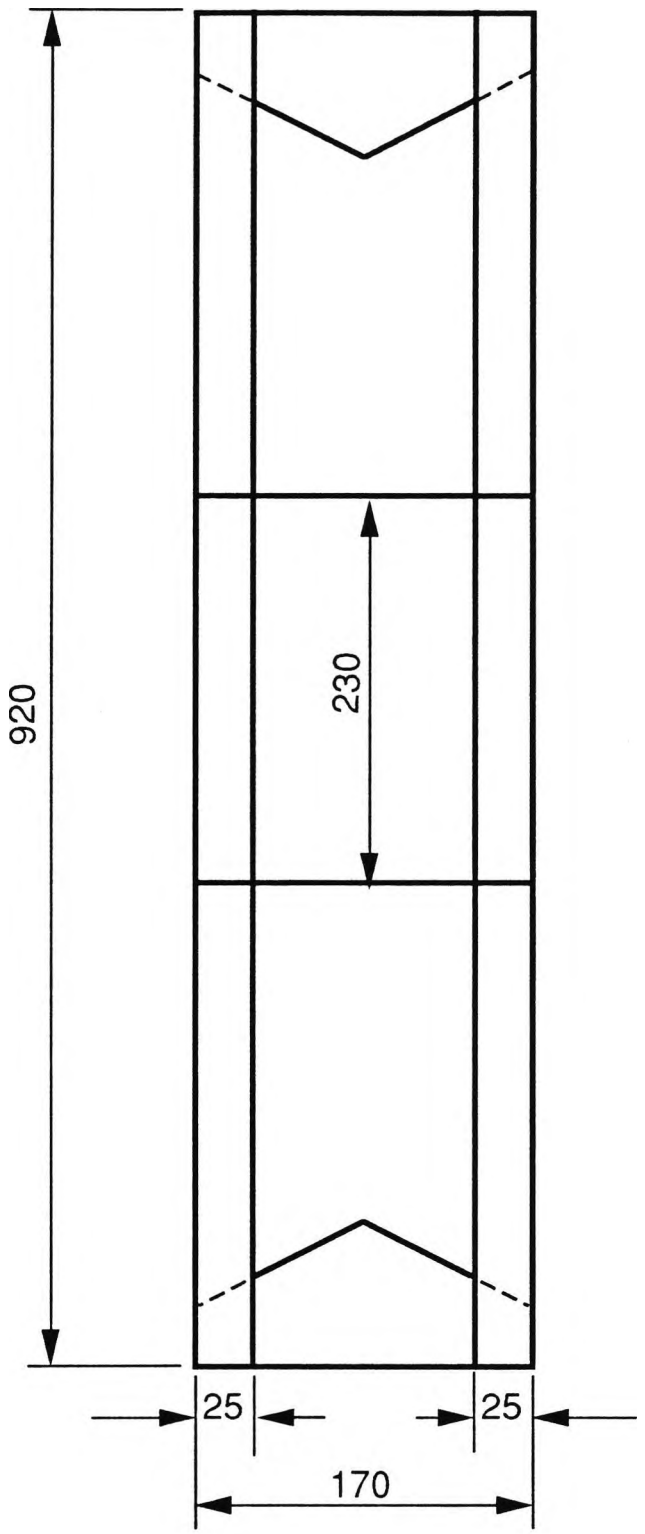

DIMENSIONS IN mm.

FIG. 25. FRAME FOR SUPPORT OF ARMOUR DURING TESTING.

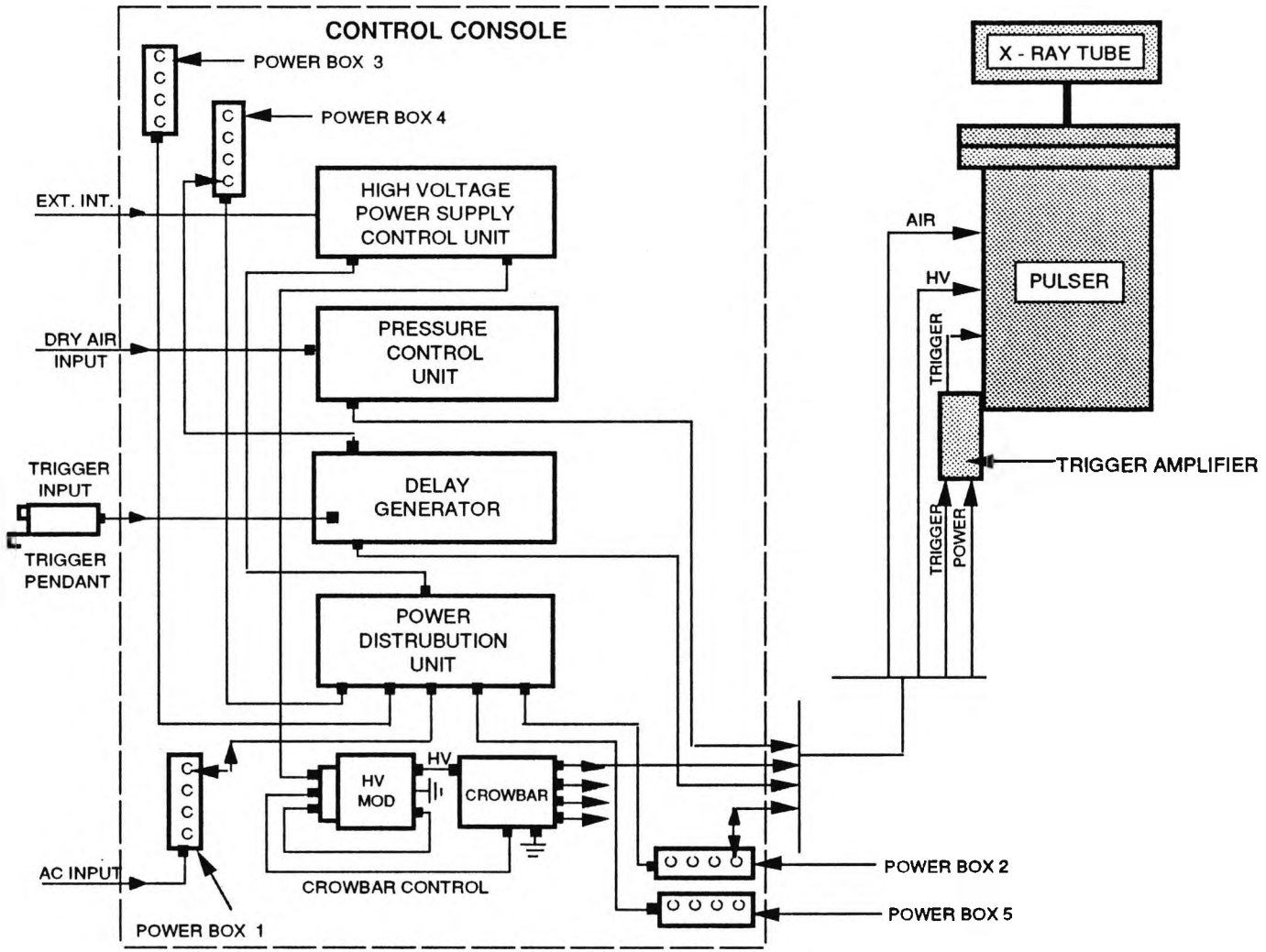

FIG. 26. X-RAY SYSTEM.

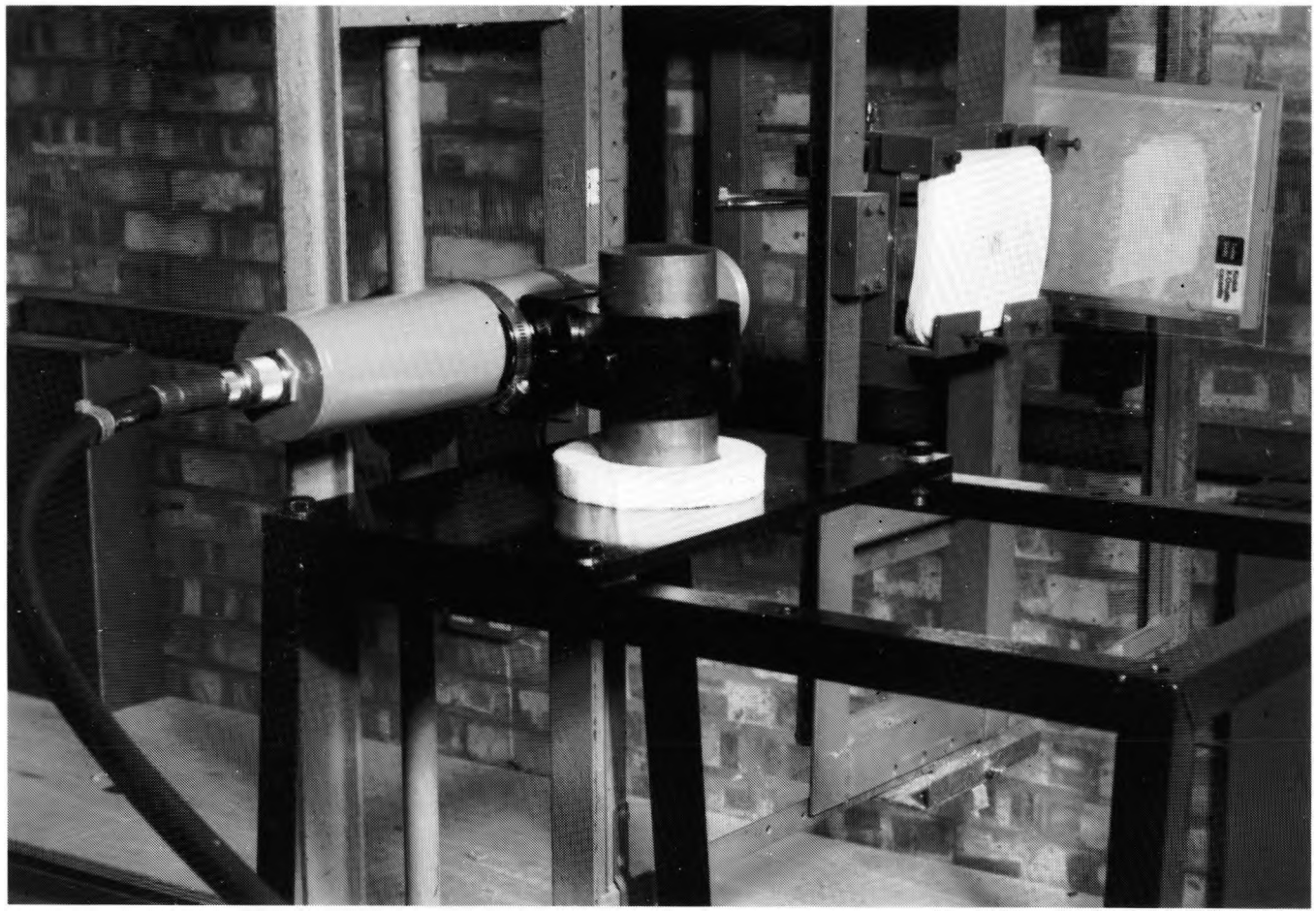

FIG. 27. SET UP FOR FLASH RADIOGRAPHY.

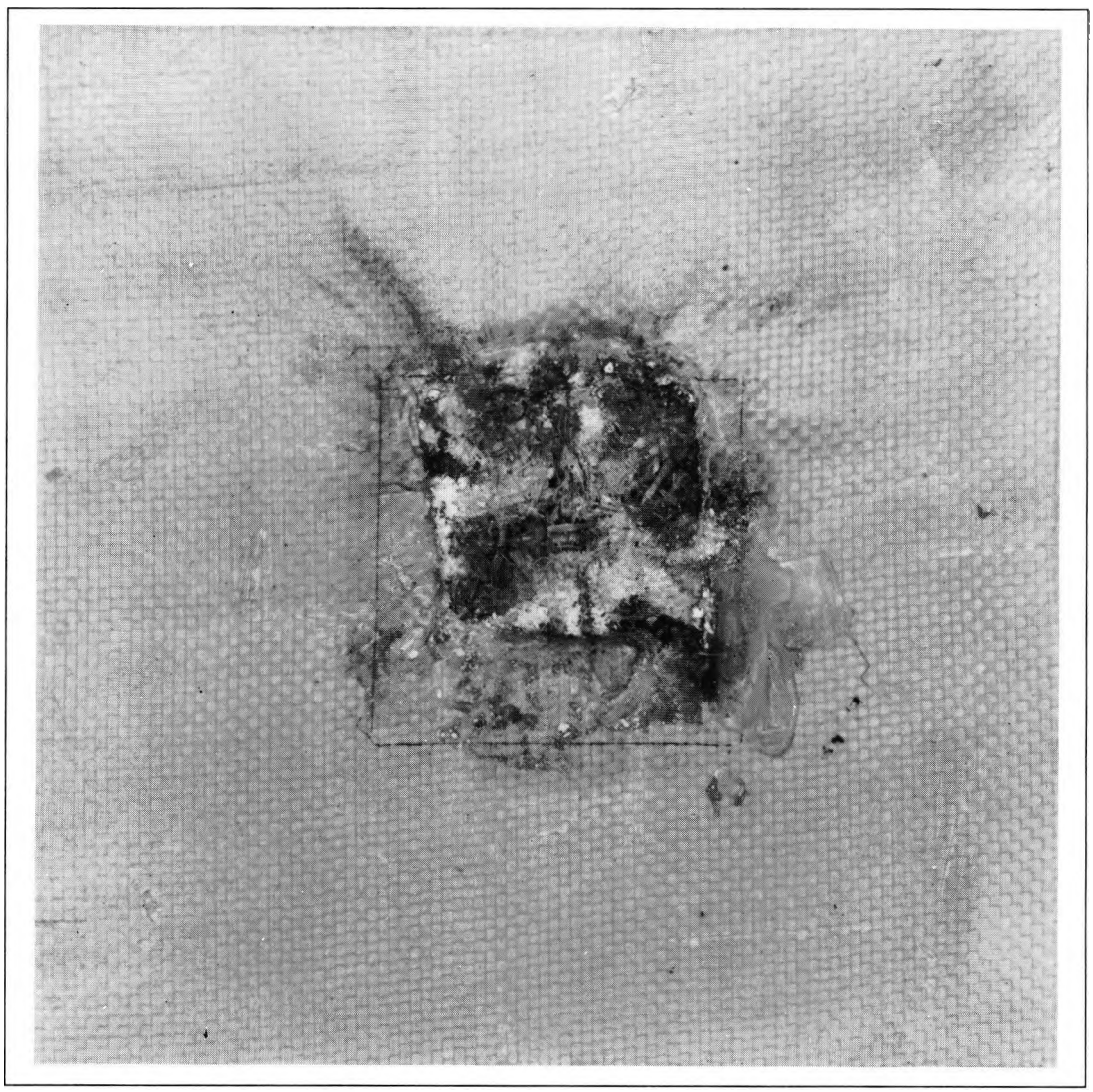

FIG. 28. FRONT VIEW OF ALUMINA FACED ARAMID LAMINATE ARMOUR AFTER PENETRATION.

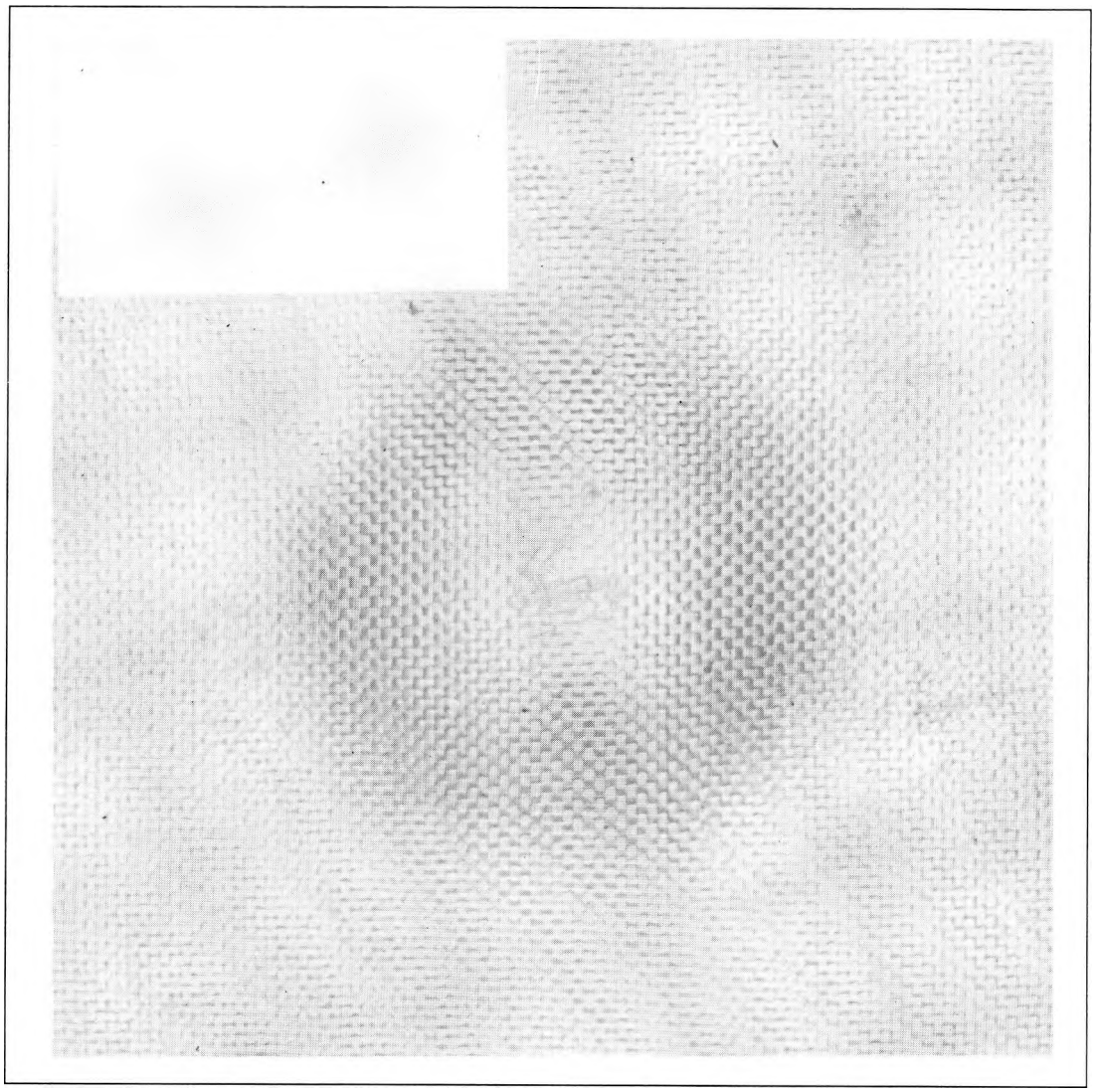

FIG. 29. REAR VIEW OF ALUMINA FACED ARAMID LAMINATE ARMOUR AFTER PENETRATION.

FIG. 30. FRONT VIEW OF ALUMINA FACED GRP LAMINATE ARMOUR AFTER PENETRATION.

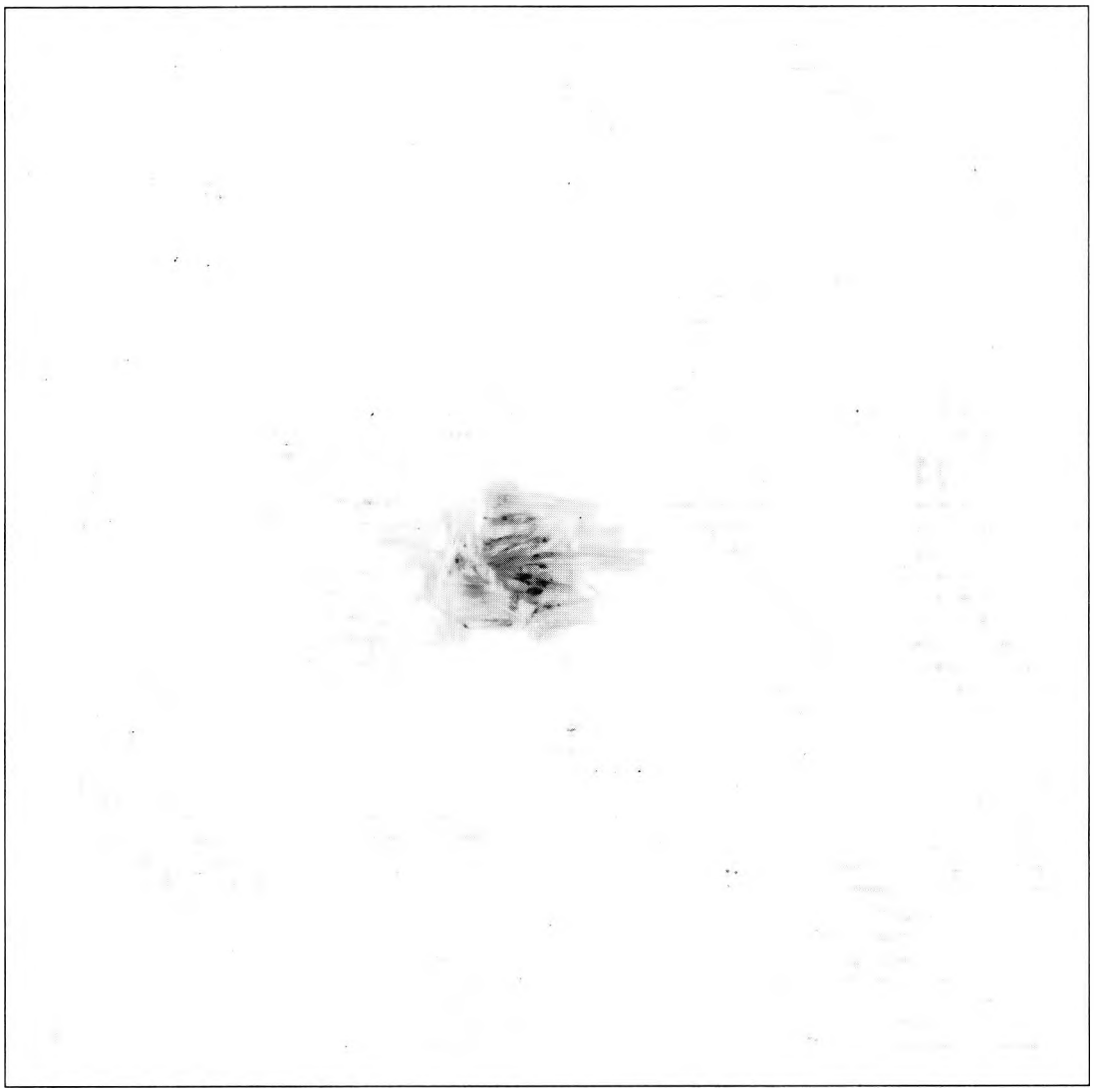

FIG. 31. REAR VIEW OF ALUMINA FACED GRP LAMINATE ARMOUR AFTER PENETRATION.

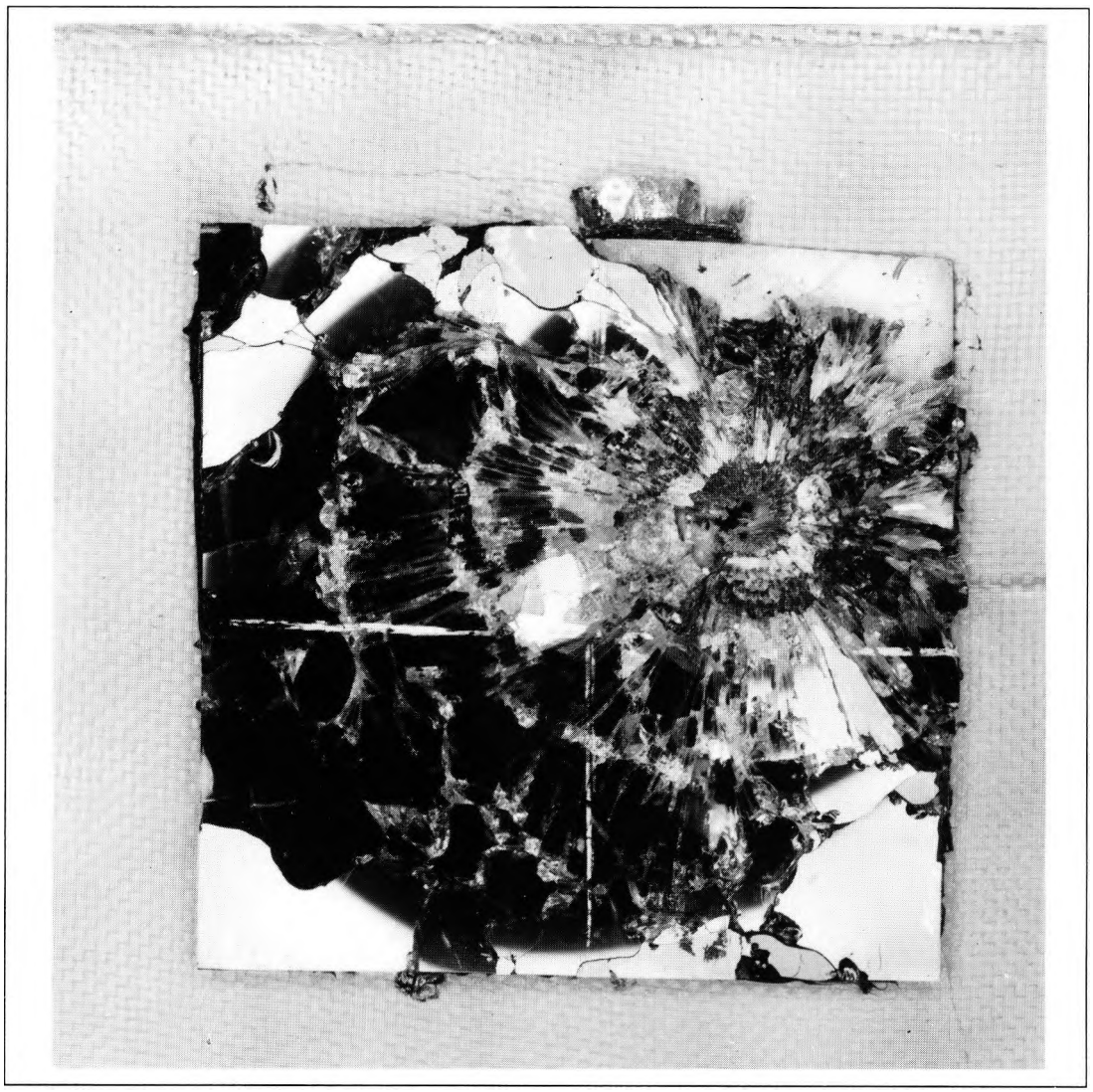

FIG. 32. FRONT VIEW OF GLASS FACED ARAMID LAMINATE ARMOUR AFTER PENETRATION.

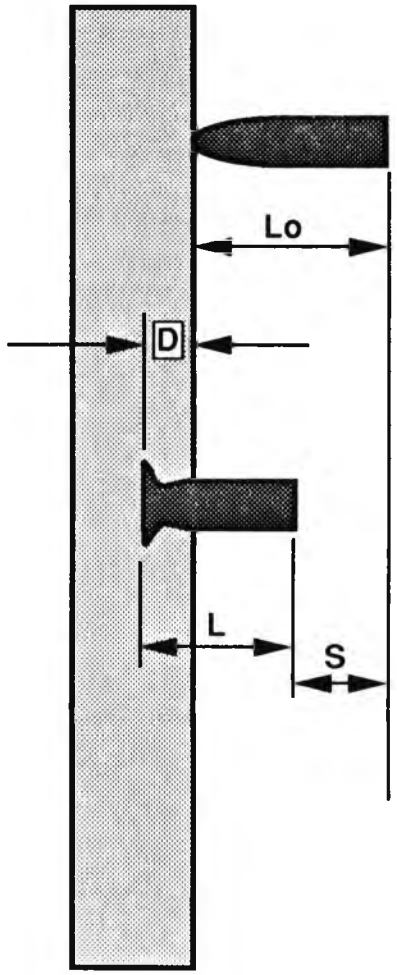

S = Displacement of bullet rear

Lo = Original length = 19mm

L = Length of Projectile

D = Penetration into ceramic

S = 19 - (L - D)

FIG. 33.
DIAGRAM SHOWING PROJECTILE EROSION

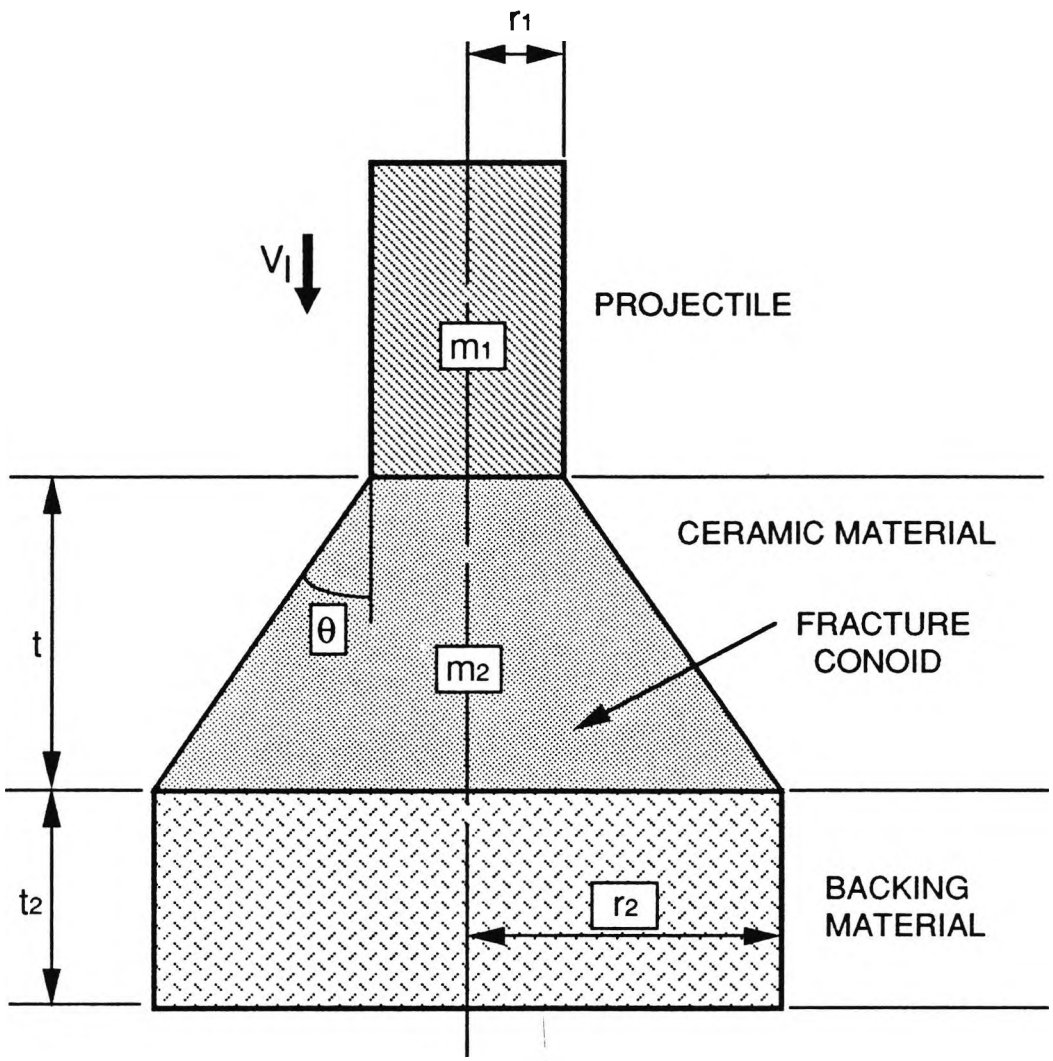

FOR A GIVEN CONOID SEMI - ANGLE θ THE AREA OVER WHICH ENERGY IS ABSORBED IS PROPORTIONAL TO THE SQUARE OF THE CERAMIC THICKNESS t_1. MATERIALS HAVING A GREATER THICKNESS FOR A GIVEN AREAL DENSITY (i.e. LOWER DENSITY) WILL BE POTENTIALLY BETTER ARMOURS

FIG. 34. SCHEMATIC DIAGRAM OF PROJECTILE IMPACT ON CERAMIC ARMOUR.

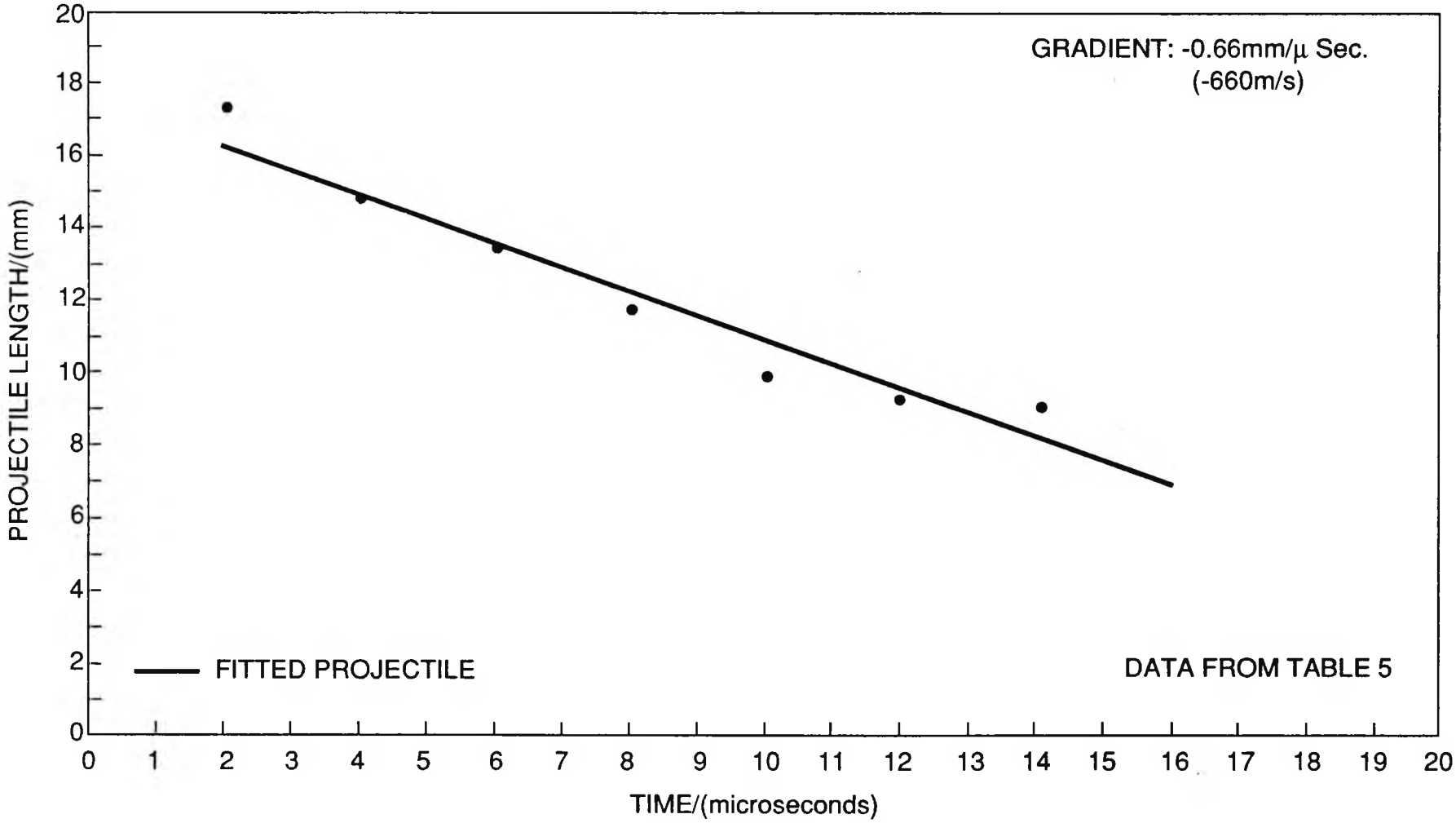

FIG. 35. EROSION OF THE BULLET AS IT PENETRATES THE ALUMINA FACING (WITH GRP BACKING).

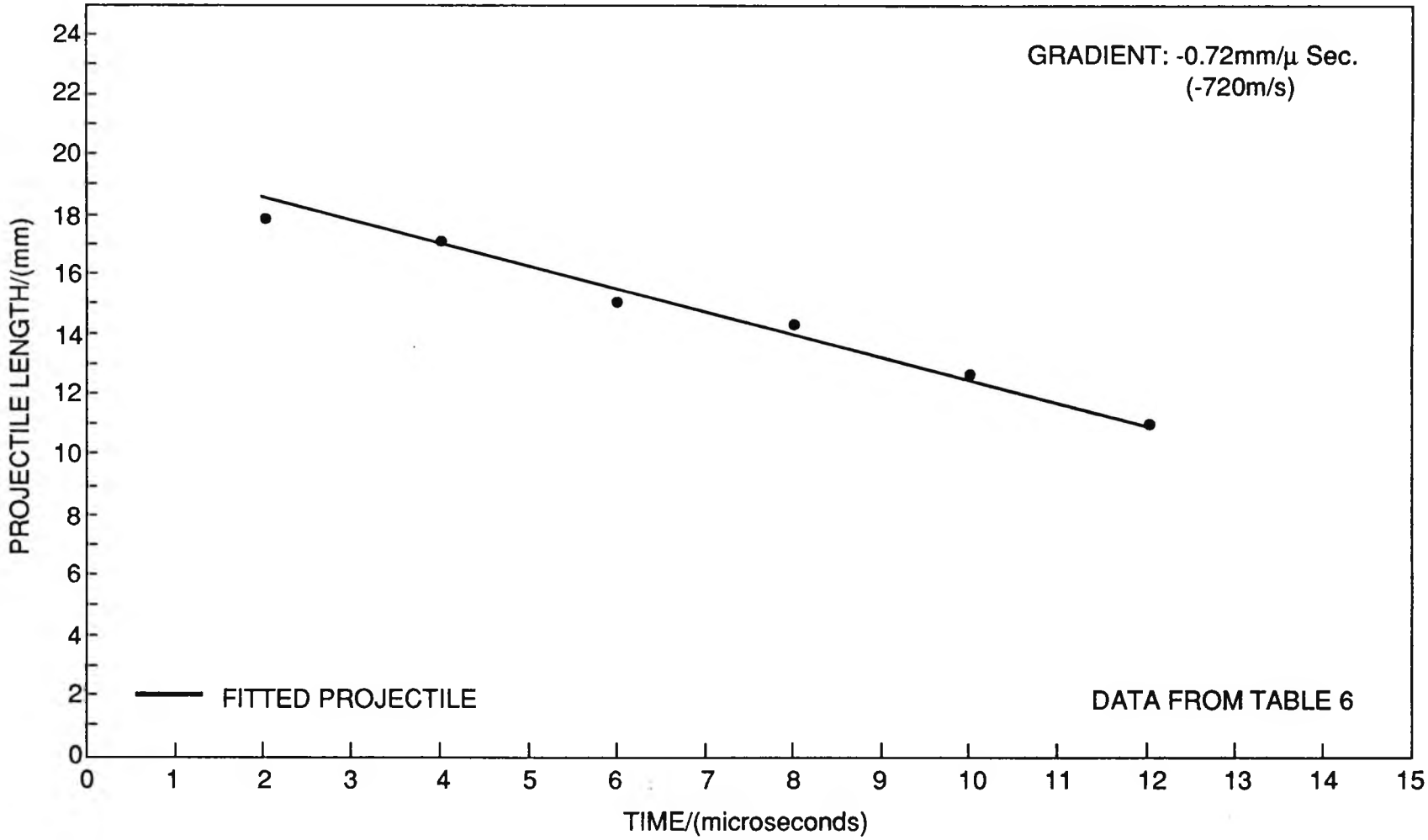

FIG. 36. EROSION OF THE BULLET AS IT PENETRATES THE ALUMINA FACING (WITH ARAMID BACKING).

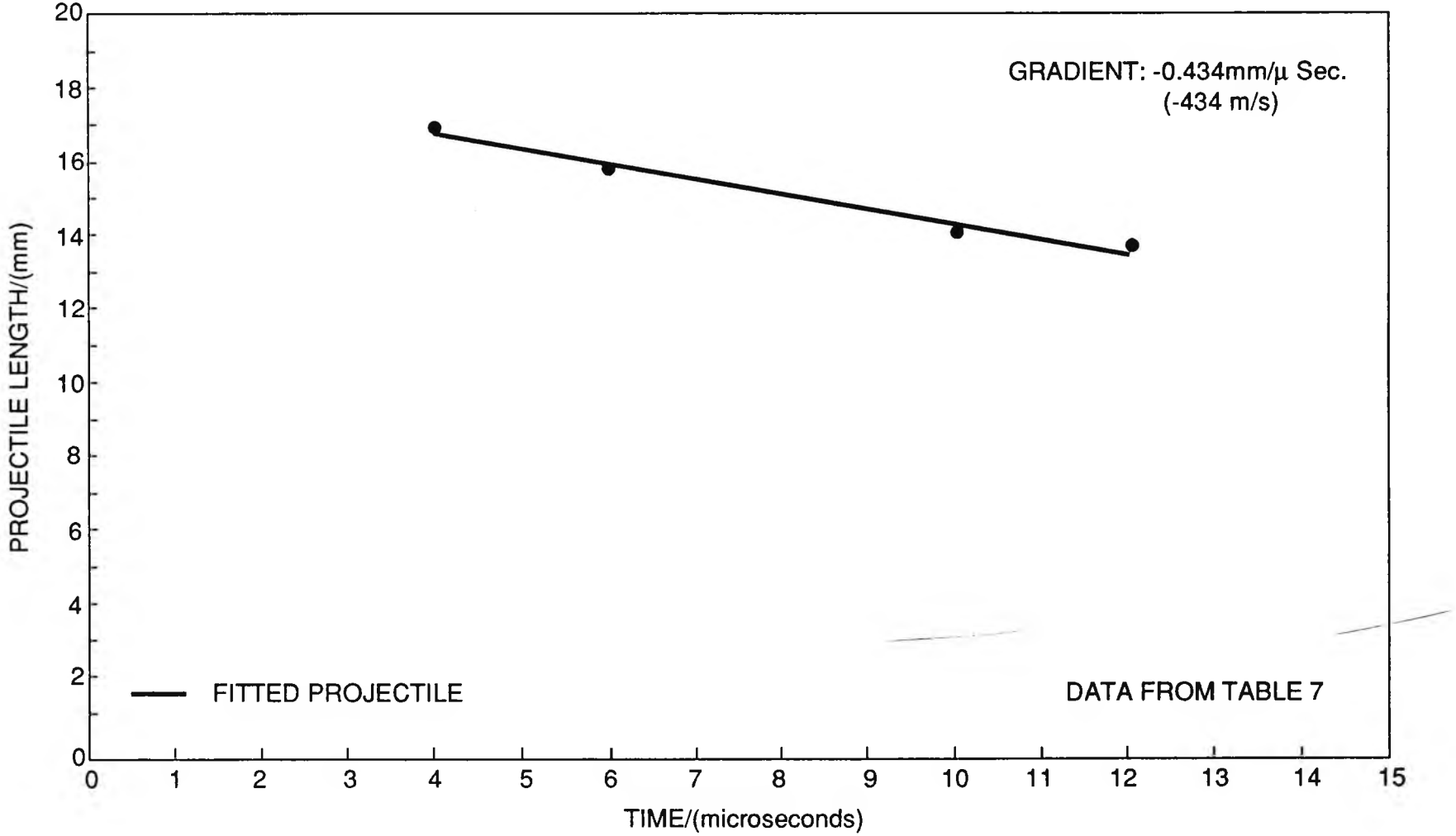

FIG. 37. EROSION OF THE BULLET AS IT PENETRATES THE GLASS FACING (WITH ARAMID BACKING).

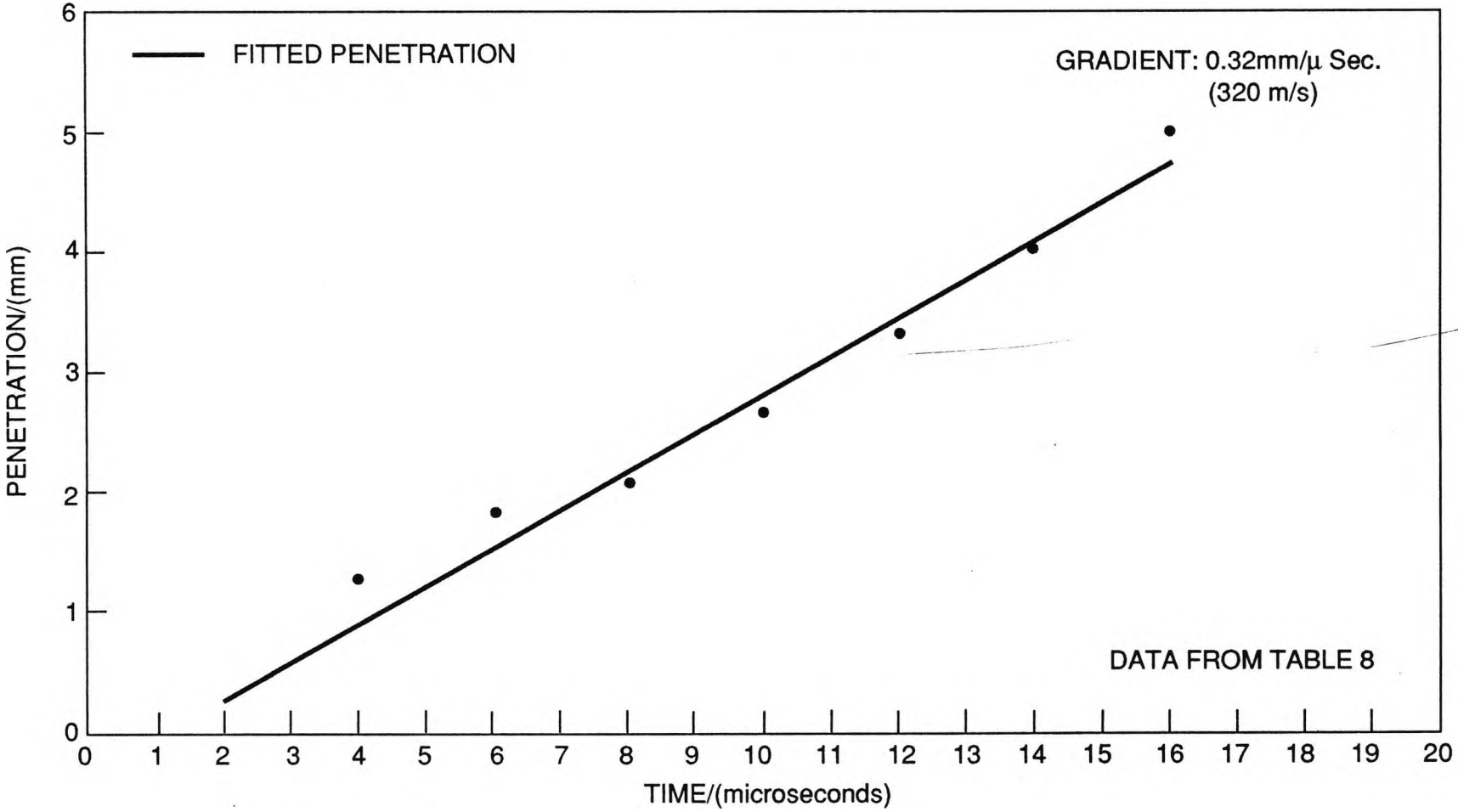

FIG. 38. PENETRATION OF THE BULLET INTO THE ALUMINA FACING (WITH GRP BACKING).

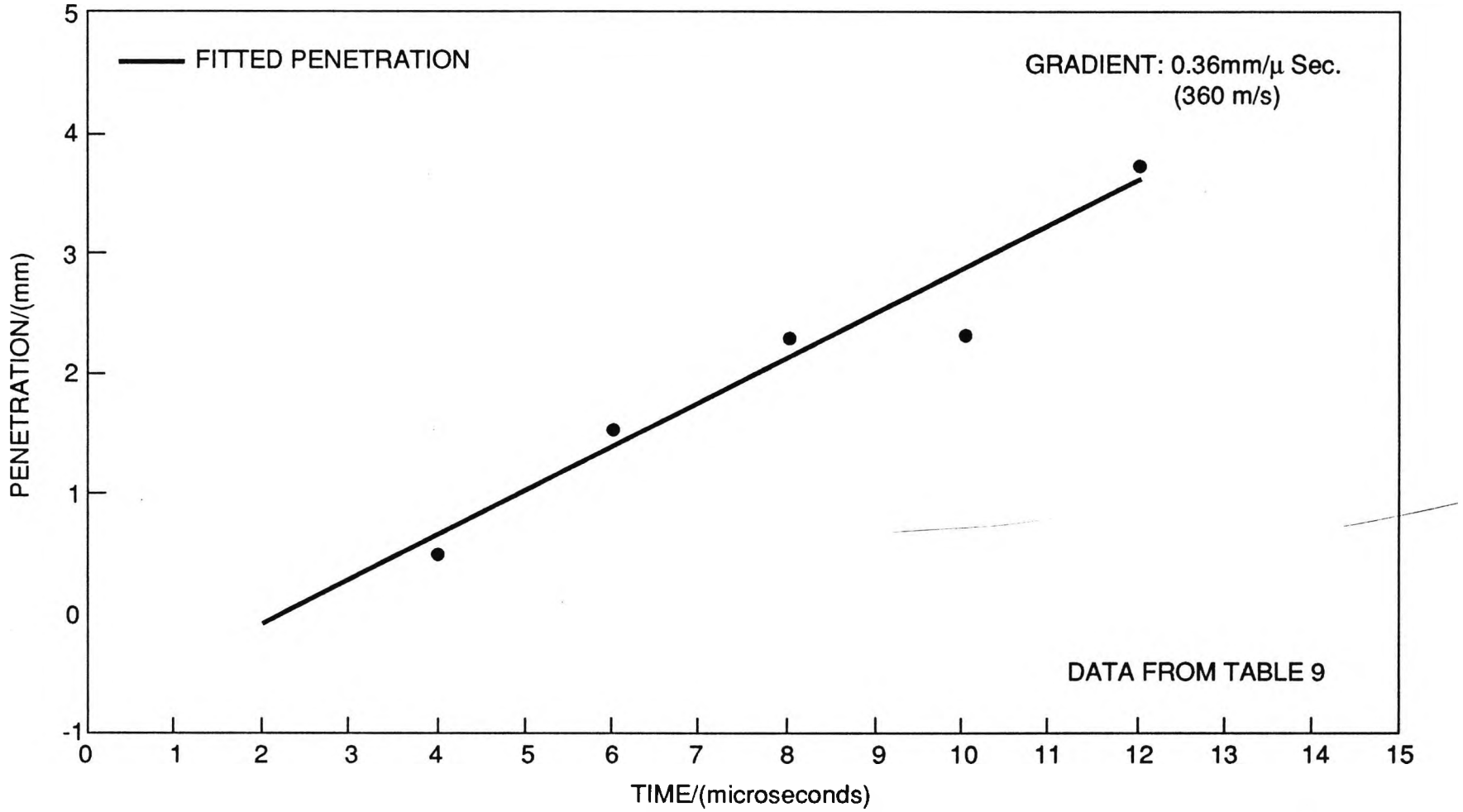

FIG. 39. PENETRATION OF THE BULLET INTO THE ALUMINA FACING (WITH ARAMID BACKING).

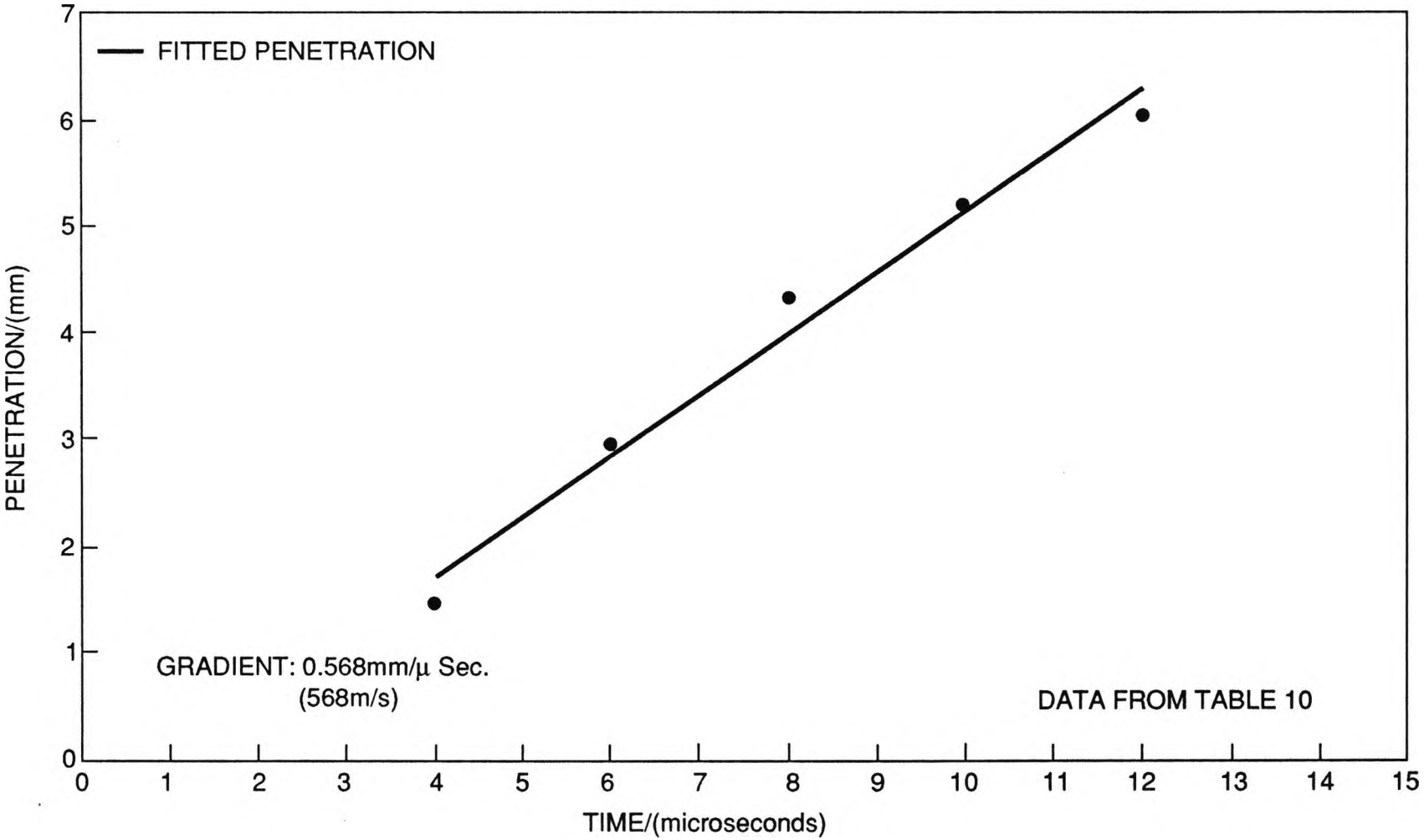

FIG. 40. PENETRATION OF THE BULLET INTO THE GLASS FACING (WITH ARAMID BACKING).

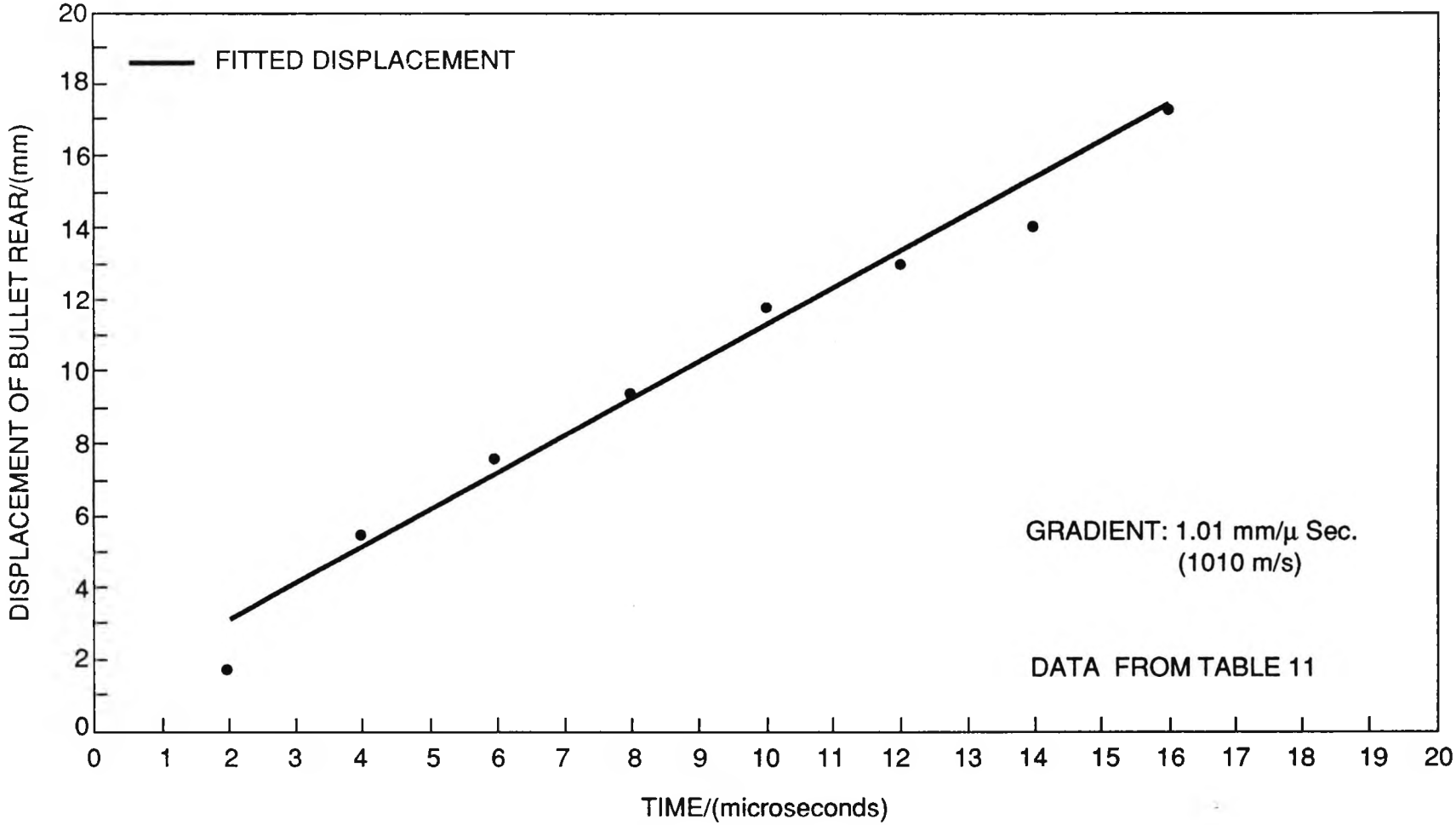

FIG. 41. DISPLACEMENT OF BULLET REAR FOR ALUMINA FACING (WITH GRP BACKING).

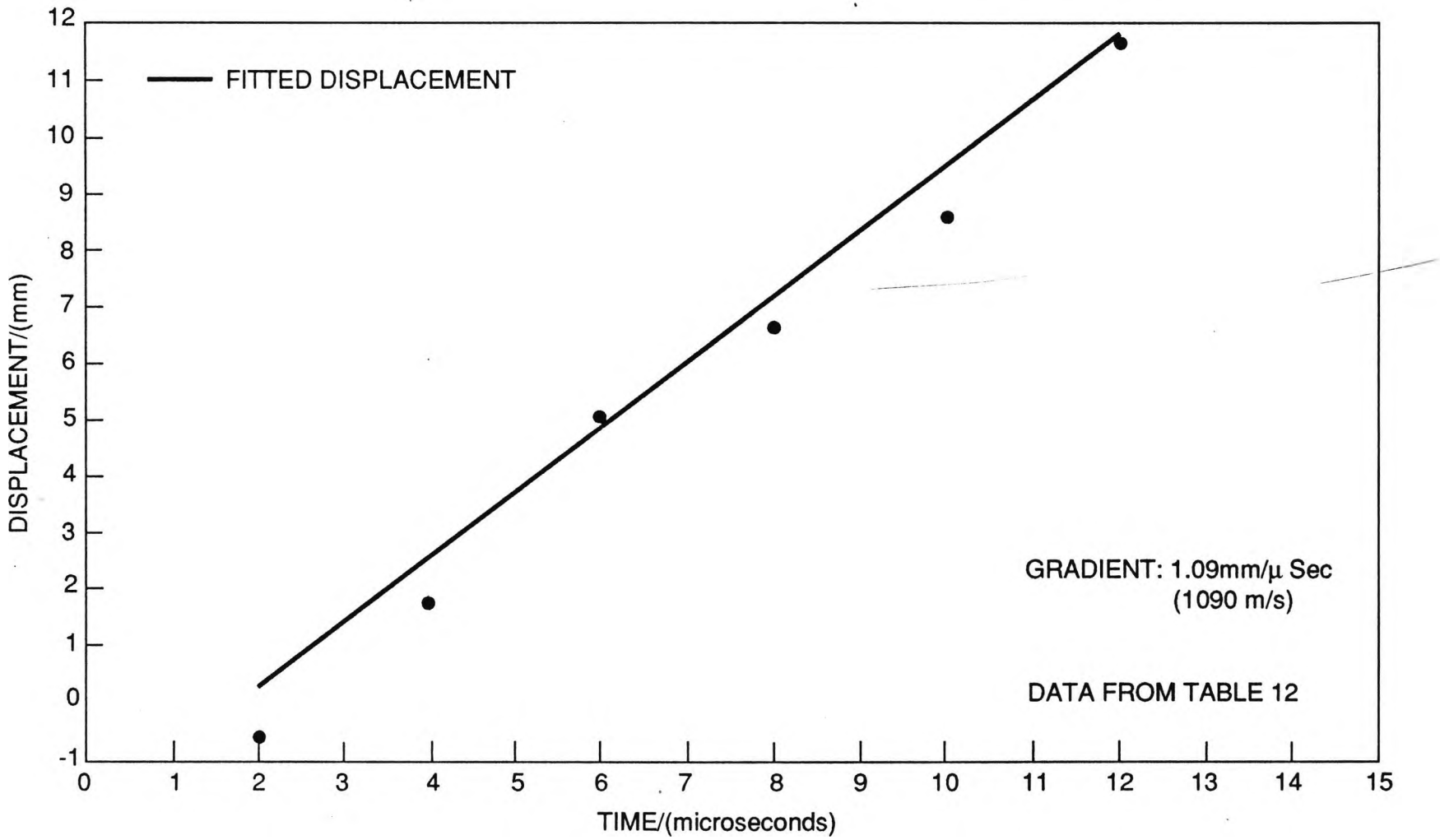

FIG. 42. DISPLACEMENT OF BULLET REAR FOR THE ALUMINA FACING (WITH ARAMID BACKING).

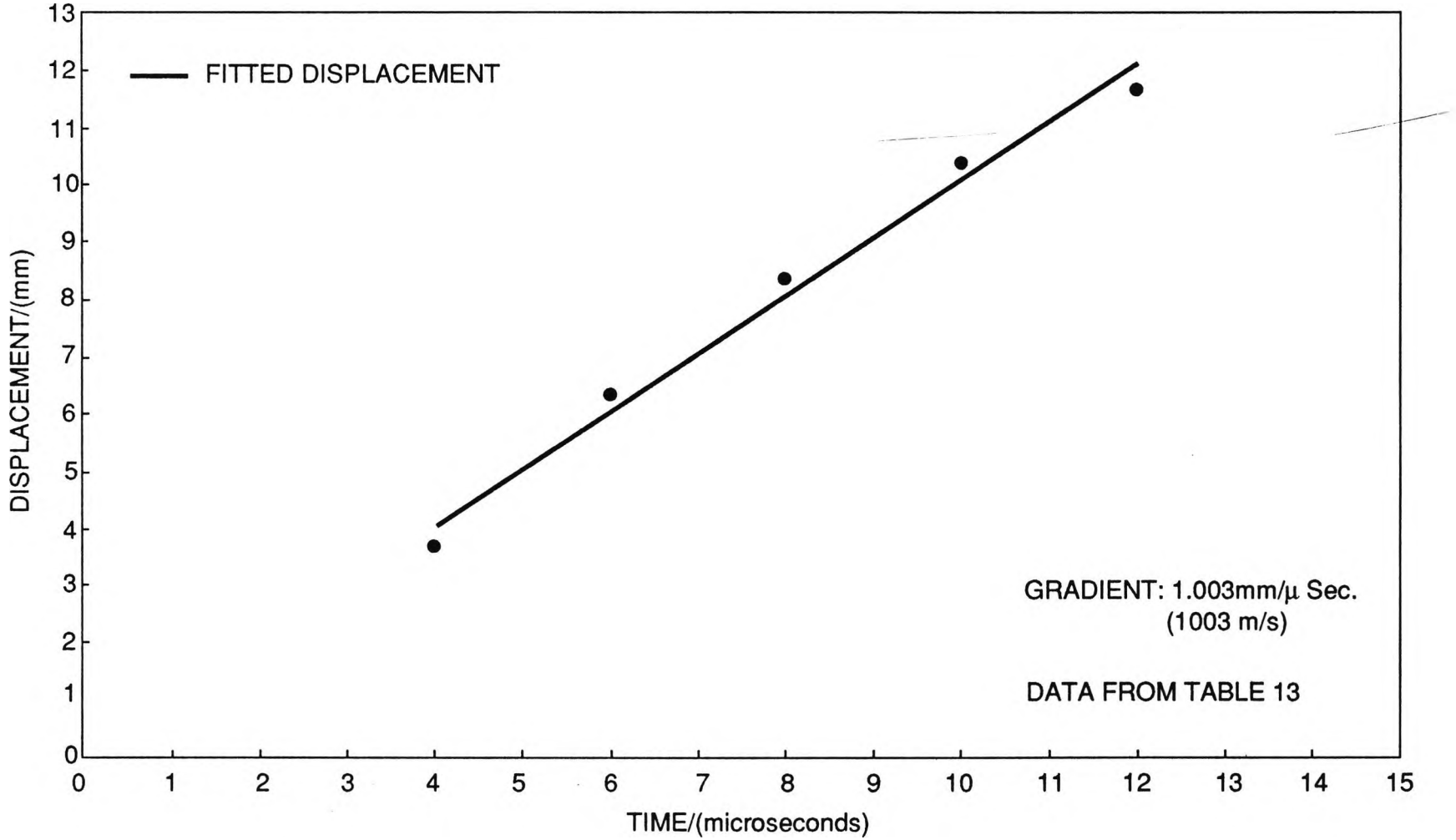

FIG. 43. DISPLACEMENT OF THE BULLET REAR FOR THE GLASS FACING (WITH ARAMID BACKING).

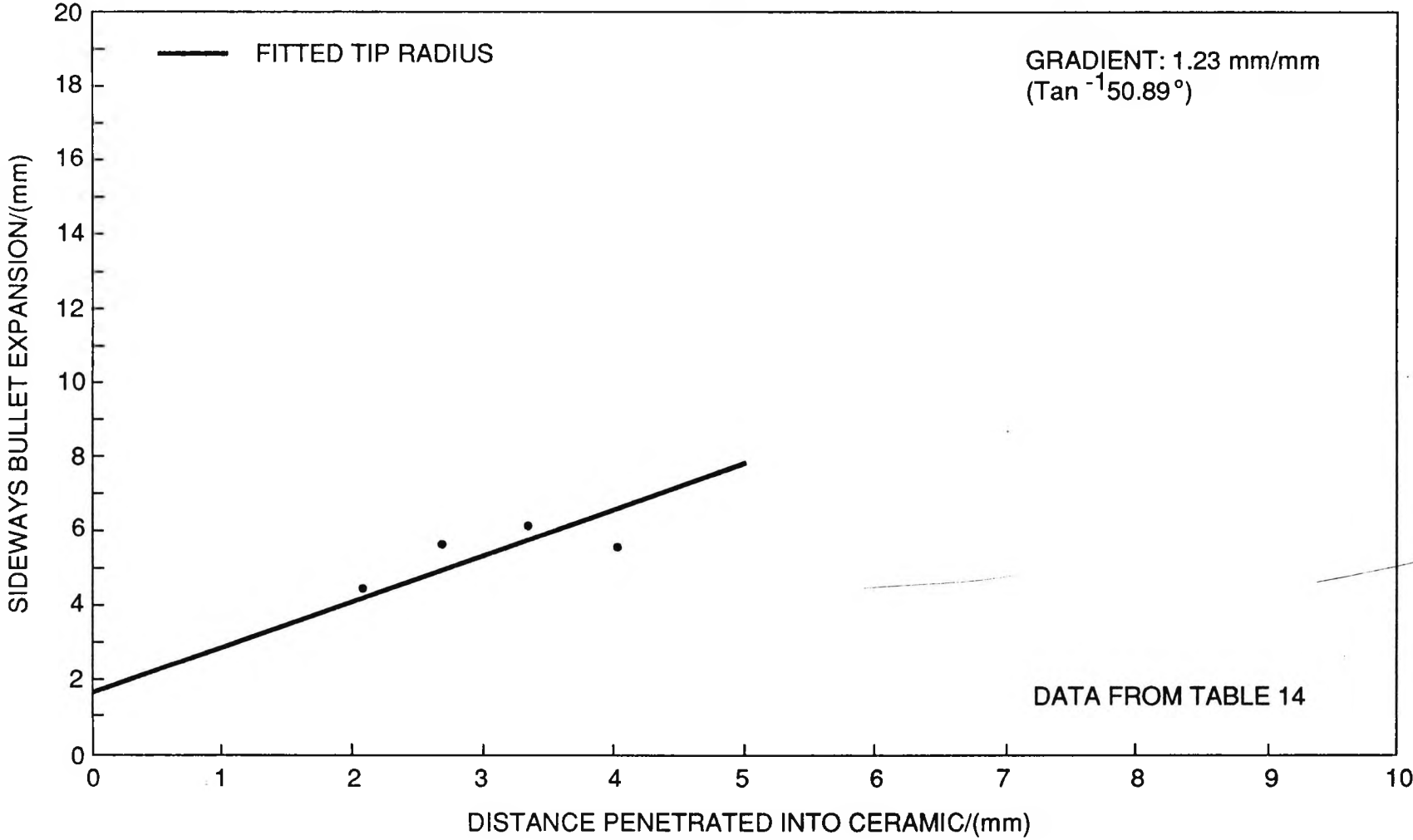

FIG. 44. SPREADING OF BULLET TIP AS IT PENETRATES THE ALUMINA FACING (WITH GRP BACKING).

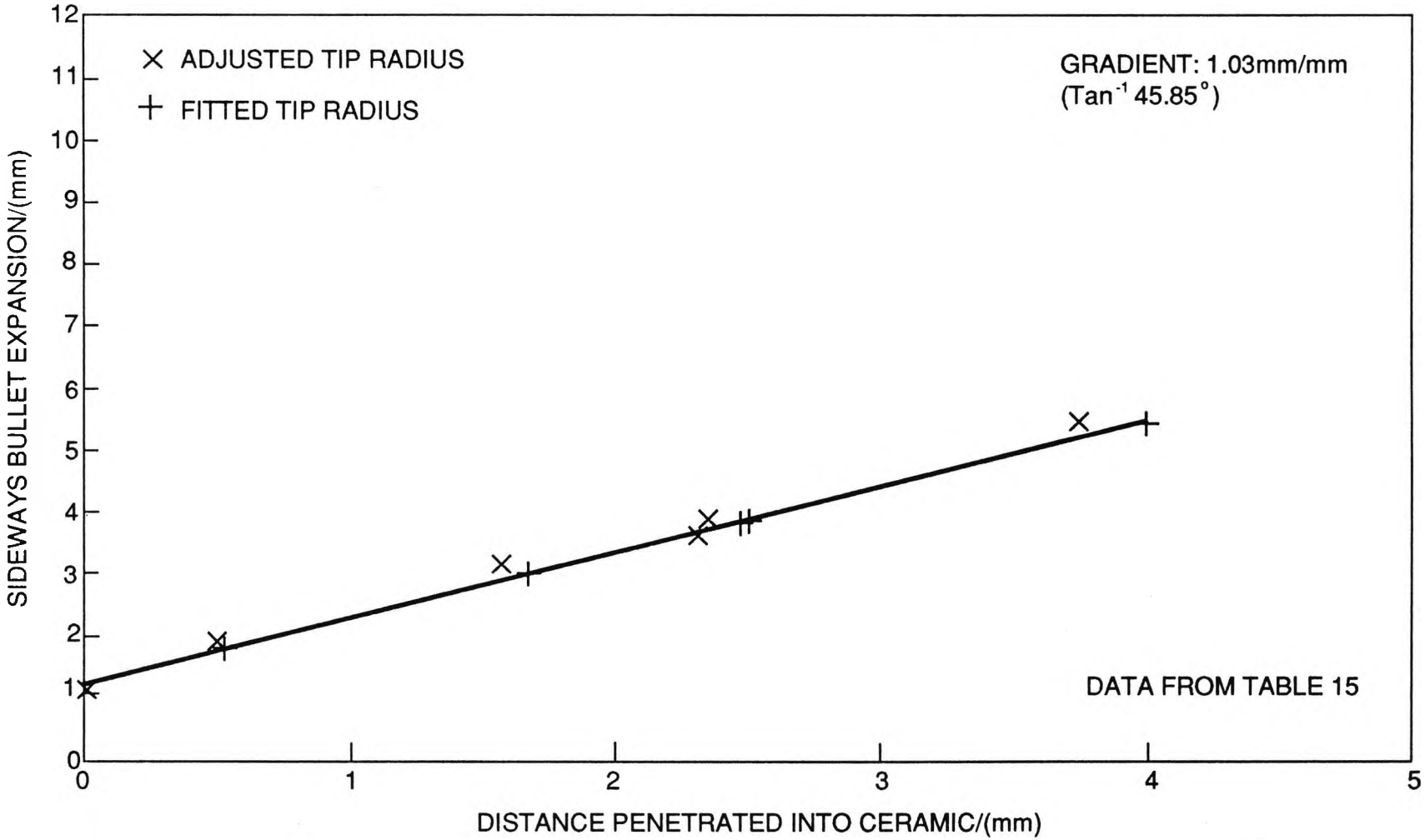

FIG. 45. SPREADING OF THE BULLET AS IT PENETRATES THE ALUMINA FACING (WITH ARAMID BACKING).

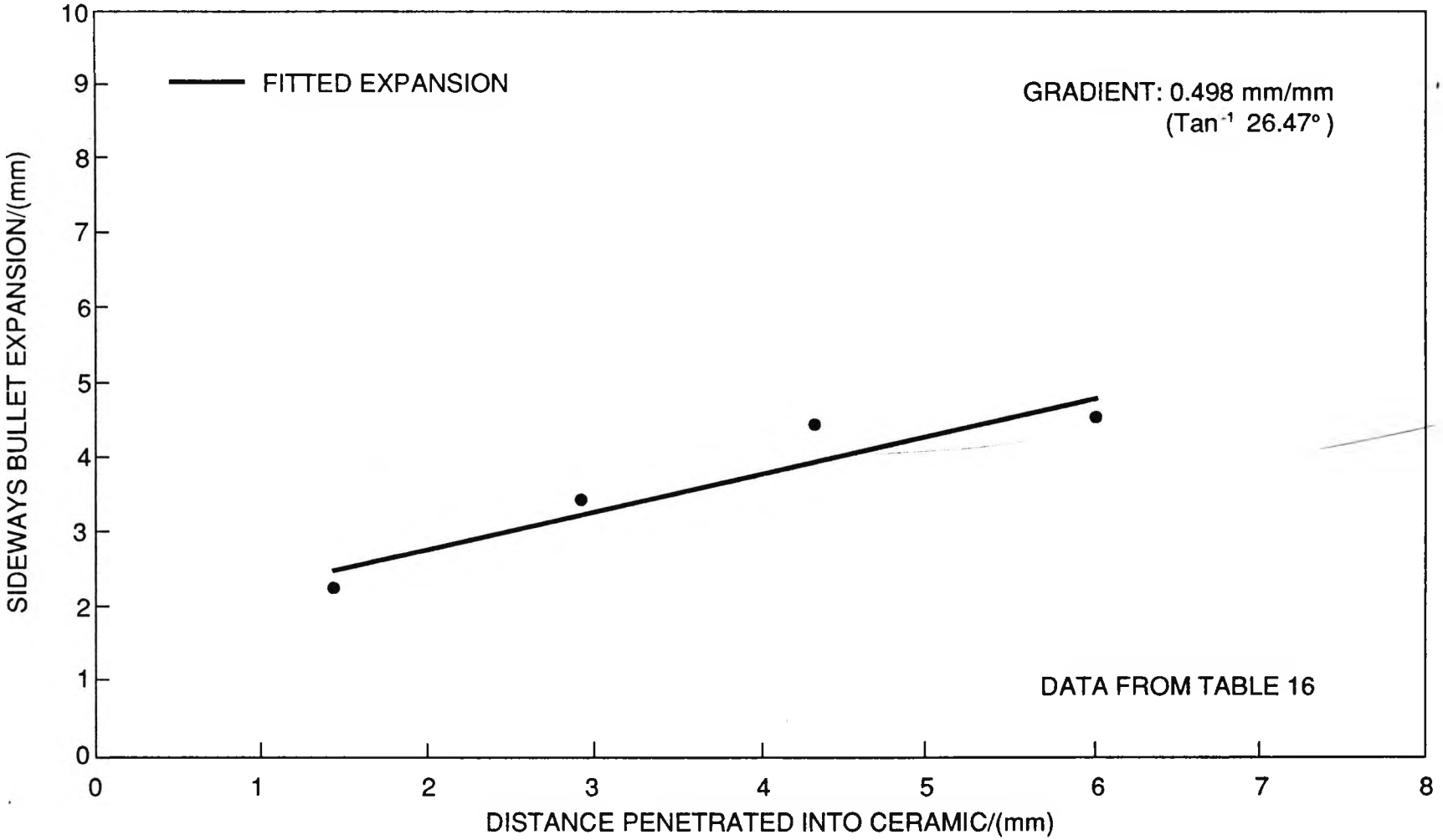

FIG. 46. SPREADING OF THE BULLET AS IT PENETRATES THE GLASS FACING (WITH ARAMID BACKING).

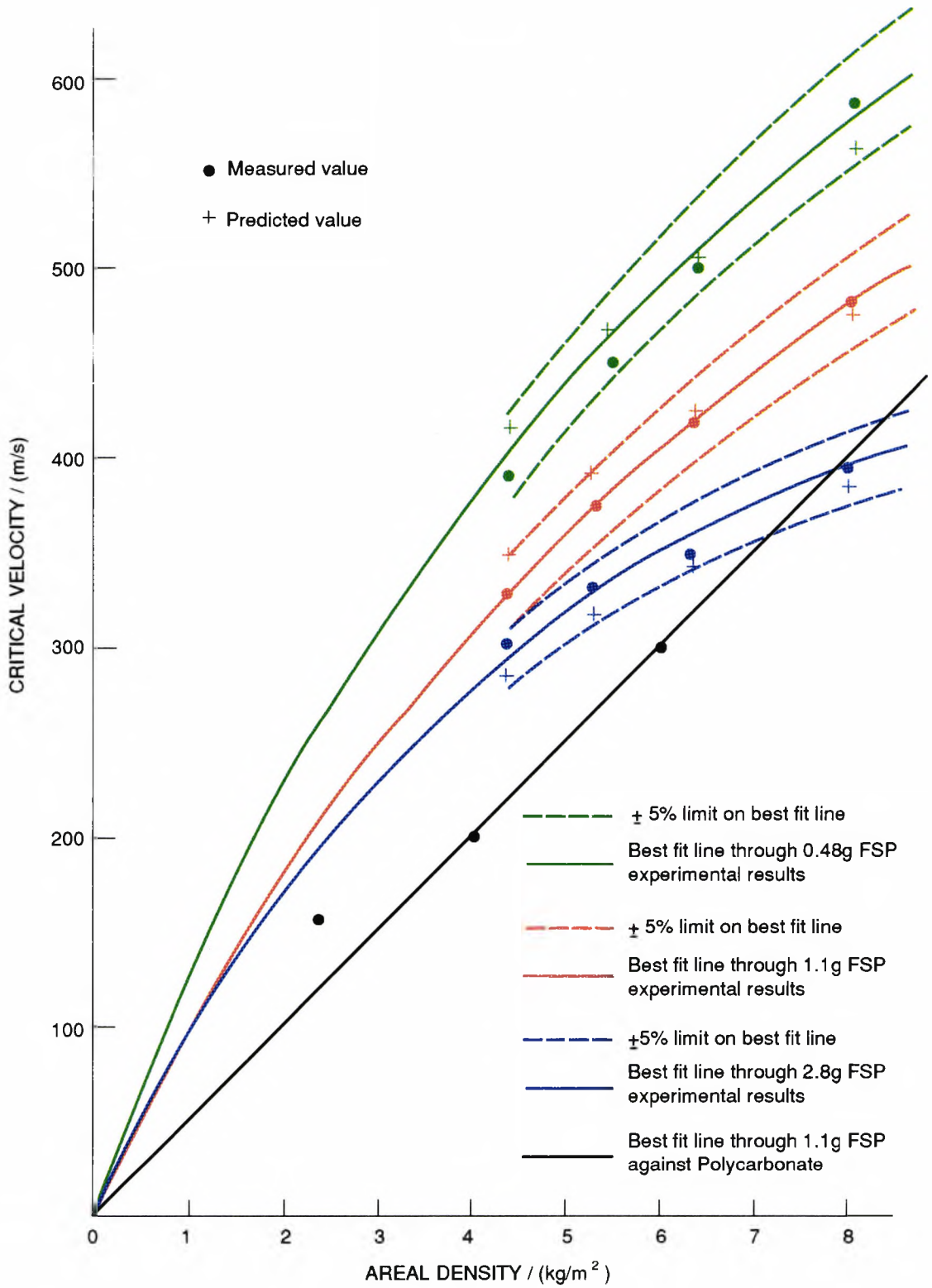

FIG. 47. GRAPH SHOWING PREDICTED AND MEASURED CRITICAL VELOCITIES OF ARAMID LAMINATES.

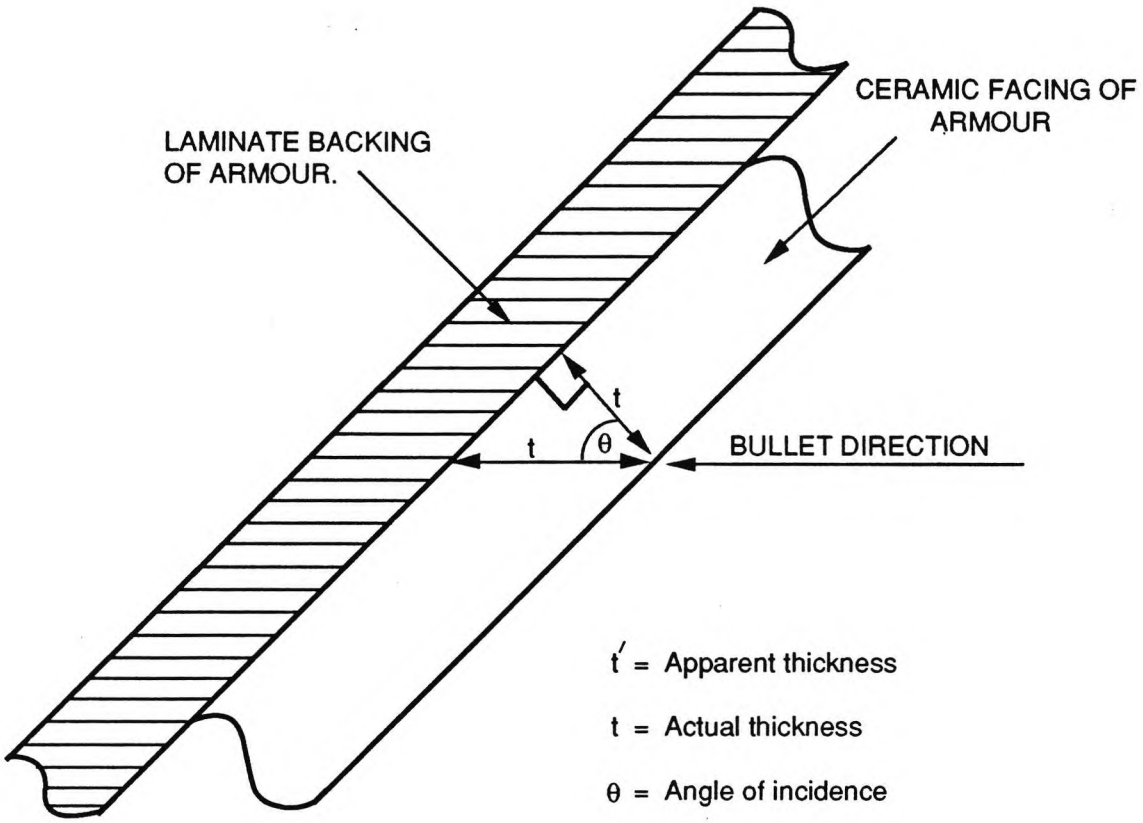

$$t' = \frac{t}{\text{Cos}\,\theta} = t\,\text{Sec}\,\theta$$

FIG. 48. RELATIONSHIP BETWEEN APPARENT THICKNESS AND ACTUAL THICKNESS OF THE CERAMIC.

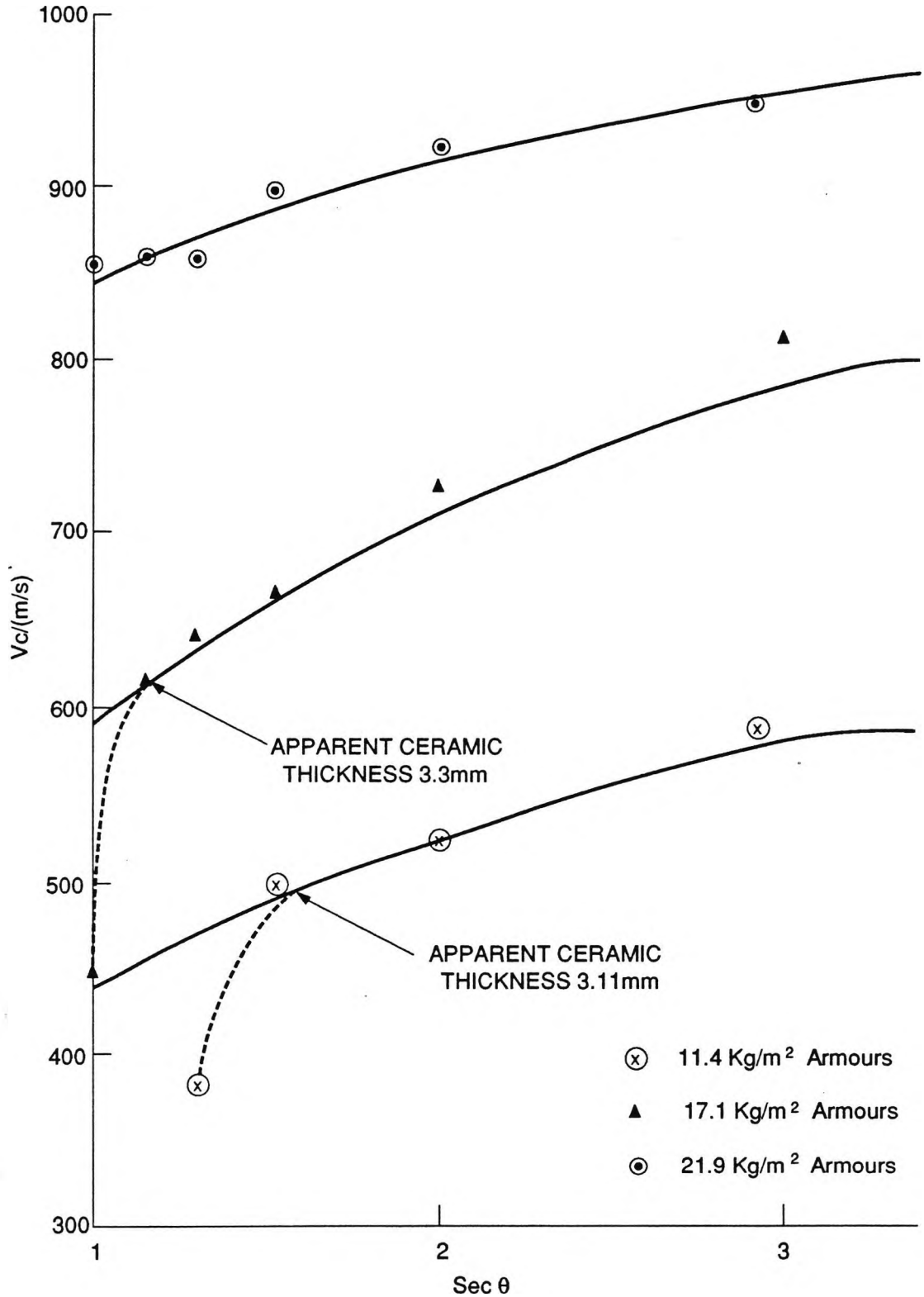

FIG. 49. GRAPH OF Vc v Sec. θ.

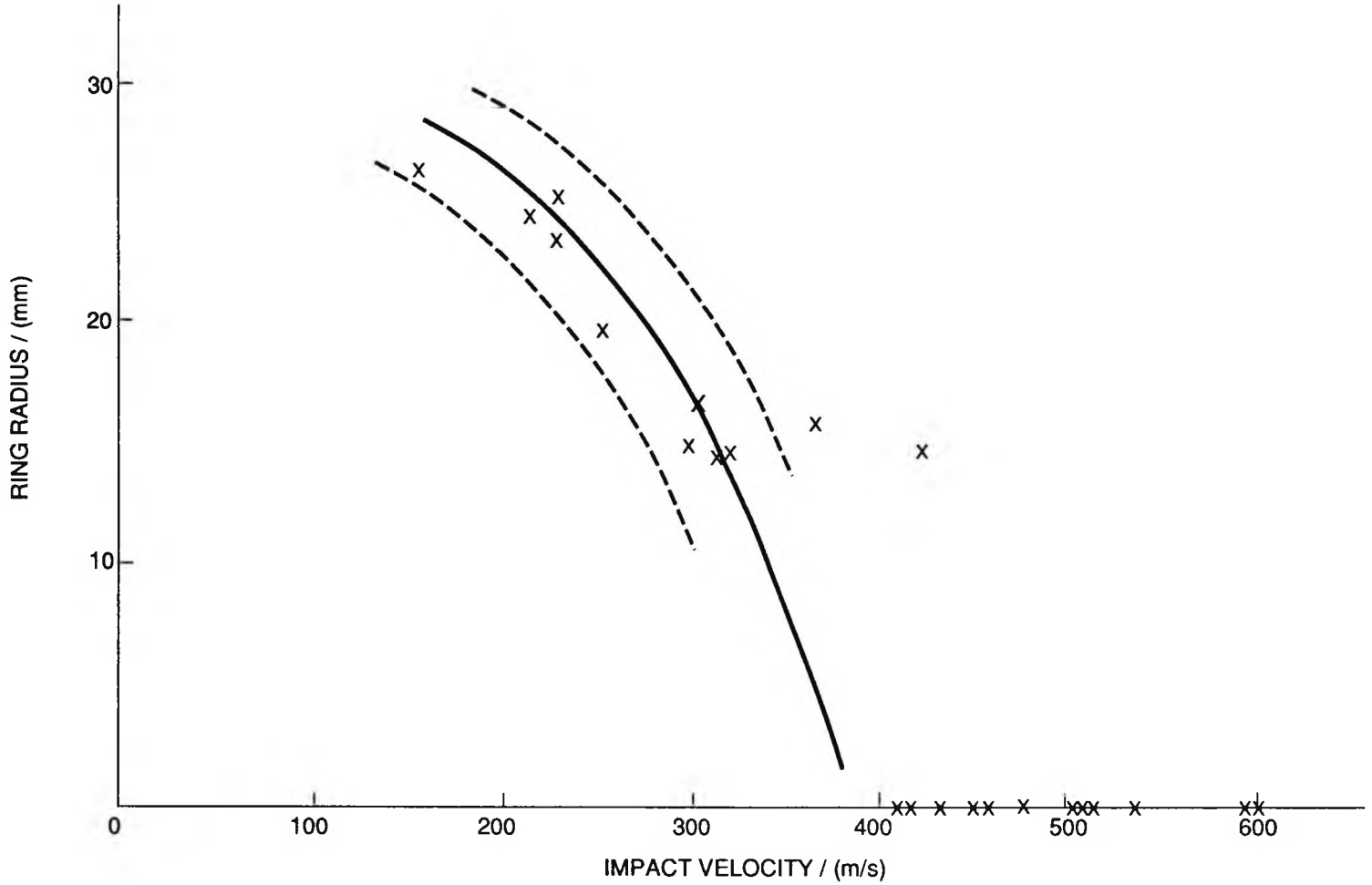

FIG. 50. GRAPH OF IMPACT VELOCITY OF FRAGMENT SIMULATING PROJECTILE

V

RADIUS OF FACTURE RING IN HARD COATING ON POLYCARBONATE.

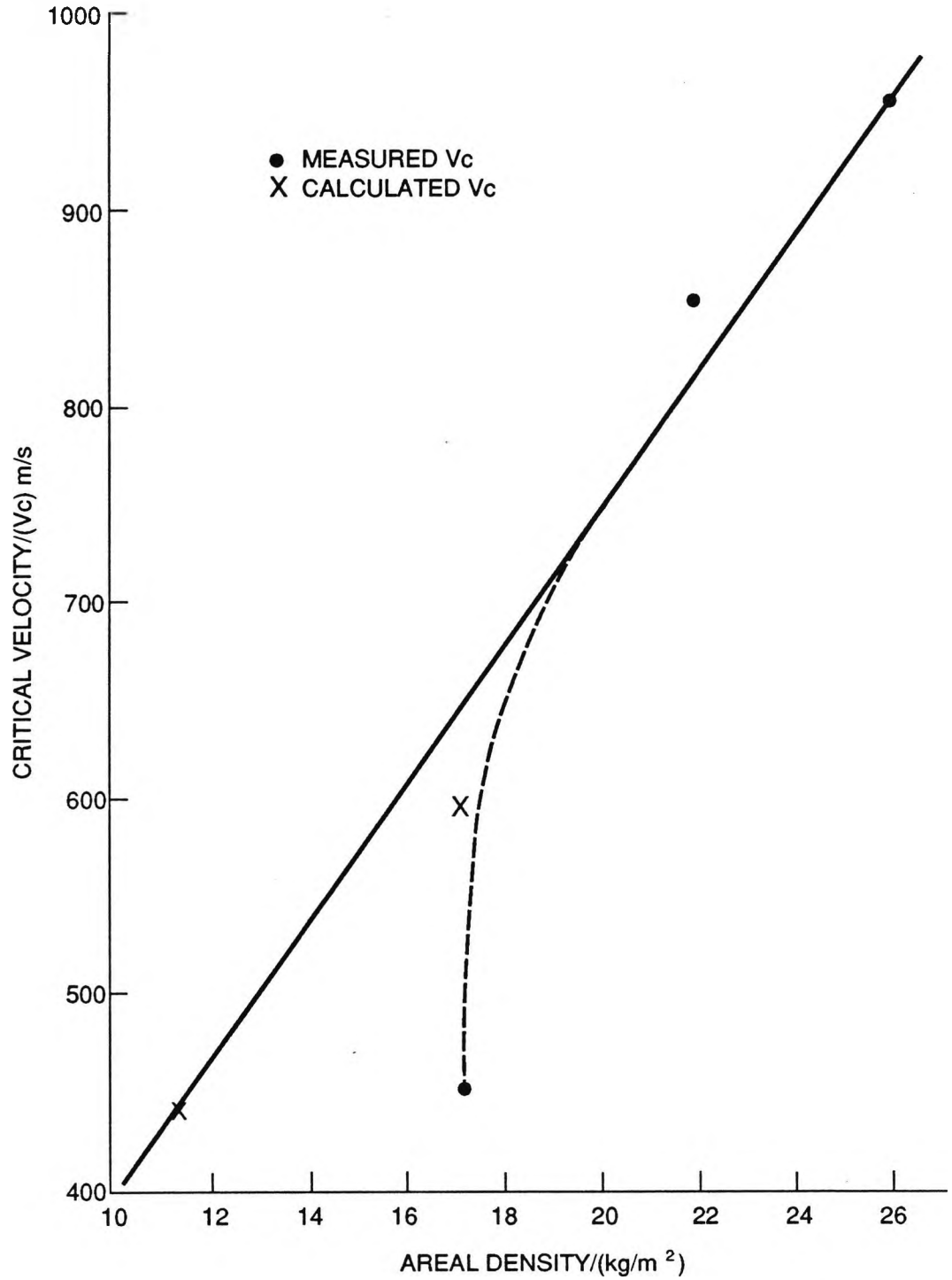

FIG. 51. CRITICAL VELOCITY v AREAL DENSITY FOR ALUMINA FACED ARAMID BACKED ARMOURS AGAINST 5.56mm L3A1 AMMUNITION.

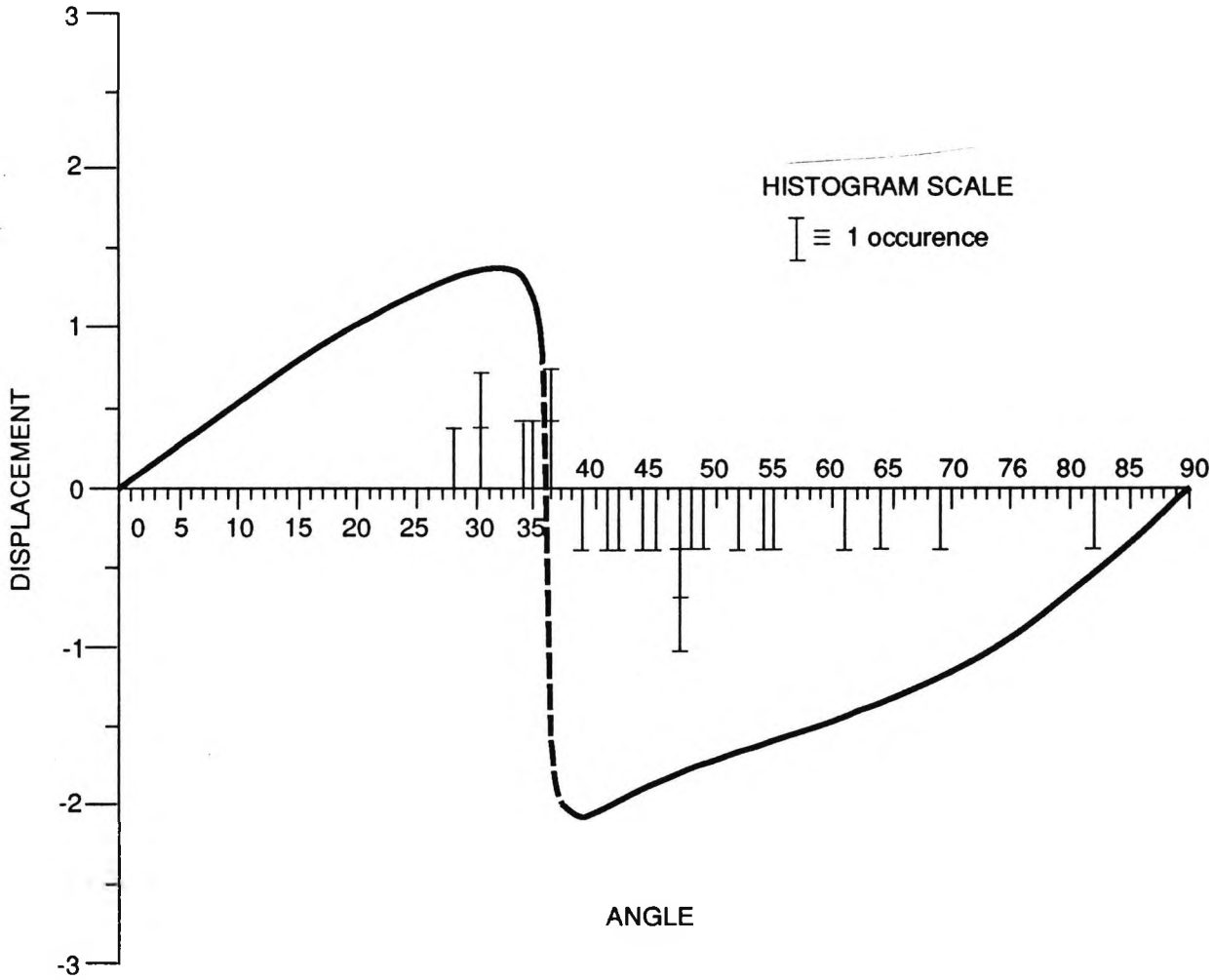

FIG. 52. DISPLACEMENT OF SHEAR WAVE v ANGLE.

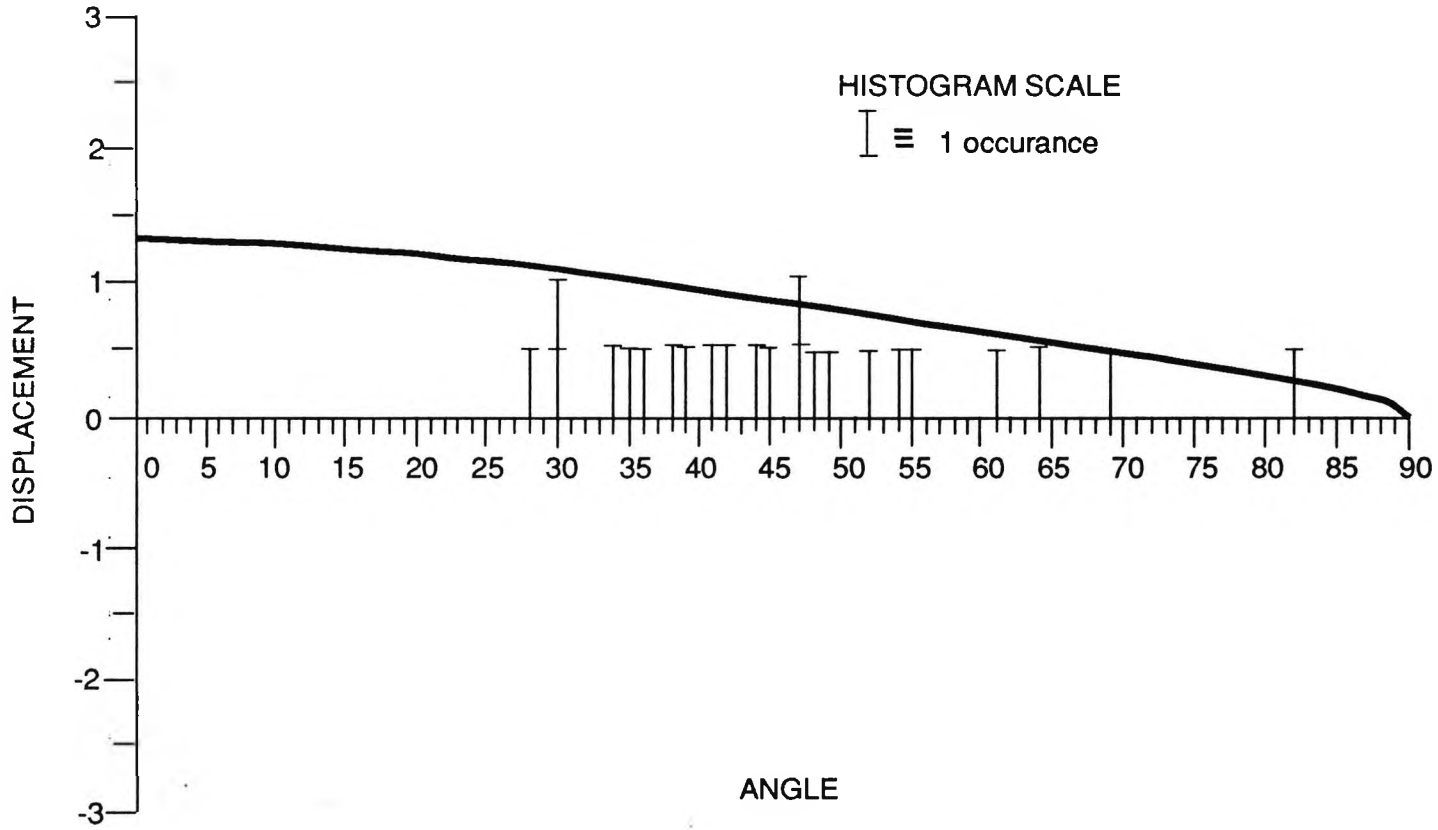

FIG. 53. DISPLACEMENT OF COMPRESSION WAVE v ANGLE.

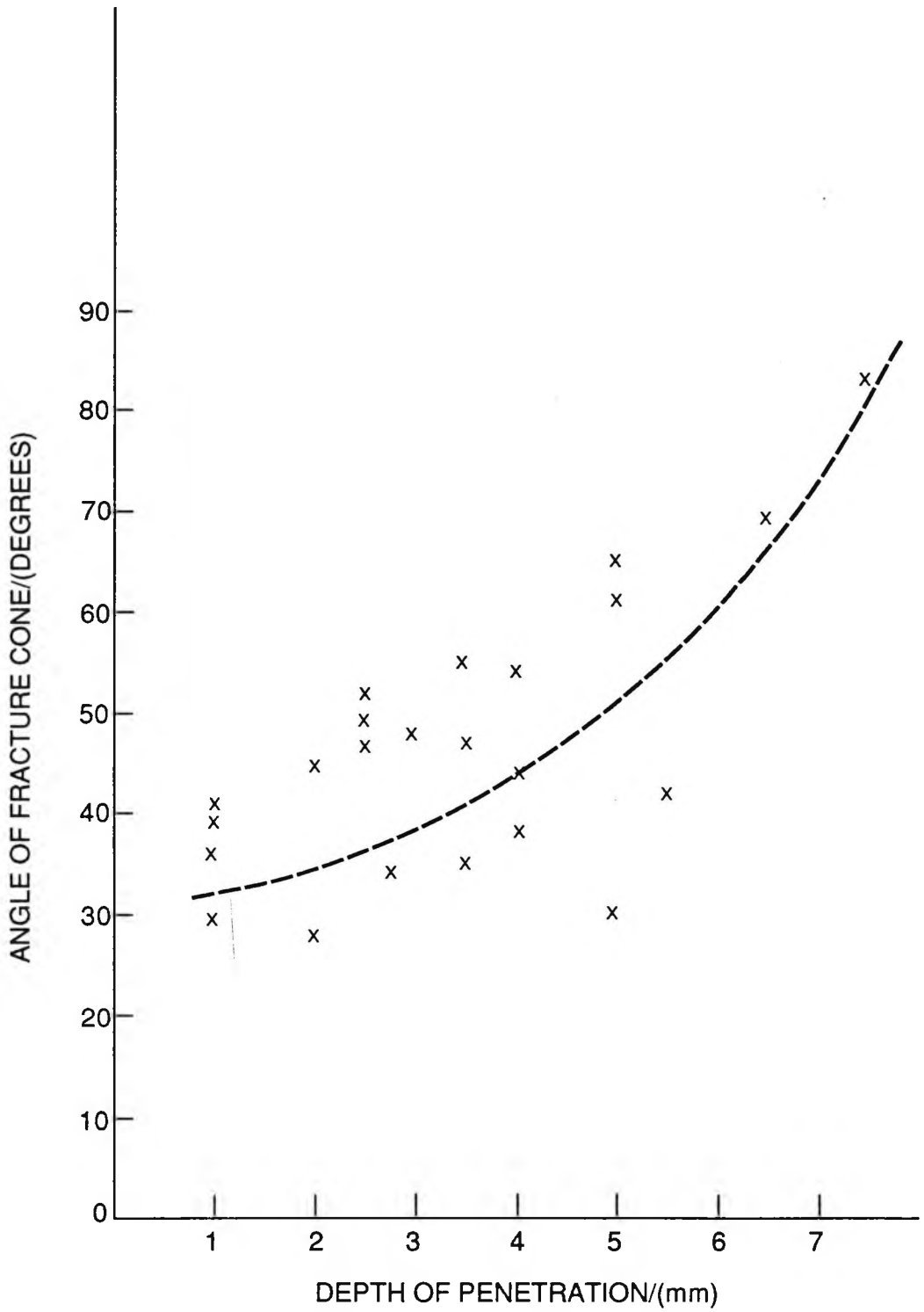

FIG. 54. FRACTURE CONE ANGLE v DEPTH OF PENETRATION.

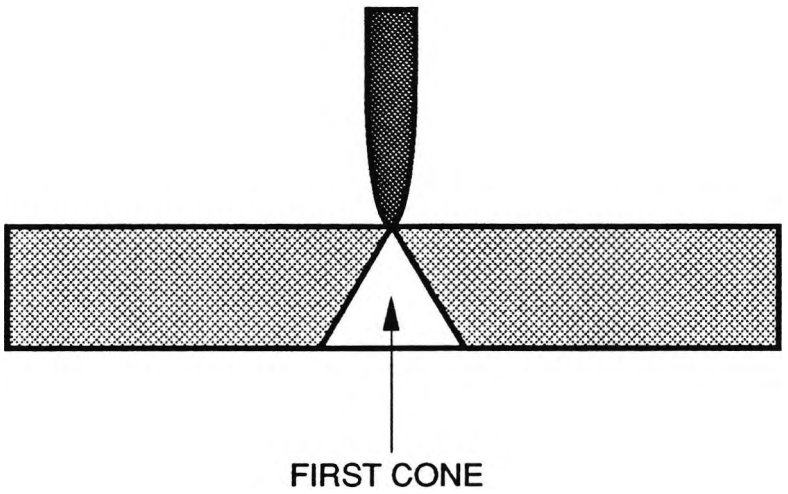

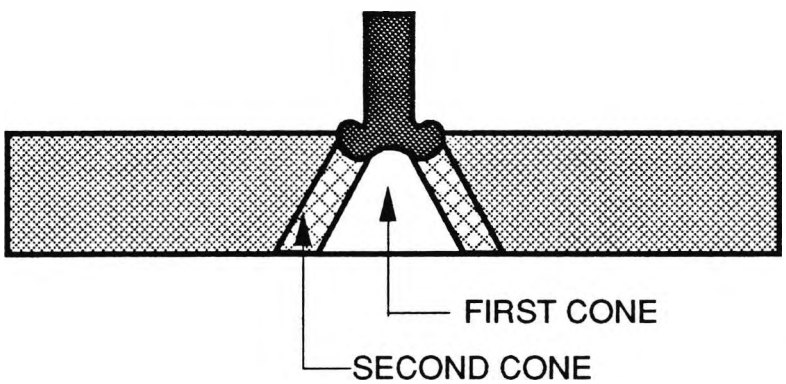

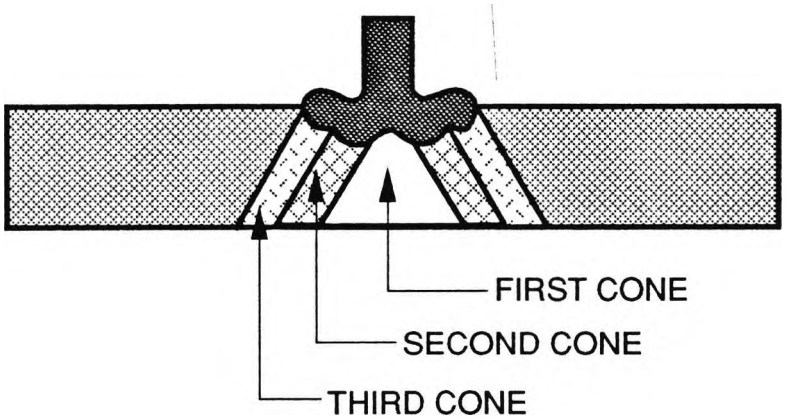

FIG. 55. DIAGRAM OF FRACTURE CONE AND BULLET PENETRATING.

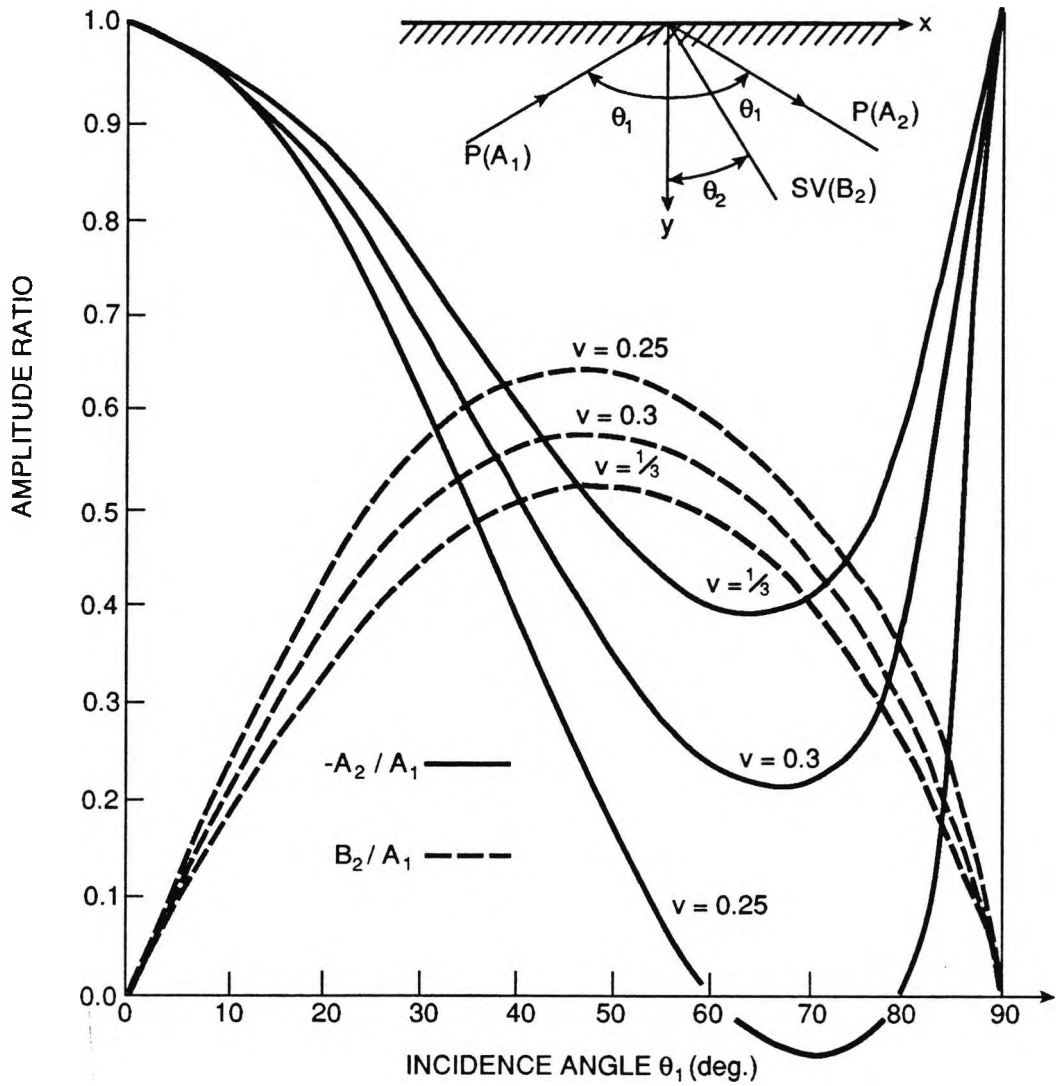

AMPLITUDE RATIOS A_2 / A_1, B_2 / A_1 FOR INCIDENT P WAVES, FOR VARIOUS POISSON'S RATIOS, WITH A RAY REPRESENTATION OF THE REFLECTION ALSO SHOWN. (AFTER KOLSKY).

FIG. 56. WAVES IN SEMI - INFINITE MEDIA.

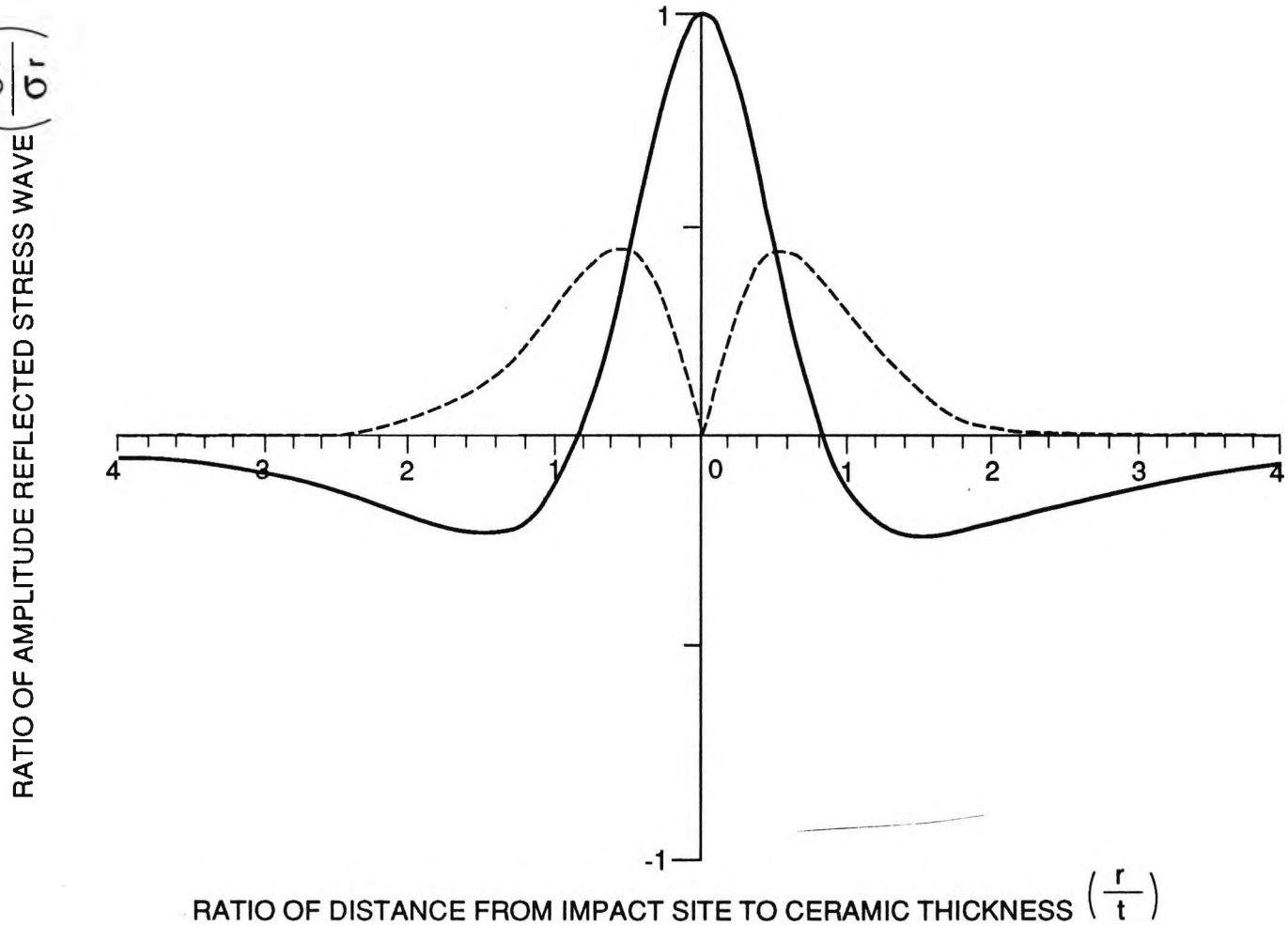

FIG. 57. AMPLITUDE OF REFLECTED STRESS WAVE FROM THE REAR FACE OF THE CERAMIC.

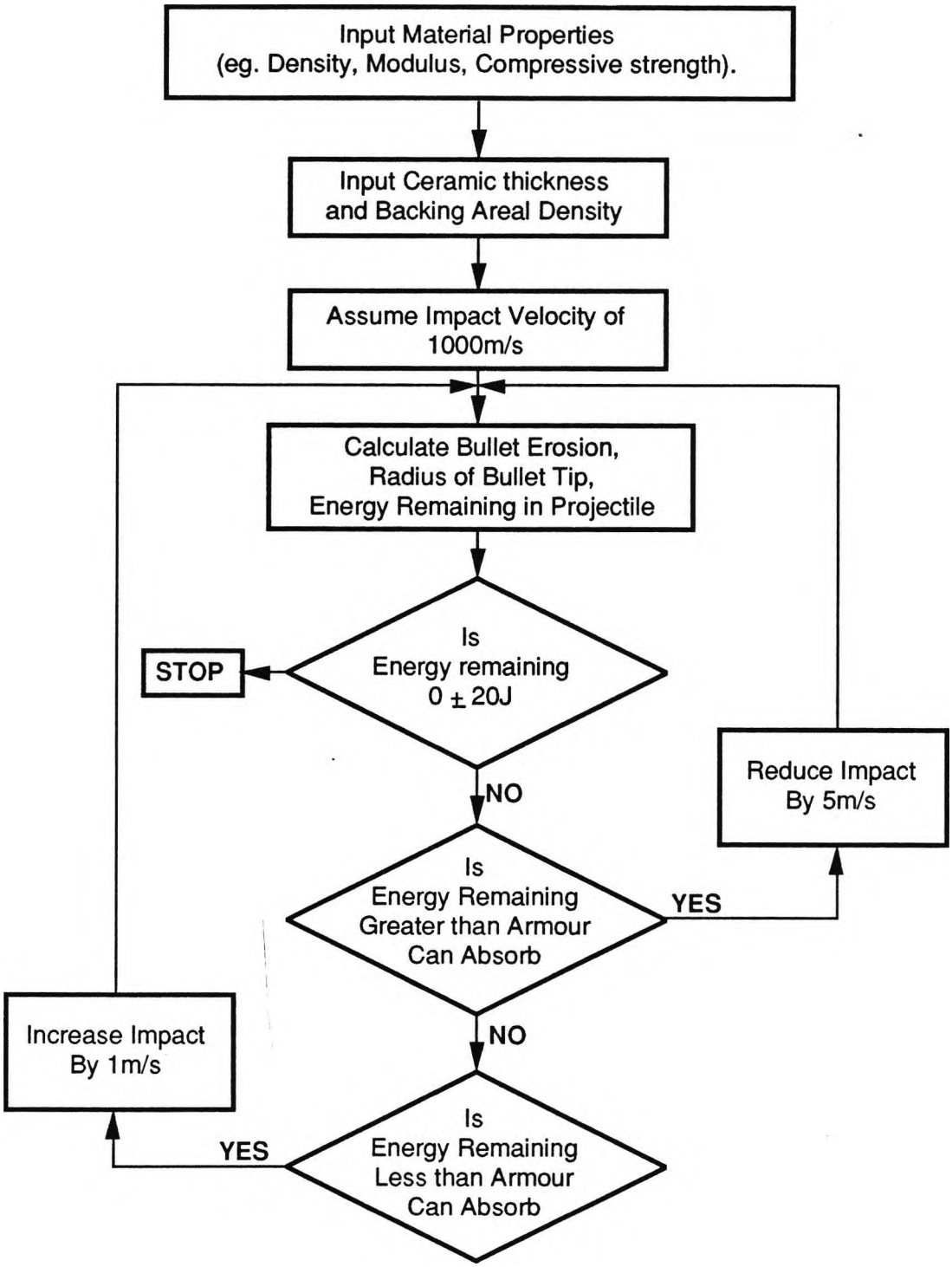

FIG. 58.
FLOW DIAGRAM FOR PERFORMANCE MODEL.

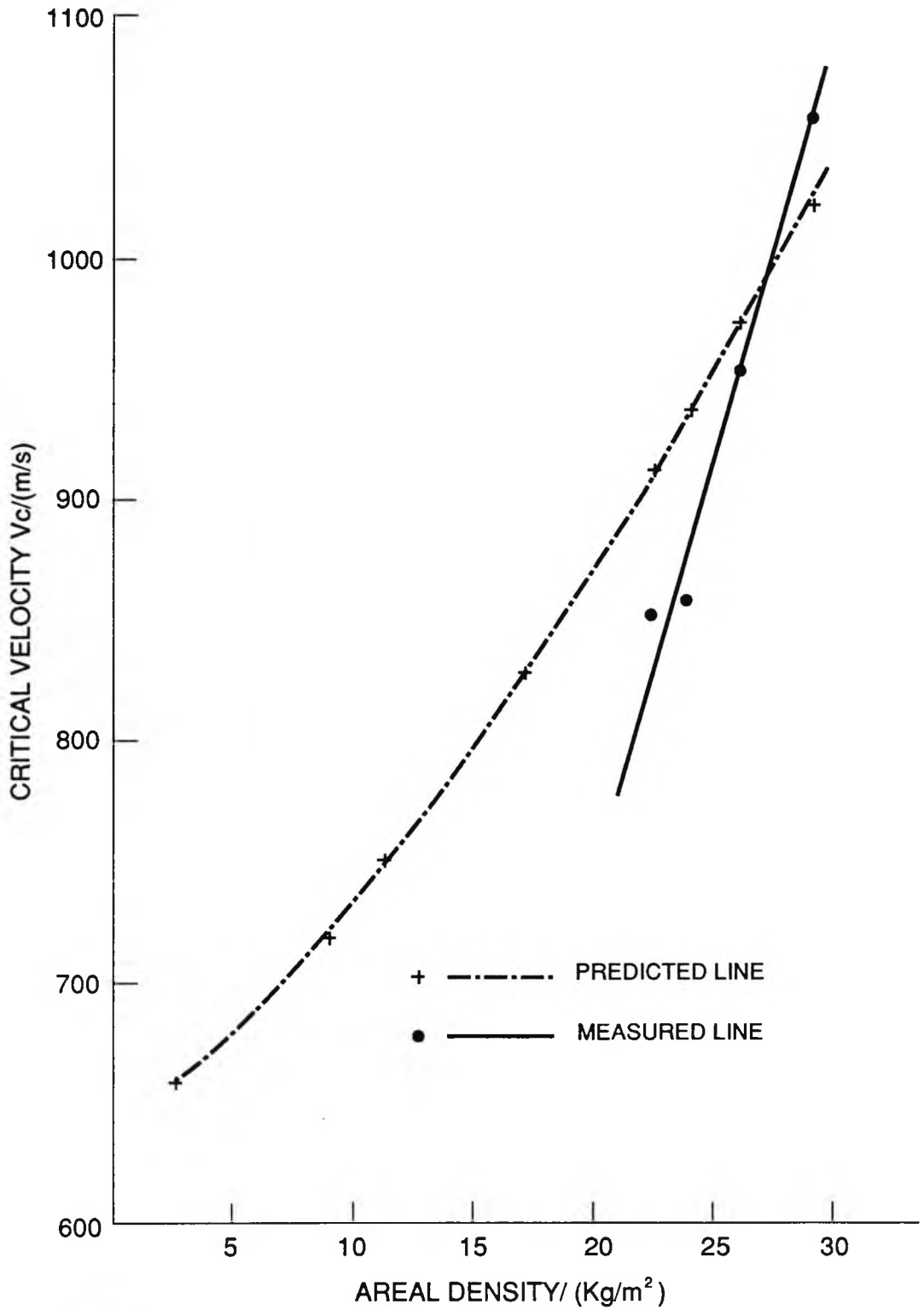

FIG. 59. A GRAPH OF PREDICTED AND MEASURED Vc VALUES FOR ALUMINA FACED ARAMID BACKED ARMOURS